DEFORMABLE HAPTIC MODELS FOR SURGICAL SIMULATION

by

Xiuzhong Wang

Presented to the Faculty of the Graduate School of
The University of Texas at Arlington in Partial Fulfillment
of the Requirements
for the Degree of

DOCTOR OF PHILOSOPHY

THE UNIVERSITY OF TEXAS AT ARLINGTON
August 2005

To my family $\cdots$

ACKNOWLEDGEMENTS

I would like to acknowledge my supervising advisor, Professor Venkat Devarajan, who constantly motivated and encouraged me during the course of my doctoral studies. I greatly appreciate the guidance and the financial support that he provided. In particular, he challenged me to solve the open problem of mass-spring-damper model parameter optimization which has turned out to be the core of this dissertation. I would also like to thank my doctoral committee memembers Dr. Robert C. Eberhardt, Dr. Kambiz Alavi, Dr. Jung-Chih Chiao, Dr. Qilian Liang and Dr. Wei-Jen Lee for their interest in my research and for taking time to serve in my dissertation committee. Additional thanks are especially to Dr. Elberhart for being my biomedical engineering guide.

I would like to extend my appreciation to the Texas Higher Education Coordinating Board and UTA Electrical Engineering Department for providing financial support, as well as the department staff for their administrative support. Many thanks to the group of wonderful and talented people who worked together with me in the Virtual Environment Lab. I have learned a great deal from them all. I wish them the very best of success in their lives and careers.

I am eternally indebted to my family and friends who have encouraged and inspired me and sponsored my graduate studies. I am extremely fortunate to be so blessed. I am also extremely grateful to my wife for her sacrifice, encouragement and patience.

July 18, 2005

ABSTRACT

DEFORMABLE HAPTIC MODELS FOR SURGICAL SIMULATION

Publication No. _____

Xiuzhong Wang, Ph.D.

The University of Texas at Arlington, 2005

Supervising Professor: Venkat Devarajan

Surgical simulation is in great need for surgical training, analysis, planning and rehearsal. One of the core problems in this application is the real time deformation of the models for human organs. The deformable models must provide both realistic visual effects (graphics) and high fidelity force feedback (haptics) in real time, without distractive visual artifacts or misleading tactile clues. In view of the requirement of physical accuracy, physically based deformable models are desirable for surgical simulation.

Physically based deformable modeling has been a serious research topic for about twenty years in the computer graphics community. For computer animation, a great deal of work has been done so that the model can barely provide realistic (physically plausible) visual effects in real time. Surgical simulation has a much higher requirement for the deformable model. First, to meet the haptics update rate of 1000 Hz rather than the graphics update rate of 30 Hz, the cycle time for regenerating the deformable model decreases by a factor of 33. Second, the physical accuracy needed for high fidelity force

feedback is much more challenging to achieve than realistic visual effects, for it results in much heavier computation.

Although there have been a lot of claims of successful application of physically based deformable models for computer animation, those models are far from mature for the applications supporting haptics, such as surgical simulation and emerging computer games supporting force feedback. The existing models are neither fast enough for real-time applications, nor can they provide both realistic deformations for graphics display and force feedback for haptics rendering. In view of this situation, it is essential to improve current deformable models or present better ones in terms of speed and physical accuracy when we aim to build a high fidelity surgical simulator for effective surgical training.

The scope of this dissertation is threefold. First, a new deformable model is proposed based on the structure and constitutive elements of human organs, which has potential to be more physically accurate though it can hardly meet the real time requirement for the current computer resources. Second, since the mass-spring-damper (MSD) model is currently the only deformable model able to meet the real time requirement, the physical accuracy of the 1D, 2D and 3D MSD models for both structured meshes and unstructured meshes is investigated based on continuum mechanics and the parameter optimization schemes are proposed and validated. Finally, the inguinal hernia surgery simulator is introduced and further research to apply the parameter optimization scheme is suggested.

TABLE OF CONTENTS

LIST OF FIGURES

LIST OF TABLES

CHAPTER 1

INTRODUCTION

1.1 Background

1.1.1 Minimally Invasive Surgery

Minimally invasive surgery [10], which includes endoscopic and laparoscopic surgery modes, is becoming increasingly popular. Unlike open surgery, it permits access to the internal organs without use of the customary large incision. Endoscopy of the rectal speculum was first described by Hippocrates (460–435 BC) [11]. Thus, the interest for physicians to look into the "internal organs" has existed since the early days of medicine.

The credit for modern endoscopy belongs to Philipp Bozzini (1773–1809) [10]. He developed a light conductor which he called "lichtleiter" to avoid the problem of inadequate illumination. This early endoscope directed light into the internal cavities in the human abdomen (called larparoscopy) and redirected to the eye of the observer. Therapeutic applications for the endoscope were realized in thoracic surgery as a result of prevalence of tuberculosis in the early 1900s. But only after the first solid state camera was introduced in 1982, could laparoscopy be brought into the main stream of general surgery, called "video-laparoscopy." Nothing had caused more revolution and had led to so many other developments during the past twenty years than the first laparoscopy cholecystectomy (gall bladder removal) on a human in 1987 [10]. Since then, this idea has developed into dozens of techniques for different general surgical procedures, such as cardiovascular surgery, colon and rectal surgery, gynecologic surgery, gastroenterologic surgery, neurosurgery, orthopedic surgery, thoracic surgery, otorhinolaryngology, urology etc.

During laparoscopic surgery, the surgeon uses small cylindrical tubes called trocars to enter the human body. The trocars allow entry of a video-telescope, called a laparoscope, to view the entire area of operation from inside the patient through a monitor. Accessory small trocars allow the introduction of long instruments necessary to perform surgery. Figure 1.1 shows the typical instrument arrangement for the cholecystectomy, which is the most frequently performed minimally invasive operation. The endoscopic camera is inserted into the abdomen through the navel and the instruments through small incisions with approximately 5–15 mm diameter. In the upper left corner, the endoscopic view is displayed by a monitor.

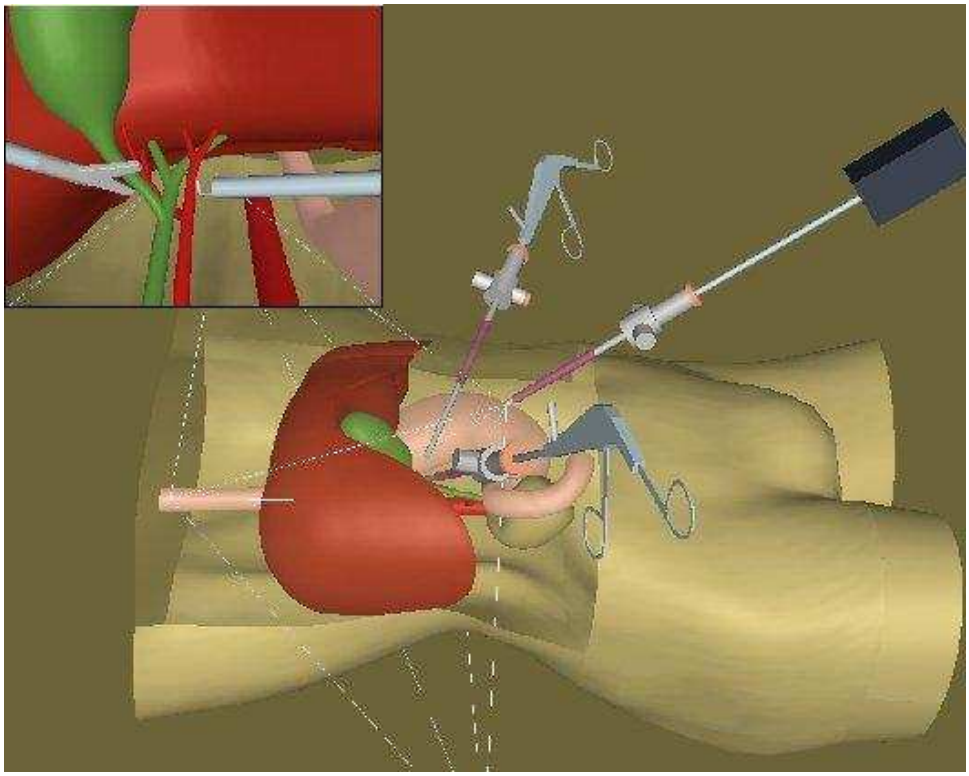

Figure 1.1. Typical instrument arrangement for the laparoscopy cholecystectomy (Courtesy Forschungszentrum Karlsruhe [1]).

In a typical laparoscopy, several small keyhole incisions are used in place of a significantly larger and more painful incision. The patient undergoes a similar operation by laparoscopy as by open incision. The advantages of laparoscopy include less pain, less scarring, a more rapid recovery, a decreased hospital stay and a quicker return to normal activities. However, during a laparoscopic procedure, the surgeons do not have access to the organs directly and have very limited operational space. What's more, the long-stemmed instrument is hard to manipulate and the two-dimensional video image cannot provide complete information about depth. Usually, the surgeons rely on tactile information or personal experience to a large extent for the hand-eye coordination. For the surgeons, laparoscopic surgery has a long learning curve and demands advanced skills. They must therefore receive extensive training before real surgeries to avoid accidents and reduce the complication and recurrence rate [12]. Traditionally, surgeons are trained on mannequins, cadavers, animals or by observing an experienced surgeon. While practicing on cadaver and live animals is very expensive and incurs criticism on ethics, mannequins are very unrealistic and inflexible. Therefore, it is necessary to build virtual reality (VR) based surgical simulators to train surgeons for laparoscopy surgeries.

1.1.2 VR-based Surgical Simulation

The primary purpose for a VR surgical simulation is training, especially for minimally invasive surgeries. To serve this purpose, the surgical simulator has to provide real-time interactive deformations (graphics) and force feedback (haptics) under different operations such as palpation, twist, drag, cut, suture, stapling, drain and cauterization [13]. To provide correct clues for effective training, not only should the deformations of the surface of the organ at different parts be consistent, but also the deformation and the force feedback should correspond to each other just as they do when surgeons operate on the real organs. For the consistency of deformations at different parts on the

object, non-physical models [14] [15] are feasible and have been widely used. But for the consistency between deformations and force feedback, and the consistency of force feedback for different deformations, physical models make more sense. At present, physically based deformable models are the first choice for surgical simulation. Deformable models are the most important part of a surgical simulator. On the one hand, they must be accurate enough not to cause distractive visual artifacts and misleading tactile clues, which results in very heavy computation. On the other hand, they must meet the real-time requirement, which is to update the graphics at a rate of 30 Hz and the haptics at rate of 1000 Hz [16]. The physical accuracy and speed of the deformable model must be balanced carefully to achieve these two goals.

One advantage of surgical simulation is that the surgeons can practice a surgery procedure as many times as needed. Another advantage is that it allows medical personnel to try different techniques and look at anatomy from perspectives that would be impossible during surgery. Moreover, simulated positions and forces can be recorded to compare with established performance metrics for assessment [17]. If an evaluation system is also built within the surgery simulator, the skill of the surgeons can then be evaluated objectively. This will drastically change the way of teaching surgeries.

1.1.3 Surgery Analysis, Planning and Rehearsal

Surgical simulation has been used to evaluate new surgery procedures and surgical tools for a long time. One example is the application of computational fluid dynamics (CFD) to design better artificial heart valves [18]. Doctors replace poorly functioning natural heart valves with prosthetic valves. But present-day designs are far from ideal. They can destroy blood platelets or permit a particle that has broken away from a blood clot to block a blood vessel. These complications likely come about because the blood is exposed to excessive stresses from the turbulent flow in the vicinity of the mechanical

prosthesis. Doctors also think the complex blood flow patterns around the valve may trigger a cellular response that can lead to the onset of heart diseases. But before the artificial valves can be redesigned, researchers need an in-depth understanding of the flow fields that the valves induce. Numerical modeling techniques have been developed to simulate the blood flow to help researchers better understand blood flow patterns through artificial mechanical heart valves. Manufacturers of heart valves can use the CFD technique to optimize their designs to minimize hazards to blood elements.

Surgical simulation can also be used to assess patients' conditions before operation. The simulator lets surgeons plan an operation by mapping it specifically to the patient's body and predicts possible surgery outcomes. One example is the application of CFD to plan heart-bypass surgery [19]. Surgeons simulate blood flow through the heart via CFD then program their findings into CAD software, where they design a patient-specific arterial bypass.

1.2 Thesis Organization

The thesis chapters are organized as follows. In chapter 2, we review the popular deformable models in the literatures. The pros and cons for each model are discussed and comparisons are made among the models.

In chapter 3, we present a new honeycomb model in consideration of a human organ as a combination of a fabric structure and incompressible fluid. The deformation of the model is achieved through the deformation of the cubic meshes and the rotation of them. In section 3.2 and 3.3, the governing equations for deformation and rotation of each cubic mesh are presented. In section 3.4, force feedback of the model is addressed. The implementation of this model is presented in section 3.5 and it turns out that this model is too slow to fit into real-time applications.

From chapter 4 to chapter 7, we aim to optimize the parameters of 1D, 2D and 3D mass-spring-damper (MSD) models to achieve physical accuracy based on continuum mechanics theory. This is the main contribution of this thesis. We start from the simplest case to solve this problem for more and more general cases.

In chapter 4, we first derive the ideal spring characteristics for the 1D structured MSD model in the parametric form by imposing the same bending stiffness on the MSD model as on a real beam. Then we use linear spring characteristics to approximate the nonlinear ideal characteristics. We find that it is essential to use preload on the springs of the 1D structured MSD model in order that it may have the same bending stiffness as the real beam. Further in section 4.3, this approach is extended to the 2D structured MSD model with equilateral triangle meshes.

In chapter 5, instead of deriving the ideal spring characteristics, we derive the optimal spring characteristics in the space of linear functions for the 1D and 2D structured MSD models. This approach has the advantage of being able to balance the modeling of the in-axis or in-plane stiffness and that of the out-of-axis or out-of-plane stiffness, and applicable to the rectangular meshes.

In chapter 6, the same rationale is applied to the 1D and 2D unstructured MSD models. Instead of deriving the parameters of the model explicitly, we derive a set of constraints on the parameters of the model and then solve the over-determined equation system under constraints to obtain the optimal parameters of the model. This approach can eliminate the boundary effect with previous approaches in chapter 4 and 5.

In chapter 7, we optimize the parameters of the 3D MSD model with both structured meshes and unstructured meshes by forcing the MSD model to have the same tensile stiffness in different directions in the 3D space. For unstructured meshes, we again obtain a set of equality constraints and one inequality constraint on the parameters of the model. The resulting equality system is usually over-determined. We treat the

inequality constraint as a hard constraint and apply the constrained least square method to solve the parameter of the MSD model. For structured meshes, we can obtain the parameters of the MSD explicitly in terms of the material properties and mesh geometry. The resulting MSD model is very accurate compared with the real object.

Finally, we introduce the inguinal hernia surgery simulator built in the Virtual Environment Lab (VEL) and suggest the future research to improve the simulator in chapter 8 and 9.

CHAPTER 2

DEFORMABLE MODELS IN THE LITERATRUE

2.1 Introduction

The finite element method (FEM) [20] has been successfully used in mechanical engineering for decades where its application has been strictly non-real-time. Therefore, it is the first consideration when we try to obtain accurate deformation results for human organs. But the computation requirement for FEM is very high and it has proven difficult to apply FEM in real-time applications. Thus, other deformable models are presented with the main goal to reduce computation to fit into real-time systems. Some people utilize pre-computation for FEM followed by minimal FEM in real time [21]. However, in view of the possible topology change during various surgical steps such as cut operation and suture operation, the applicable pre-computation for FEM is very limited, i.e. most of the computation has to be done in real time. In fact, for the same reason, pre-computation can hardly play much role in the other methods.

Over the past twenty years, many physically based deformable models have been proposed since Terzopoulos et al's seminal paper on elastically deformable models [22]. The most popular ones are the MSD model [23–30], FEM [20,31,32], the method of finite spheres (MFS) [33–35], the elasticity theory method [36, 37], the tensor-mass model [3], the quasi-static elastic model [3], the hybrid models [3, 38], the long element method (LEM) [39] etc. We will introduce these models one by one in the following.

2.2 The mass-spring-damper (MSD) Model

The MSD model is a physically based technique that has been used widely and effectively for modeling deformable objects. In this scheme, an object is modeled as a collection of point masses connected by springs in a lattice structure (Fig. 2.1). The forces from the springs are often linear but nonlinear springs can be used to model deformable objects such as human organs that exhibit nonlinear behavior.

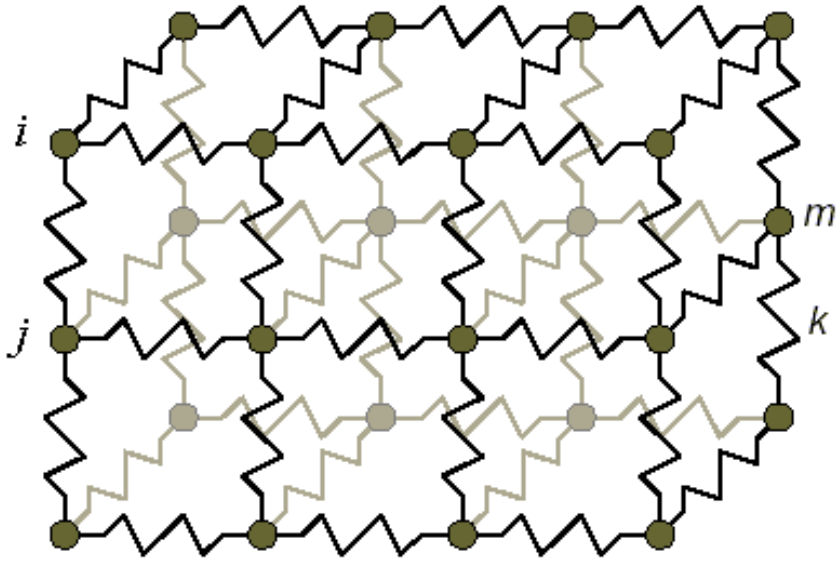

Figure 2.1. The MSD system structure [2].

In a dynamic MSD system, Newton's Second Law governs the motion of each mass point in the lattice structure:

$$m_i \ddot{\vec{p}}_i = -\gamma_i \dot{\vec{p}}_i + \sum_j \vec{f}_{ij} + \vec{f}_e \tag{2.1}$$

where m_i is the mass, $\vec{p}_i \in R^3$ is its position, $\vec{f}_{ij}$ is the force exerted on mass i by the spring between masses i and j, $\vec{f}_e$ is the sum of external forces (e.g. gravity or forces

applied by the user) acting on mass i, and γ_i is the damping coefficient for the resistance from the environment against motion of the mass.

If we use linear springs and introduce linear damping resistance for the relative motion between mass i and j, we have

$$\vec{f_{ij}} = k_{ij}(||\vec{p_i} - \vec{p_j}|| - L_{ij})\frac{\vec{p_i} - \vec{p_j}}{||\vec{p_i} - \vec{p_j}||} + \lambda_{ij}(\dot{\vec{p}}_j - \dot{\vec{p}}_i) \tag{2.2}$$

where L_{ij} is the rest length of the spring between mass i and j, k_{ij} is the Hooke's constant of the spring, λ_{ij} is the damping coefficient for the resistance against relative motion between mass i and j, which is used to model the internal energy loss during deformation of the continuum object.

From (2.1) and (2.2), we can have

$$\ddot{\vec{p}}_i = -(\frac{\gamma_i}{m_i} + \sum_j \frac{\lambda_{ij}}{m_i})\dot{\vec{p}}_i + \sum_j \frac{\lambda_{ij}}{m_i}\dot{\vec{p}}_j + \sum_j \frac{k_{ij}}{m_i}(\vec{p_i} - \vec{p_j}) - \sum_j \frac{k_{ij}}{m_i}L_{ij}\frac{\vec{p_i} - \vec{p_j}}{||\vec{p_i} - \vec{p_j}||} + \frac{\vec{f_e}}{m_i} \tag{2.3}$$

Based on the motion equation of each mass, we can obtain the motion equation system for the entire system with N masses.

$$\ddot{\vec{P}} + D\dot{\vec{P}} + K(\vec{P})\vec{P} = \vec{A}_e \tag{2.4}$$

where D and $K(\vec{P})$ are the $3N \times 3N$ damping matrix and stiffness matrix respectively; $\vec{P}$ is a column vector of the positions of the N masses; $\vec{A}_e$ is a column vector of the acceleration of the N masses due to external forces. Note that D and $K(\vec{P})$ are symmetric. The system described by (2.4) is a nonlinear system since $K(\vec{P})$ is a function of $\vec{P}$.

The second-order equation system above can be converted to a first-order equation system for the convenience of analysis or integration.

$$\dot{\vec{V}} = -D\vec{V} - K(\vec{P})\vec{P} + \vec{A}_e \tag{2.5}$$

$$\dot{\vec{P}} = \vec{V} \tag{2.6}$$

During simulation, the acceleration, velocity and position of each mass are only updated at discrete time points spaced by certain time step and constitute a discrete time system. We have several integration methods to solve the differential equation system above numerically among which the Euler's method is the simplest. If using the Euler's method and a time step of T, we have

$$\vec{V}(n+1) = (I - TD)\vec{V}(n) - TK(\vec{P}(n))\vec{P}(n) + T\vec{A}_e(n) \quad (2.7)$$

$$\vec{P}(n+1) = \vec{P}(n) + \vec{V}(n)T \quad (2.8)$$

As shown above, the MSD model is a simple model with easily understood dynamics. It has a small computation burden and is the only one among all the aforementioned models that is suitable for real-time applications for the current available computer resources. Since the MSD model has a simple discrete structure, all kinds of operations including cut and suture in the surgery can be handled easily. This model has been widely used in facial animation (both static and dynamic, two dimensional and simplified three dimensional [23–25]), animating fire, clouds and water [40], animation of artificial animals [41, 42], cloth draping [43, 44], garment animation [45–49] and recently in surgical simulation [29, 50]. To improve this model, a great deal of research has been carried out on various aspects—to refine the model adaptively [51], to update the Hooke's constants after refinement [30], to control the isotropy or anisotropy of the material [52], to improve its speed [28, 29, 53, 54], to eliminate the super elasticity phenomena [55], and to handle post-buckling instability for stable but responsive simulation [49]. All these research falls in two categories—for speed or for accuracy.

Despite the vast research performed on the MSD model, two problems with this model have not been completely solved as yet.

1. The MSD model cannot give exact deformation of real organs. In other words, proper values for the parameters of the model are not easy to specify.

2. Numerical instability phenomena often occur [28]. Fast and stable simulation is not easy to achieve.

A great deal of work has been done on the second problem to increase the speed of the model without incurring instability [28, 29, 49, 56]. Now the first problem is the main hurdle for the MSD model, which prevents further research work such as adaptive refinement to improve the model in terms of speed and accuracy.

Human organs are very complicated and the computation resources required for real-time deformations are too heavy for the current CPU capacity. One approach for solving this problem is to lay more emphasis on the area of interest, i.e., in the area where the operation is going on. The area of interest changes as the surgery progresses, so this idea has to be implemented adaptively. However, for the MSD model, it is difficult to assign parameters to ensure consistent behavior before and after refinement since we are not clear about the relationship between the parameters and topology of the model and the material properties of the organ. Upon solving the parameter assignation problem, we will be able to assign parameters to the MSD model before and after refinement (subdivision) independently according to the material properties and topology of the model. The consistency of the behavior of the MSD system will be automatically realized within certain tolerance.

Recently, J. Brown et al [29, 57] applied the MSD model to suture simulation, in which they take advantage of the local nature of the deformations to reduce calculations by using a "wave-propagation" technique that has automatic computation cutout (stoppage) when deformations become insignificant. They achieved an update frequency of 30 Hz for the deformations in suturing vessel surgery, which is compatible with real-time computer animation. But to provide realistic force feedback, it needs to be updated at a frequency of 1000 Hz. Although some interpolation can be used to make up the gap between the realized speed of an algorithm and 1000 Hz, a possible effect may be

that the user feels the simulation to be somewhat dull. According to [16], the human somatosensory system, which is a set of sensory systems associated with the body, can perceive vibrotactile stimuli up to 1000 Hz. Although the force control bandwidth for human is only 20–30 Hz, it is still important for the simulator to provide high frequency force feedback to make the simulation realistic.

2.3 The Finite Element Method

FEM [20] is the most accurate method for solving the deformation problem under certain boundary conditions. It decomposes the object of interest into small polygonal or polyhedral meshes. In each mesh, the field of deformation is expressed by a polynomial interpolated by the displacements of the vertices of the mesh. The governing equations of continuum mechanics are applied to each mesh to obtain a set of equations with displacements and external forces as unknowns. Usually, we only have interest in part of the unknowns, so we can condense the matrix equation to solve those unknowns to reduce computation [31].

For FEM, integration over the mesh is calculated using Gauss product rules to reduce computation. Since the interpolation functions (shape functions) are polynomials, we can obtain accurate integration by using only a small number of integration points. Usually the integration is reduced to only a small number of multiplications and additions.

The accuracy of the deformations obtained through FEM depends on the type of polygon or polyhedron, the size of it and the number of interpolation points used. We need to notice that the number of interpolation points is not necessarily the number of vertices. We can increase the number of meshes (h-refinement) and/or the number of interpolation points of each mesh (p-refinement) to enhance accuracy. Note that the shape functions are chosen to ensure this property—the deformation results will converge to the real values as we use h-refinement and/or p-refinement. To get a good trade-off

between accuracy and computation, we need to choose meshes of proper size which corresponds to certain number of meshes, and suitable number of interpolation points which corresponds to certain type of mesh and certain number of interpolation points on the mesh.

The meshes used most frequently are triangles in two dimensions (2D) and tetrahedrons in three dimensions (3D). Usually several thousand meshes are used to obtain accurate results for an uncomplicated object under a simple boundary condition. The corresponding FEM has too heavy a computation burden to achieve accurate deformations in real-time. Generally, FEM is not suitable for real-time applications for the present CPU capacity. But if there is no topology change, i.e. cut or suture operation, it is possible to obtain real-time deformations by using pre-computation [21] [32] [58] because the stiffness matrix in the FEM scheme does not change.

2.4 The Finite Sphere Method

The method of finite spheres (MFS) [33–35] is a meshless method. It was developed by S. De and K. J. Bathe to overcome the meshing burden for methods like FEM. This method uses a set of points instead of meshes to solve the governing equations. When a surgical tool touches the tissues, a set of points is sprinkled locally around the tool tip and a sphere with a finite radius is located at each sprinkled point. Just as in the FEM method, shape functions [20] are used to approximate deformation fields. The difference is that in the MFS method, we have to use rational functions instead of polynomials. Although the rational functions are carefully chosen to enhance the computation efficiency [34], they still lead to more computation in the integration part because of more interpolation points than in the polynomial case, which is obviously a disadvantage. Although J. Kim, S. De et al claimed the finite sphere method could give good local deformation comparable to FEM [35], it is still not convincing that this

method could give accurate deformation results in real time, because the number of the points they used in their simulation is too small (34 points) compared to that in the finite element method (4045 nodes). For MFS to be really applicable for the real-time application, further work needs to be done to reduce the computation. Besides, the current MFS is limited to point interactions and needs to be extended to handle general interactions.

Since this method is developed intending to overcome one of the main shortcomings of the traditional FEM method, it has potential to be a feasible method.

2.5 The Elasticity Theory Method

This method [36, 59] is based on the Hooke's law, which relates the stress tensor and the strain tensor, and it uses a discrete approximation of derivative operators on irregular sample points [37]. It allows space-time adaptation to distribute computation resources in an efficient way and ensures numerical stability. This method can handle cut operation and suture operation just like the MSD model.

In this method, we spray sampling points inside the organ of interest, just like in the finite sphere model. According to elasticity theory, for every sampling point, we have

$$\rho\vec{a} = \mu\nabla^2\vec{d} + (\lambda+\mu)\nabla(div\vec{d}) \tag{2.9}$$

where λ and μ are Lame coefficients characterizing the stiffness of a material, ρ is the material density, $\vec{a}$ is the acceleration of the point and $\vec{d}$ is the displacement.

In this method, a scale-dependent umbrella operator is used to approximate the Laplacian operator.

$$\nabla^2\vec{d} = \frac{2}{\sum_{j \text{ neighbors}} l_{ij}} \sum_{j \text{ neighbors}} \frac{\vec{d_j} - \vec{d_i}}{l_{ij}} \tag{2.10}$$

where $l_{ij} = |\vec{d_j} - \vec{d_i}|$ is the distance between sample point i and j obtained in the previous update step.

To provide a stable pair of operators for simulation, the gradient-of-divergence operator is approximated in the following way.

$$\nabla(div\vec{d}) = \frac{2}{\sum_{j \text{ neighbors}} l_{ij}} \sum_{j \text{ neighbors}} \frac{[(\vec{d_j} - \vec{d_i}) \cdot \vec{l}_{ij}]\vec{l}_{ij}}{l_{ij}^3} \tag{2.11}$$

where $\vec{l}_{ij} = \vec{d_j} - \vec{d_i}$ is the vector from sample point i to sample point j obtained in the previous update step.

The implementation of this method is as straight forward as that of the MSD model. The recursive process is listed as follows:

1. Calculate the Laplacian and gradient-of-divergence operator;
2. Calculate the acceleration of each sample point using 2.9;
3. Integrate the acceleration over a time step dt to update positions and velocities.

This method uses both space and time adaptation to concentrate computation where and when required. The space refinement criterion is

$$h^2|\nabla^2\vec{d}| \geq \varepsilon_{max} \tag{2.12}$$

The simplification criterion is

$$h^2|\nabla^2\vec{d}| < \varepsilon_{min} \tag{2.13}$$

where h represents the shortest distance between the particle and its neighbors. ε_{max} and ε_{max} are refinement threshold and simplification threshold respectively.

The time adaptation is constrained by the following two inequations.

$$dt < h\sqrt{\frac{\rho_0}{\lambda + 2\mu}} \tag{2.14}$$

$$|adt| < \Delta v_{max} \tag{2.15}$$

where ρ_0 is the rest density of the material and Δv_{max} is the threshold for the change of velocity.

This method also uses internal damping to add realism just like the MSD model. In [37], Debunne et al implemented a system and achieved a 30 Hz update rate without force feedback. Later in [60], force feedback is added to the simulation system. For a system of a few hundred sampling points, real-time interaction with graphics and haptics is achieved. One problem with this method is that the operator approximation is very sensitive to the distribution of the sampling points. The sampling points have to be chosen very carefully. Another problem with this model is that it is not accurate for large deformation.

2.6 The Tensor-mass Model

The tensor-mass model [3] meshes the organs with conformal tetrahedrons. Just like the MSD model, it also discretizes the distribution mass in the object to lumped mass on the mesh points P_i $(i = 1, 2, \cdots, N)$. The governing equation for the motion of the mesh points is also based on the Newtonian Law.

$$m_i \frac{d^2 \vec{P}_i}{dt^2} = \gamma_i \frac{d\vec{P}_i}{dt} + \vec{F}_i \tag{2.16}$$

The difference is that $\vec{F}_i$ is obtained through the energy-based finite element method. The computation of this linear elastic force can be decomposed into four steps:

1. Define the interpolation equation (shape functions) that gives the displacement vector at any point inside a tetrahedron T_k as a function of the four displacement vectors at each vertex;
2. Express the elastic energy of a tetrahedron as a function of these four displacement vectors;
3. Compute the elastic force produced by tetrahedron T_k and apply it to vertex P_i;
4. Add the $\vec{F}_{iT_k}$ produced by all the tetrahedrons connected to vertex P_i together to obtain $\vec{F}_i$.

Through the first three steps above, we can obtain the force $\vec{F}_{T_i(j)}$ applied on vertex $P_{T_i(j)}$.

$$\vec{F}_{T_i(j)} = \sum_{k=0}^{3} K_{jk}^{T_i}(\vec{P}_{T_i(k)} - \vec{P}_{T_i(k)}^{0}) \tag{2.17}$$

where $K_{jk}^{T_i}$ are stiffness matrices (tensors). $K_{jk}^{T_i}$ can be computed using the Lame coefficients and the normal vectors of the four surfaces of the tetrahedron T_i.

$$K_{jk}^{T_i} = \frac{1}{36V(T_i)}\Big(\lambda_i M_k^{T_i}(M_j^{T_i})^T + \mu_i M_j^{T_i}(M_k^{T_i})^T + \mu_i (M_j^{T_i})^T M_k^{T_i} I_3\Big) \tag{2.18}$$

where $V(T_i)$ is the volume of the tetrahedron, $M_k^{T_i}$ and $M_j^{T_i}$ are the normal vectors of the surfaces of the tetrahedron, λ_i and μ_i are the Lame coefficients of the material for tetrahedron T_i.

From above, we know that $\vec{F}_i$ is computed locally, since it is only related to the tetrahedrons connected to vertex P_i. So this method can handle cut operation and suture operation with ease, just like the MSD model. Compared with the MSD model, the tensor-mass model computes force by continuum mechanics and therefore is independent of the mesh topology (we know the MSD model is sensitive to the mesh topology). When there is cut operation or suture operation, the tensor-mass model can provide more realistic interactions. But one drawback of the tensor-mass method is that it is only accurate for small displacements. The $\vec{F}_i$'s are computed locally, so they won't be zero under pure rigid transformation without deformation, which is not correct.

2.7 The Hybrid Elastic Model

The hybrid elastic model [3] combines a quasi-static pre-computed linear elastic model and several tensor-mass models and takes advantages of the good property of both types of model. In section 2.1, we have mentioned that pre-computation is only suitable for the situation without cut (or tear) and suture and by using pre-computation, we can achieve accurate results in real time with ease. So it is a good idea to use one model that

makes full use of pre-computation for the part where there is no cut operation or suture operation, and use another model that can handle cut operation and suture operation to model each of the parts where cut or suture operation is performed. Although in the real surgery, we may not know in advance where to cut or suture, in the simulation, we can arrange beforehand where to cut or suture. So the idea mentioned above is feasible. In this scenario, where several models coexist, different models share some boundaries. One model may provide the boundary conditions for another model. Since we use different models, there may be some artifacts in the areas close to the common boundaries between different models. But if we choose two models with close theoretical foundations and thus similar properties, it is possible for us to reduce the artifacts to an acceptable level. The two constitutional models of the hybrid elastic model follow the same physical law—the Hooke's Law, so the combination of these two models should behave like a global linear elastic model. Here we need to notice that the combination of other models is also possible for a different hybrid model system [38].

In section 2.6, we have described the tensor-mass model. This model is applied for the parts where there is a cut or suture operation. We use a quasi-static pre-computed elastic model for the part in which there is no cut or suture operation. The quasi-static pre-computed elastic model is also based on elasticity theory—the Hooke's Law. In this method, the object is decomposed into tetrahedrons and elasticity energy is computed for each tetrahedral element. By applying the principle of least action, the state of equilibrium of the model is reached when the overall elasticity energy reaches its minimum. So this method is actually an energy-based finite element method. Just like other variants of the finite element method, the calculated results are very accurate and pre-computation can be used to speed up the algorithm to fit into real-time applications [61]. However, similar to the tensor-mass model, the quasi-static pre-computed linear elastic model is only suitable for small deformations. The main difference between the quasi-static pre-

computed elastic model and the tensor-mass model is that the motion of the elements in the former model is calculated by a continuous finite element method, which uses pre-computation and is more accurate, while in the latter model, it is obtained through a discrete lumped mass method, which is less accurate but can handle cut and suture operations.

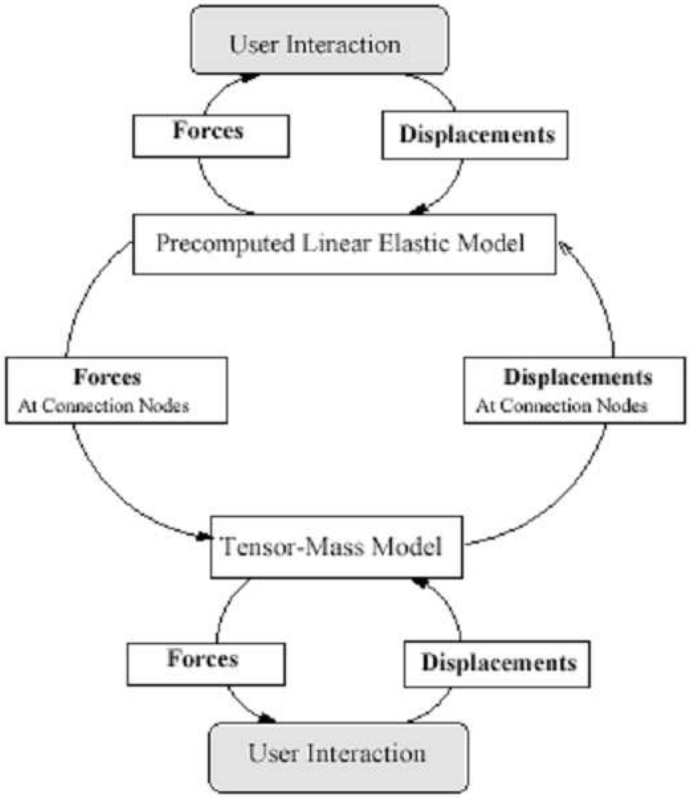

Figure 2.2. Interaction loop for the hybrid elastic model [3].

The interaction loop for the hybrid elastic model is shown in the Fig. 2.2. The pre-computed elastic model is updated based on the imposed displacements on its boundary—both the natural boundary and the common boundaries shared with the tensor-mass models. The deformations of the pre-computed elastic model arise from both user inter-

actions and the motion of the nodes shared with the tensor-mass models. At this stage, the resulting force at the shared nodes are calculated to provide boundary values for the tensor-mass models. After the pre-computed elastic model is updated, each tensor-mass model is updated based on the forces applied on the shared nodes and the displacements imposed by user interactions. At this stage, the tensor-mass models provide boundary displacements for the pre-computed elastic model at the next loop.

The hybrid elastic model is implemented to simulate a hepatectomy in [3]. The artifacts close to the common boundaries of the two types of models are very small and are not perceivable to human eye. So this model is a suitable for surgical simulators. But this model has the drawback that it is only accurate for small deformations.

2.8 Conclusions

The comparison of all the aforementioned models in terms of computation efficiency, applicability for large deformations, possibility for precomputation in case of cut and/or suture operations and theoretical foundation is shown in Table 2.1.

Table 2.1. Comparison between the deformable models

Deformable models	Computation efficiency	Large deformation	Precomputation with cut/suture	Theory foundation
MSD model	Real time	Yes	N/A	Incomplete
FEM	Very slow	No	No	Solid
MFS	Slow	No	No	Solid
Elasticity theory method	real time	No	N/A	Solid
Tensor-mass model	Barely real time	No	Yes	Solid
Quasi-static elastic model	Barely real time	No	No	Solid
Hybrid elastic model	Barely real time	No	Yes	Solid

Among the models discussed above, the MSD model is a complete discrete model in which the continuous material is discretized into lumped masses and the distributed interactions are discretized into springs. Due to the discretization of both aspects, the MSD model is the simplest and easiest one to implement, and it can handle all kinds of user interactions. However, a simple model is not necessarily an efficient one. The constraints for the continuous system sometimes are not easily transformed into constraints for the corresponding discrete system, which means the MSD model is not efficient in handling some constraints [2].

The elasticity theory method is a complete continuous model. The key point of the elasticity theory method is the approximation of the Laplacian operator and divergence of the gradient operator by an umbrella operator. If this approximation were accurate enough without significant number of sampling points, the elasticity theory method would be an efficient model.

FEM is a continuous model, but is not purely continuous. The discrete component in this method lies in the meshing step, which causes the deformation field to be only C^0 continuous across the mesh boundaries. FEM is accurate only when the discontinuity of the derivative of the deformation field across the mesh boundaries is not large. With regard to speed, optimization techniques such as condensation and pre-computation have been applied to increase the speed of FEM [21]. But they are not compatible with the topology change entailed by cut or suture operation where the stiffness matrix changes [62].

MFS is a method very close to FEM. The main difference is that MFS is a meshless method and the shape functions are rational functions instead of polynomials.

The tensor-mass model is a semi-continuous model. The interactions are calculated on a continuous base (elasticity theory). The material mass is lumped onto the vertices of the mesh to establish the motion equations. This model can handle cut and suture

operations in a way as efficient as the MSD model. Under small deformations, it can replace the MSD model and is more accurate. But it is not suitable for large deformations. The quasi-static pre-computed elastic method is actually an energy based finite element method. It is also only suitable for small deformations. Combined with the tensor-mass model, it forms a hybrid model, which can take advantage of pre-computation and simultaneously can handle cut and suture operations.

To achieve a real-time surgical simulation, effective modeling of the organs involved is of paramount importance. However, none of the aforementioned models is satisfactory in the sense of accuracy or speed as yet. Since human organs themselves are very complicated and the computation resources are insufficient, it is natural to apply the adaptive refinement technique mentioned in section 2.2 to lay more emphasis on the area of interest. The adaptation refinement concept is not new. However, it is not clear how to keep consistent properties for some of the models before and after refinement. Particularly, for the discrete models, it is not clear how to set the parameters for the models before and after refinement to ensure they deform the same under the same load condition. For the continuous models, it is not clear how to introduce new meshes or sampling points for the models to ensure consistency before and after refinement.

CHAPTER 3

HONEYCOMB MODEL

3.1 Introduction

In this chapter, we present a model [63] that takes volume preservation as a basic principle and views the organ as a combination of honeycomb fabric structure and fluid filling in the structure, which can handle large deformation and the phenomenon of high coupling between the stresses of human organs in different directions and is hopeful to be more realistic. Since speed and implementation issues are somewhat dependent on the current state of computer hardware technology, we set this aspect aside as we examine the possibility of a versatile soft tissue model.

This model is hypothesized in consideration of a human organ as a combination of a fabric structure and incompressible fluid. The whole organ is discretized into small cubic cells, of which the six sides are the abstraction of the fabric tissue, and incompressible fluid inside models the fluid contained in the organ. We say two cells are adjacent if they contact each other on some side. The contacting sides of two adjacent cells adhere to each other and form one patch of the honeycomb wall shared by the two cells and all these walls form a honeycomb shaped structure. Adjacent cells can only have tangential relative motion and interact in three mutually perpendicular directions—the normal direction of the contacting side and the two tangential directions of that side. The deformation of each cubic cell is decided by the equilibrium condition of all its six sides. In section 3.2, we will discuss in detail the deformation of an individual cell. In addition to the axial deformation, each cell will rotate along its central axes under the torque produced by the tangential forces acting on its sides. We will discuss this

problem in section 3.3. In section 3.4, we calculate force feedback on the instrument when the user operates on one cell of the organ with it. For the whole organ, the deformation of one cell propagates to its adjacent cells through its contacting sides, which causes the complementary deformation of the adjacent cells, and further of the whole structure. The interactions between the boundary cells and the external world constitute the boundary conditions of the global deformation problem. In section 3.5, we will discuss the implementation of the deformation of the whole organ and show the simulation result. Finally, in section 3.6, we come to a conclusion for this model.

3.2 The Deformation of an Individual Cell

The deformation analysis of an individual cell is shown in Fig. 3.1 left. We assume the cell keeps its cubic shape during deformation. In other words, the cubic mesh will only change its dimensions in three directions. When some sides of the cell are pressed or dragged, we call these sides "active". The other sides are called passive sides.

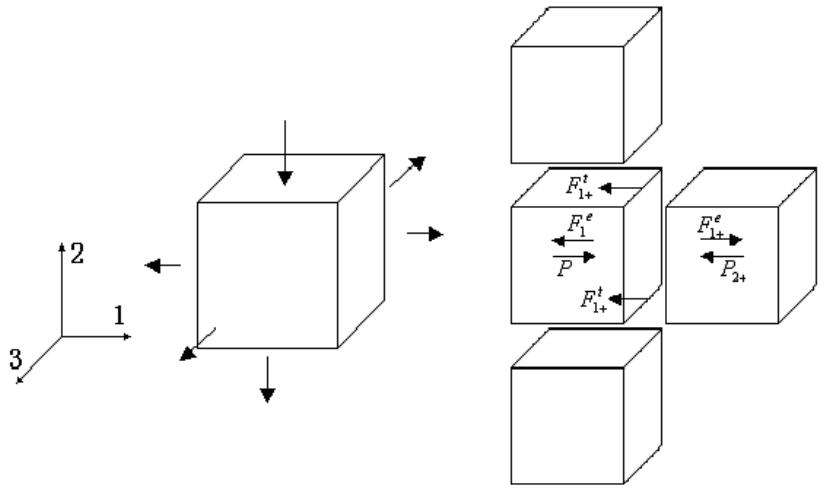

Figure 3.1. Left: deformation of an individual cell; right: lateral interaction forces that generate torque along the third axis.

The amount of displacement of each passive side in its normal direction depends on the equilibrium condition of the corresponding honeycomb wall. The internal force imposed on each wall in its normal direction consists of five components. Two components result from the stretch (or compression) of the four lateral sides of each of the two cells, which share that wall. The inner pressure of the two cells produces two other components. The fifth component comes from the four walls which are originally in the same plane around the wall of interest (we call them co-planar adjacent walls later). Fig. 3.1 right shows the internal forces acted on the wall corresponding to the side of the cell in the positive first axis. The first two component forces $\vec{F}_1^e$ and $\vec{F}_{1+}^e$ are related to the stiffness of the two cells in the corresponding direction. For each cell, we can use a 3×4 stiffness matrix (k_{ij}) to represent its stiffness. Each row of the matrix represents the four elastic coefficients for the four lateral sides of the cell in the direction of the corresponding axis. The elastic coefficient for the cell in the direction of the ith axis is the sum of the ith row of the matrix, i.e.

$$k_i = \sum_{j=1}^{4} k_{ij} \tag{3.1}$$

We need to note that if some lateral side is an active side and the external tangential force acted on it is not zero in the normal direction of the side of interest, then the elastic force is not the only force exerted by the lateral sides. The external tangential force also contributes part of the force exerted by the lateral sides. This force component is not shown in Fig. 3.1 right, and we use F_i^l to represent it.

When one wall changes its position in its normal direction, its four coplanar adjacent walls hold it back. We assume this tangential resistant force to be proportional to the amount of the relative displacement. The interaction coefficients between the three walls and their coplanar adjacent walls can be represented by a 3×4 matrix (t_{ij}^+) for the three walls of a cell in the three positive axis directions. Each row of the matrix repre-

sents the elastic coefficient for the interaction of the walls of the cell in the ith positive axis direction between its four coplanar adjacent walls. We have the same argument for the three walls of a cell in the three negative axis directions.

Each cell is associated with a local coordinate system, whose three axes are the three central axes of the cell. We assume the local coordinate system can be obtained by the translation of the global coordinate system followed by a rotation of angle α about the first axis, β about the second axis and γ about the third axis. Then α, β and γ together with the position of the six sides of the cell in the local coordinate system determine the state of the cell. We also assume that the positive third axis of the global coordinate system is in the opposite direction to gravity. For a cell surrounded by cells on its six sides, we can form equilibrium equation for each passive side of the cell based on the analysis above. Here, we only derive the equilibrium equation for the wall corresponding to the positive first axis side when it is a passive side. According to Fig. 3.1 right, the elastic force exerted by the lateral sides of the current cell is

$$F_1^e = k_1(l_1 + d_1^+ + d_1^- - l_{1r}) \tag{3.2}$$

where, d_1^+, d_1^- are the displacements of the sides of the current cell in the positive and negative first axis respectively, l_1, l_{1r} are the length and rest length of the current cell along the first axis respectively.

The elastic force exerted by the lateral sides of the cell contacting the current cell is

$$F_{1+}^e = k_1^+(l_1^+ - d_1^+ + d_{1+}^+ - l_{1r}^+) \tag{3.3}$$

where, k_1^+ are the stiffness along the first axis of the cell next to the current cell in the positive direction of the first axis, d_{1+}^+ is the displacement of the positive first axis side of the adjacent cell in the positive first axis direction, l_1^+ is the length along the first axis

of the cell next to it in the positive direction of the first axis and l_{1r}^{+} is the corresponding rest length.

The tangential resistant force from the four coplanar adjacent walls is

$$F_{1+}^{t} = \sum_{k=1}^{4} t_{1k}^{+}(d_1^{+} - d_{1k}^{+}) \tag{3.4}$$

where d_{1k}^{+} $(k = 1, 2, 3, 4)$ are the displacements of the sides in the positive direction of the first axis of the four adjacent cells on the lateral sides of the current cell.

The force caused by the inner pressure of the current cell is

$$F_{P1}^{+} = \frac{1}{2}\big(P + \frac{1}{2}\rho g(l_1 + d_1^{+} + d_1^{-})\sin\beta\big)\big(\frac{V}{l_1 + d_1^{+} + d_1^{-}} + \frac{V}{l_1^{+} + d_{1+}^{+} - d_1^{+}}\big) \tag{3.5}$$

where P is the inner pressure of the current cell at its center, V is the volume of the cell, ρ is the density of the fluid, g is the gravity constant, β is the rotation angles of the current cell around the second axis.

And the force caused by the pressure of the cell contacting the current cell on the side of interest is

$$F_{P1+}^{-} = \frac{1}{2}\big(P_1^{+} - \frac{1}{2}\rho g(l_1^{+} + d_{1+}^{+} - d_1^{+})\sin\beta_1^{+}\big)\big(\frac{V}{l_1 + d_1^{+} + d_1^{-}} + \frac{V}{l_1^{+} + d_{1+}^{+} - d_1^{+}}\big) \tag{3.6}$$

where, P_1^{+} is the inner pressure of the cell next to it in the positive first axis direction, and β_1^{+} is the rotation angle around the second axis of the cell adjacent to the current cell in the positive direction of the first axis.

Another possible force is the external force exerted on the lateral sides of the two cells in the normal direction of the side of interest.

$$F_1^{l} = \frac{1}{2}\sum_{k=1}^{4}(f_{1k} + f_{1k}^{+})F \tag{3.7}$$

where, f_{1k}, f_{1k}^{+} are the tangential forces acting on the lateral sides of the two cell in the normal direction of the side of interest respectively.

Now we can get the equilibrium equation of this wall.

$$\frac{1}{2}\big(P_1^+ - \frac{1}{2}\rho g(l_1^+ + d_{1+}^+ - d_1^+)\sin\beta_1^+\big)\big(\frac{V}{l_1 + d_1^+ + d_1^-} + \frac{V}{l_1^+ + d_{1+}^+ - d_1^+}\big) +$$
$$k_1(l_1 + d_1^+ d_1^- - l_{1r}) + \sum_{k=1}^{4} t_{1k}^+(d_1^+ - d_{1k}^+) = k_1^+(l_1^+ - d_1^+ d_{1+}^+ - l_{1r}^+) + \frac{1}{2}\sum_{k=1}^{4} f_{1k} +$$
$$\frac{1}{2}\big(P + \frac{1}{2}\rho g(l_1 + d_1^+ + d_1^-)\sin\beta\big)\big(\frac{V}{l_1 + d_1^+ + d_1^-} + \frac{V}{l_1^+ + d_{1+}^+ - d_1^+}\big) \tag{3.8}$$

Assume $d_i^+, d_i^- \ll l_i$ and $d_{i+}^+, d_{i-}^+ \ll l_i^+$, then we can get

$$(k_1 + k_1^+ + t_1^+)d_1^+ + \Big(k_1 - \frac{1}{4}\rho g\sin\beta\big(\frac{V}{l_1} + \frac{V}{l_1^+}\big)\Big)d_1^- - \frac{1}{2}\big(\frac{V}{l_1} + \frac{V}{l_1^+}\big)P =$$
$$\frac{1}{2}\sum_{k=1}^{4} f_{1k} + \frac{1}{2}P_1^+\big(\frac{V}{l_1} + \frac{V}{l_1^+}\big) + k_1^+(l_1^+ + d_{1+}^+ - l_{1r}^+) - k_1(l_1 - l_{1r}) +$$
$$\frac{1}{4}\rho g[l_1\sin\beta + (l_1^+ + d_{1+}^+)\sin\beta_1](\frac{V}{l_1} + \frac{V}{l_{1+}}) + \sum_{k=1}^{4} t_{1k}^+ d_{1k}^+ \tag{3.9}$$

where $t_1^+ = \sum_{k=1}^{4} t_{1k}^+$.

Although the equation above is developed for the cells surrounded by cells on all its sides, it is also valid for those cells on the boundary. For the cell that has some sides on the boundary, we impose the boundary condition on the equilibrium equation.

Since the volume will be preserved for each cell, we have

$$\prod_{i=1}^{3}(l_i + d_i^+ + d_i^-) = \prod_{i=1}^{3} l_i = V \tag{3.10}$$

When $d_i^+, d_i^- \ll l_i$, it can be approximated as

$$\frac{d_1^+ + d_1^-}{l_1} + \frac{d_2^+ + d_2^-}{l_2} + \frac{d_3^+ + d_3^-}{l_3} = 0 \tag{3.11}$$

For a cell having m active sides, it has $6-m$ passive sides. The unknowns are the displacements of the passive sides and the inner pressure of the cell. We can obtain $6-m$ equilibrium equations for the passive sides. Plus the volume preservation equation, we have $7-m$ equations for $7-m$ unknowns. So we can get a unique solution.

3.3 Rotation of the Cubic Cell

The cell of the deformable object not only deforms in its axial directions, but can also rotate around its three axes as a whole driven by nonzero active torque produced by the tangential interactions between cells. These rotations will change the transformation angles α, β, γ between the local coordinate system and the global coordinate system.

To calculate the rotation angle around the third axis, we need to first calculate the active torque. Fig. 3.2 shows the interaction forces between the cell of interest and its adjacent cells that produce active torque in the direction of the first axis.

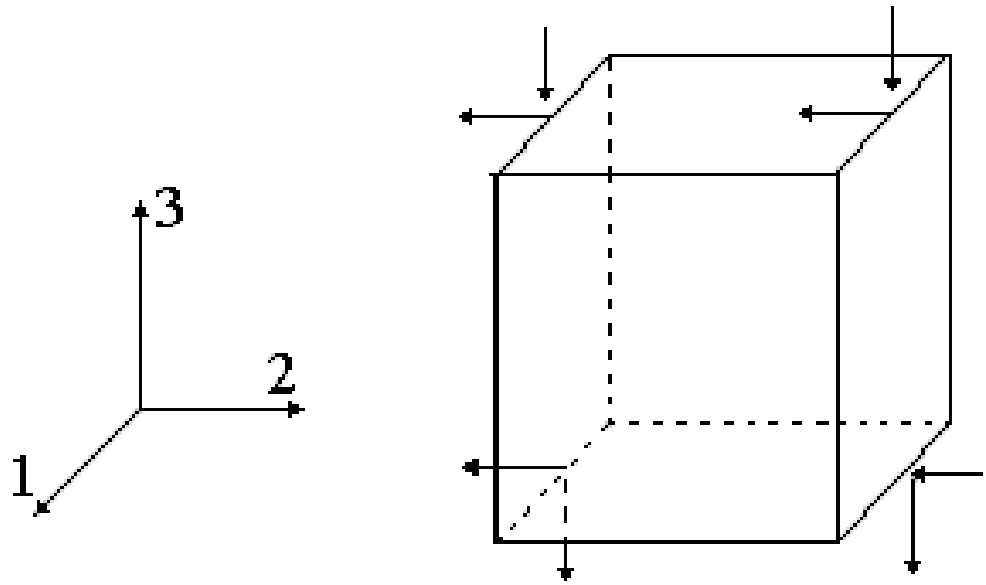

Figure 3.2. Lateral interaction forces that generate torque along the third axis.

According to Fig. 3.2, we can obtain the active torque in the positive direction of the first axis.

$$\begin{aligned} T_1 &= \frac{l_3}{2}[t_{21}^{+}(d_2^{+}-d_{21}^{+})-t_{21}^{-}(d_2^{-}-d_{21}^{-})-t_{23}^{+}(d_2^{+}-d_{23}^{+})+t_{23}^{-}(d_2^{-}-d_{23}^{-})]+ \\ &\quad \frac{l_2}{2}[t_{34}^{+}(d_3^{+}-d_{34}^{+})-t_{34}^{-}(d_3^{-}-d_{34}^{-})-t_{32}^{+}(d_3^{+}-d_{32}^{+})+t_{32}^{-}(d_3^{-}-d_{32}^{-})] \end{aligned} \tag{3.12}$$

In general, this torque is not zero and it will cause the cell to rotate around the first axis. When the cell rotates around the first axis relative to its adjacent cells, it will encounter resistance from them (Fig. 3.3).

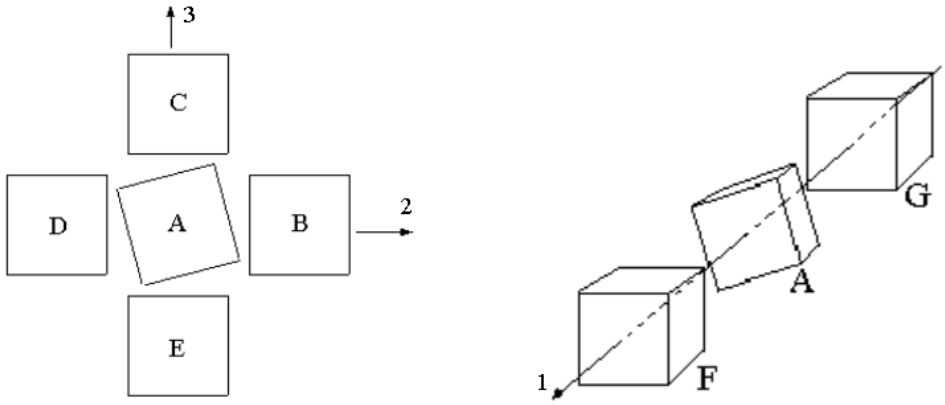

Figure 3.3. Left: resistance from lateral adjacent cells; right: resistance from the front and back cells.

In Fig. 3.3, we analyze the resistant torque due to the relative rotation around the first axis between cell A and C. One component of the torque comes from the uneven elongation of the joint part between cell A and C. We use the average of the elastic constants of the two adjacent cells along the direction of the third axis to approximate the elastic constant of the joint part, i.e.

$$k_J = \frac{1}{2}(k_3 + k_3^+) \tag{3.13}$$

Then the resistant torque is

$$T_{AC1} \approx \frac{1}{3}(\alpha - \alpha_3^+)k_J l_2^2 = \frac{1}{6}(\alpha - \alpha_3^+)(k_3 + k_3^+)l_2^2 \tag{3.14}$$

where α_3^+ is the rotation angle around the first axis of the cell next to the current cell in the positive direction of the third axis.

Another component results from the relative displacements between the negative third axis sides of cell C and the positive third axis sides of cell A. The corresponding torque is

$$T_{AC2} \approx \frac{l_3^2}{2}(t_{21}^+ + t_{21}^-)(\alpha - \alpha_3^+) \tag{3.15}$$

Thus the total resistant torque from cell C due to the relative rotation around the first axis is

$$T_{AC} \approx \frac{1}{6}(\alpha - \alpha_3^+)(k_3 + k_3^+)l_2^2 + \frac{l_3^2}{2}(t_{21}^+ + t_{21}^-)(\alpha - \alpha_3^+) \tag{3.16}$$

Similarly we can obtain T_{AB}, T_{AD} and T_{AE}.

In Fig. 3.3 right, through similar analysis as above, we have

$$T_{AF} = \frac{1}{6}(\alpha - \alpha_1^+)[(t_{22}^+ + t_{22}^-)l_3^2 + (t_{31}^+ + t_{31}^-)l_2^2] \tag{3.17}$$

$$T_{AG} = \frac{1}{6}(\alpha - \alpha_1^-)[(t_{24}^+ + t_{24}^-)l_3^2 + (t_{33}^+ + t_{33}^-)l_2^2] \tag{3.18}$$

Now we can obtain the resistance torque around the first axis.

$$\begin{aligned} T_{1r} &= T_{AB} + T_{AC} + T_{AD} + T_{AE} + T_{AF} + T_{AG} \\ &= \frac{1}{6}(\alpha - \alpha_3^+)(k_3 + k_3^+)l_2^2 + \frac{1}{6}(\alpha - \alpha_3^-)(k_3 + k_3^-)l_2^2 + \\ &\quad \frac{1}{6}(\alpha - \alpha_2^+)(k_2 + k_2^+)l_3^2 + \frac{1}{6}(\alpha - \alpha_2^-)(k_2 + k_2^-)l_3^2 + \\ &\quad \frac{1}{6}[(t_{22}^+ + t_{22}^-)l_3^2 + (t_{31}^+ + t_{31}^-)l_2^2] + \frac{1}{6}[(t_{24}^+ + t_{24}^-)l_3^2 + (t_{33}^+ + t_{33}^-)l_2^2] + \\ &\quad \frac{l_2^2}{2}[(t_{32}^+ + t_{32}^-)(\alpha - \alpha_2^+) + (t_{34}^+ + t_{34}^-)(\alpha - \alpha_2^-)] + \\ &\quad \frac{l_3^2}{2}[(t_{21}^+ + t_{21}^-)(\alpha - \alpha_3^+) + (t_{23}^+ + t_{23}^-)(\alpha - \alpha_3^-)] \end{aligned} \tag{3.19}$$

The equilibrium condition about torque in the direction of the first axis requires $T_1 = T_{1r}$, from which we can obtain the rotation angle α around the first axis. In the same way, we can update values for β and γ.

3.4 Force Feedback

The interaction between the instrument and the deformable object consists of a set of collisions between the instrument and the cubic cells of the deformable object. The force feedback on the instrument for each of those collisions has three components. One is in the normal direction of the surface and the other two are in the two tangential directions. These three components are in alignment with the three axes of the local coordinate system respectively. Here we illustrate the situation when the instrument operates on the side of the cell in the positive direction of the first axis direction. The normal reaction force can be calculated through the equilibrium condition of the interacting side of the cell as follows.

$$N_1^+ = (P - \frac{1}{2}\rho g l_1 \sin\beta)\frac{V}{l_1} + k_1(l_1 - l_{1r}) + \sum_{k=1}^{4} t_{1k}^+ d_{1k}^+ - t_1^+ d_1^+ \tag{3.20}$$

Assume the contact point of the instrument does not slide on the side of the cell, and then the two tangential reaction forces result from the static friction between the contact point of the instrument and that of the cell. Suppose the static friction force is proportional to the relative displacement d_r of the contact point of the instrument and the corresponding central axis of the cell. Here, we illustrate how to calculate the tangential force along the second axis. We need to first calculate the relative displacement d_{2r}. Suppose the displacements of the two sides that are vertical to the second axis are d_2^+ and d_2^-, and the displacement of the contact tip of the instrument along the second axis is d_{2I}. Then,

$$d_{2r} = d_{2I} - \frac{d_2^+ - d_2^-}{2} \tag{3.21}$$

The friction force along the second axis is

$$F_t^2 = -\frac{\xi}{2}(t_{22}^+ + t_{22}^-)d_{2r} \tag{3.22}$$

where ξ is determined by the value of the contact area of the collision.

3.5 Implementation and Results

The deformation of the cells spreads out in a wave-propagation pattern. We can make use of this pattern [29] to reduce computation by processing the cells in an order that starts at the interacting cells and expands towards the cells farthest away. When the deformation at a distance from the interacting cells is below some threshold, we stop calculating the deformation of farther cells.

For the first shot, we implement our model for a cubic deformable object, which is decomposed into 3D cubic meshes of the same size for its initial state. Through simple collision detection, we obtain the sides that are being operated on, which we call "control side". The control side set is actually a set of active sides. Let Δt be the time step. At each time step $t = k\Delta t$ ($k = 1, 2, \cdots$), the algorithm goes through the following three steps.

1) Going through the control side, set "active" flag for those sides and obtain a set of cells that have at least one active side. We call this set of cells active cell set.

2) For each cell in the set of active cells, solve the axial deformation problem for different input situations to obtain the displacements of the passive sides and then calculate the rotation angles around the three axes of the local coordinate system. Next, set "inactive" flag for the active sides of this cell and set "active" flag for the inactive sides of this cell. We obtain a new set of active sides. Going through the new set of active sides, obtain a new set of active cells that have at least one active side and are not in the last active cell set. Repeat 2) until the active side set is empty.

3) Go to 2). When the changes of the displacements are below some threshold, update the position and dimensions for the cells.

This model is implemented on a Pentium IV 2 GHz CPU workstation. For a $10\times10\times10$ cubic structure with 1000 meshes of cube, the update rate is about 100 Hz. To meet the 1000 Hz update rate requirement of the Phantom interaction device, we

have to interpolate force feedback values between the calculated values. Future hardware advancements will help with the speed, as would more optimal programming techniques. Fig. 3.4 shows the deformation of the cube when we use an instrument to push and drag the top surface of the cube. The simulation shows that the deformation is pretty localized. This is a good feature for the simulation of local deformation.

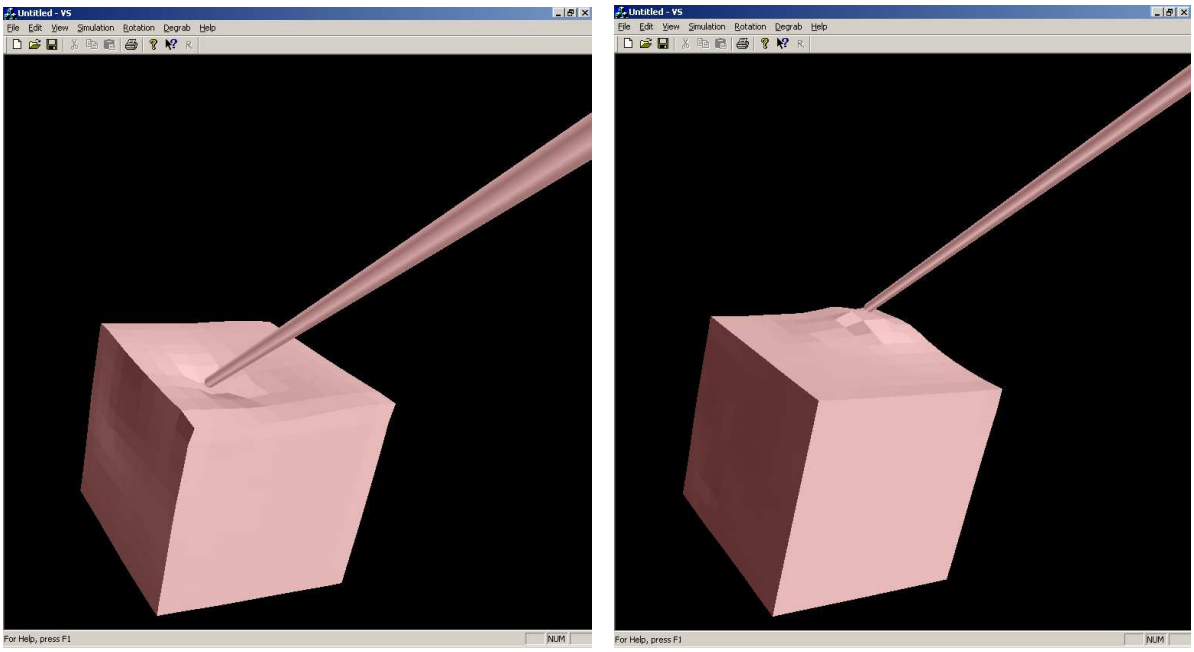

(a) (b)

Figure 3.4. Deformation of the cube when it is (a) pushed and (b) dragged from top.

3.6 Conclusion

The advantage of this model is that the deformation is localized and the displacements in different directions are deeply coupled, which is consistent with the observation for real organs. Also the fluid in the human organ is modeled in this method, which makes it possible for us to obtain the correct stress coupling effect. We know the other

models don't have a mechanism to ensure volume preservation and model stress coupling effect except the long element method.

One shortcoming of this quasi-static model is the stability problem. During simulation, we can see part of the surface of the cube jerk, especially when there is large deformation. More research needs to be done to eliminate this phenomenon.

In this model, we discretize the organ into small cubes. For meshes of this shape, it is easy for us to define the rules for the deformation of an individual mesh and the interaction between meshes. But it is not convenient for graphics display since we have to form the corresponding triangle surface mesh according to the outer cubic mesh. Further work needs to be done on the tetrahedron mesh situation.

CHAPTER 4
IDEAL SPRING CHARACTERISTICS FOR 1D AND 2D STRUCTURED MSD MODELS

4.1 Introduction

The MSD model has been widely used to model deformable objects. Generally, there are two kinds of application: graphics animation and real-time interaction with the virtual environment involving both graphics and haptics. In animation, only the graphics effect is important, and computation does not need to be real time. In the latter situation, both graphics and haptics are essential and have to be rendered in real-time. Virtual surgery simulation and computer games with force feedback are typical applications of this type.

In spite of the many reported applications of the MSD model, there is little mention in the literature about how to assign values to the parameters of the springs [64–67]. It is well known that due to spatial discretization, the MSD model can only be an approximation in some aspects to the continuum object. In case of cloth simulation for example, Gelder compared the MSD model and the finite element method and concluded that an exact simulation using the MSD model is impossible [65]. This may explain why there is little research done to optimize parameters of the MSD model.

Although the MSD model cannot give an exact simulation, some good parameter sets do give better simulation results than others. The criterion for better simulation appears ambiguous and hard to define. Current implementation of the MSD model for a lot of applications usually chooses the parameter values on a trial and error basis. That is a very tedious and time-consuming procedure. Without guidance, we cannot expect

to obtain a good parameter set for the MSD model to fully exploit its potential. So it is essential to develop some algorithms to optimize parameters for the MSD model.

One natural approach is to estimate the parameter set from outer appearances of the MSD model. For cloth animation, Jojic and Huang proposed to estimate cloth-draping parameters from range data [64]. They compared the drape of the model with the range data and searched for the best fit. Bhat et al proposed to estimate the parameters from video [66] based on matching between folds. Their method works fine for soft cloth if the experiment is done carefully. But for linen cloth, which is more rigid, the estimated parameter values turn out to be sensitive to the size of the cloth, which is an undesired property. This phenomenon does not necessarily mean that anything is wrong with their optimization method. In section 4.2.2, we will show that the problem lies in the model itself and we can extend their method to include the rest lengths of the springs as optimization variables to solve that problem.

Besides the effort above to obtain parameter values based on simulated images, there are also some methods presented to calculate parameters for the MSD model based on the material properties of the real object. Gelder derived an approximate formula to calculate the spring constants based on the constant strain assumption in the triangular/tetrahedral mesh [65]. The accuracy depends on how far the strain field is from uniform distribution for each mesh. Maciel et al [67] calculated the spring constants based on the Hooke's law. The drawback with this method is that the MSD system obtained can pass the tensile force test in a certain direction, but cannot pass it in other directions and cannot pass other tests, like the shear test.

Most research on the MSD model up to now focuses on the application of the 2D model to cloth simulation. In this chapter, we also restrict to investigate the parameter optimization problem for 1D and 2D structured MSD models. Before continuing to address this problem, let us review some related work that aimed to improve cloth

simulation. To overcome the super-elasticity phenomenon, Provot proposed to apply an ad hoc dynamic procedure to the "super-elongated" springs so as to reduce their elongation [55]. When deformation rate is greater than a critical deformation rate, the dynamic inverse procedure is applied to the two ends of the spring so that its deformation is exactly equal to the critical rate. Vassilev et al developed further Provot's method by applying a velocity directional modification approach to eliminate the super-elasticity phenomenon [48].

To model the folds and wrinkles in clothing simulation, Bridson et al proposed to calculate the bending resistance according to the bending mode motion instead of using bending springs. This method can be used to model pre-wrinkles when the rest angle is not zero [68]. To model curved undeformed configurations such as hats, leaves and aluminum cans, Grinspun et al proposed to model the bending energy as the function of the difference of the dihedral angle between adjacent triangle meshes before and after deformation [69]. These two methods for bending resistance modeling are very close. The resistant force calculation is complicated and the computation burden is much heavier than the pure MSD model.

In this chapter, we limit our work to the pure MSD model for high speed. While admitting the fact that perfect parameter assignation does not exist, we will optimize parameters for some important behaviors so that the model will behave accurately in those situations. In other words, we use these behaviors as criteria for realism. For the MSD model of rigid cloth, besides the super-elasticity phenomenon, another main defect observed is its weak resistance to lateral displacement. Although we can increase the resistance by increasing the spring constants, the relationship between the resistance and the lateral displacement is not correct. To overcome this problem, we choose to optimize the static parameters based on the bending behavior of a plate [70], since out-of-plane motion always involves dynamic local bending. From another point of view, local

bending behavior is important in itself because wrinkles and folds are very important in cloth simulation. In section 4.2.2, we find that as long as we want to get approximate results in some sense, it is essential to use nonzero pre-displacement (or preload) for the springs, which is against the common assumption and therefore is one of the main contributions of this dissertation.

4.2 The 1D Structured MSD Model

4.2.1 Ideal Spring Characteristics for a Pure Bending Beam

We know that for a symmetric beam under the action of pure bending (see Fig. 4.1), the curvature is the same everywhere on the neutral plane of the beam. The relationship between the radius R of the curvature ρ and applied bending moment M is stated by

$$R = \frac{1}{\rho} = \frac{EI}{M} \tag{4.1}$$

where E is the modulus of elasticity of the beam material and I is the moment of inertia of the beam about its neutral plane.

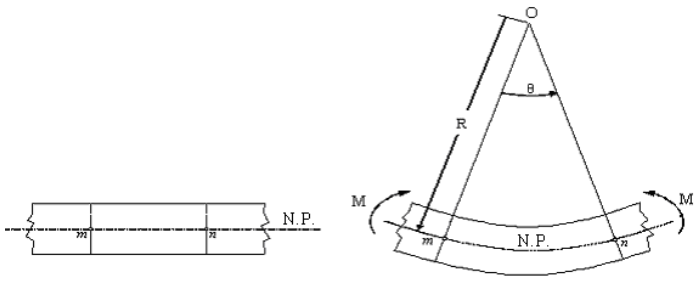

Figure 4.1. A pure bending beam.

The bending energy absorbed in an interval of length U in the beam is

$$E_b = \frac{1}{2} M \rho U = \frac{1}{2} EIU\rho^2 \tag{4.2}$$

where the subscript b indicates the beam.

For a MSD system modeling the beam, we consider the simplest situation when the beam is modeled by uniformly distributed masses connected by springs between neighbor masses and every other masses (Fig. 4.2). We refer to the first type of spring which connects adjacent masses as the *structural* spring and the second type which connects every other mass as the *flexion* spring. Assume the energy functions of the structural spring and the flexion spring to be $W_1(u)$ and $W_2(v)$ respectively, where u and v are the elongations of two types of springs.

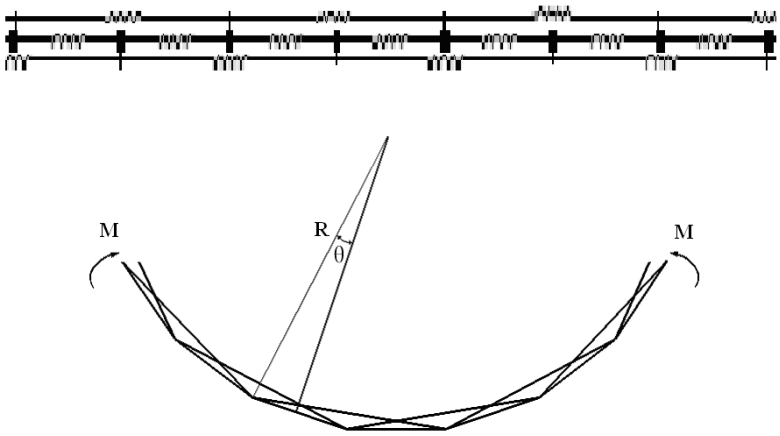

Figure 4.2. Top: a beam modeled by the MSD system; bottom: the state of the springs after bending the MSD model of the beam.

When the MSD system above is under pure bending action, it will deform in a similar way as a beam (Fig. 4.2). For a realistic MSD model for a beam, it should bend approximately in the same way as the beam does under pure bending action.

On one hand, the MSD system should have the same stiffness against bending, i. e. it should absorb the same amount of energy for the same shape of bending as the real beam. We have

$$W_1(u) + W_2(v) - W_1(u_0) - W_2(v_0) = E_b \tag{4.3}$$

where u_0 and v_0 are the elongations of the structural spring and flexion spring respectively when the model is in its natural rest state. Here we don't restrict u_0 and v_0 to be zero to give more freedom to parameter optimization. Nonzero u_0 and v_0 values for the springs on the edge pose a problem for the balance of the boundary masses. But for the springs not on the boundary, it is possible to make them have nonzero u_0 or v_0. In this sense, we optimize the parameters for the inner springs in this section.

Let the rest lengths of the structural spring and the flexion spring be L_1 and L_2 respectively. In Fig. 4.2, we can get

$$u = 2R\sin\theta - L_1 \tag{4.4}$$

$$v = 2R\sin 2\theta - L_2 \tag{4.5}$$

Let the length of the structural spring and the flexion spring be U and $2U$ respectively when the model is in its natural rest state. We have

$$U = 2R\theta \tag{4.6}$$

Then

$$u = \frac{2}{\rho}\sin\frac{U\rho}{2} - L_1 \tag{4.7}$$

$$v = \frac{2}{\rho}\sin U\rho - L_2 \tag{4.8}$$

$$\frac{du}{d\rho} = \frac{U}{\rho}\cos\frac{U\rho}{2} - \frac{2}{\rho^2}\sin\frac{U\rho}{2} \tag{4.9}$$

$$\frac{dv}{d\rho} = \frac{2U}{\rho}\cos U\rho - \frac{2}{\rho^2}\sin U\rho \tag{4.10}$$

On the other hand, for the same shape of bending, the masses of the MSD model that are not close to the two ends should reach an equilibrium state without external force, i.e. the resultant force imposed by springs on those masses should be zero. We have

$$W_1'\sin\theta = -W_2'\sin 2\theta \tag{4.11}$$

So

$$W_1'(u) = -2W_2'(v)\cos\theta = -2W_2'(v)\cos\frac{U\rho}{2} \tag{4.12}$$

From (4.2), (4.3), (4.9) and (4.10), we have

$$W_1'(u)\left(\frac{U}{\rho}\cos\frac{U\rho}{2} - \frac{2}{\rho^2}\sin\frac{U\rho}{2}\right) + W_2'(v)\left(\frac{2U}{\rho}\cos U\rho - \frac{2}{\rho^2}\sin U\rho\right) = EIU\rho \tag{4.13}$$

From (4.12) and (4.13), we have

$$-2W_2'(v)\cos\frac{U\rho}{2}\left(\frac{U}{\rho}\cos\frac{U\rho}{2} - \frac{2}{\rho^2}\sin\frac{U\rho}{2}\right) + W_2'(v)\left(\frac{2U}{\rho}\cos U\rho - \frac{2}{\rho^2}\sin U\rho\right) = EIU\rho \tag{4.14}$$

Then we can obtain

$$W_2'(v) = \frac{EI\rho^2}{\cos U\rho - 1} \tag{4.15}$$

$$W_1'(u) = \frac{2EI\rho^2}{1-\cos U\rho}\cos\frac{U\rho}{2} \tag{4.16}$$

We cannot obtain a closed and explicit form for $W_1'(u)$ vs. u and $W_2'(v)$ vs. v. However, we can obtain the numerical relationships of them in Fig. 4.3 and Fig. 4.4.

4.2.2 Linear Spring Approximation

If we use linear springs to approximate the structural spring and the flexion spring, we can assume that the reaction force functions for the two types of spring are $F_1(x) = a_1x$ and $F_2(x) = b_1x$ respectively. To ensure the equilibrium condition at the operation point, which corresponds to the natural rest state of the model, $F_1(x) = a_1x$ must pass through $(u_0, W_1'(u_0))$. According to (4.7) and (4.16), we have

$$\begin{aligned} a_1 &= \lim_{\rho\to 0}\frac{W_1'(u)}{u} \\ &= \lim_{\rho\to 0}\frac{2EI\rho^2 cos\frac{U\rho}{2}}{(1-\cos U\rho)(\frac{2}{\rho}\sin\frac{U\rho}{2} - L_1)} \\ &= \frac{4EI}{U^2(U-L_1)} \quad (0 \le L_1 < U) \end{aligned} \tag{4.17}$$

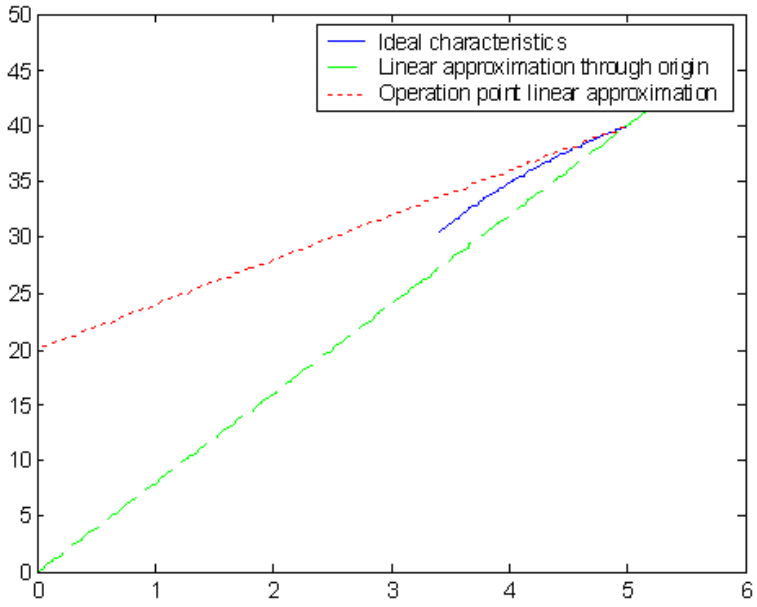

Figure 4.3. Ideal characteristics for the structural spring (solid), its linear operation point approximation (dotted) and linear approximation through origin (dashed).

Similarly, we can have

$$b_1 = \frac{2EI}{U^2(L_2 - 2U)} \qquad (L_2 > 2U) \tag{4.18}$$

Now there are still two unknowns L_1 and L_2. We can use these two parameters to achieve better approximations of the characteristics of the two types of spring. From (4.7) and (4.16), we know that function $W_1'(u)$ will not change its shape but shift horizontally when L_1 changes. In Fig. 4.3, it is clear that for some particular value of L_1, $F_1(u) = a_1 u$ will be closest to $W_1'(u)$. We choose the approximation criterion to be

$$\begin{aligned} G_1(L_1) &= \int_{u(\rho_0)}^{u_0} (W_1'(u(\rho)) - a_1(L_1)u(\rho))^2 du \\ &= \int_{\rho_0}^{0} \left(\frac{2EI\rho^2}{1-\cos U\rho} \cos\frac{U\rho}{2} - \frac{4EI}{U^2(U-L_1)} \left(\frac{2}{\rho}\sin\frac{U\rho}{2} - L_1\right) \right)^2 \left(\frac{U}{\rho}\cos\frac{U\rho}{2} - \frac{2}{\rho^2}\sin\frac{U\rho}{2}\right) d\rho \end{aligned} \tag{4.19}$$

Then we minimize $G_1(L_1)$ to obtain the optimal value of L_1. Here we choose $\rho_0 = \frac{\sqrt{2}}{U}$, which means 90 degrees bending for adjacent structural springs, to obtain the numerical

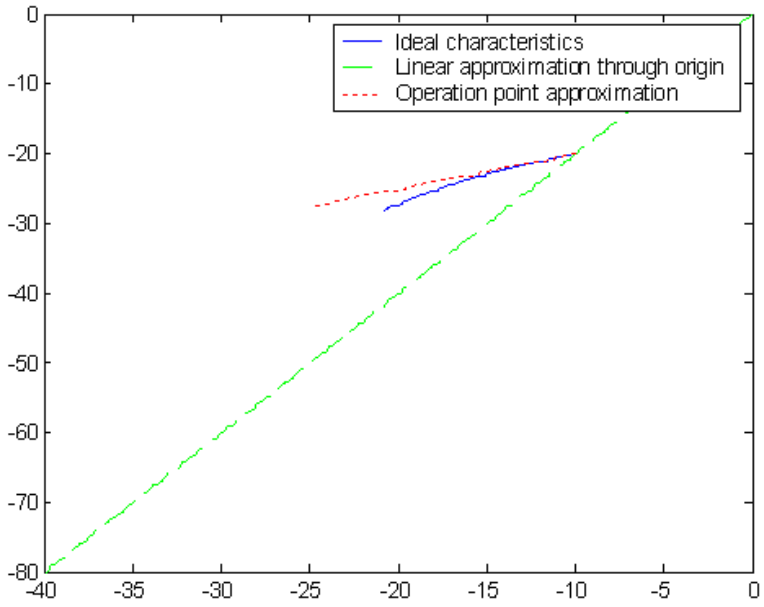

Figure 4.4. Ideal characteristics for the flexion spring (solid), its linear operation point approximation (dotted) and linear approximation through origin (dashed).

relationship between $G_1(L_1)$ and L_1 as shown in Fig. 4.5(a). We can see that $G_1(L_1)$ increases monotonically as L_1 increases from 0 to U. Based on this, we should choose L_1 close to zero.

To optimize L_2 to obtain an optimal approximation between $F_2(v) = b_1 v$ and $W_2'(v)$, we choose the criterion to be

$$\begin{aligned} G_2(L_2) &= \int_{v(\rho_0)}^{v_0} (W_2'(v(\rho)) - b_1(L_2)v(\rho))^2 dv \\ &= \int_{\rho_0}^{0} \left(\frac{EI\rho^2}{\cos U\rho - 1} - \frac{2EI}{U^2(L_2 - 2U)} (\frac{2}{\rho} \sin U\rho - L_2) \right)^2 (\frac{2U}{\rho} \cos U\rho - \frac{2}{\rho^2} \sin U\rho) d\rho \end{aligned} \quad (4.20)$$

We also choose $\rho_0 = \frac{\sqrt{2}}{U}$ to obtain the numerical relationship between $G_2(L_2)$ and L_2 as shown in Fig. 4.5(b). We can see that $G_2(L_2)$ decreases monotonically as L_2 increases from $2U$ to $6U$, and increases monotonically as L_2 increases from $6U$ to infinity. In this point of view, we should choose L_2 around $6U$.

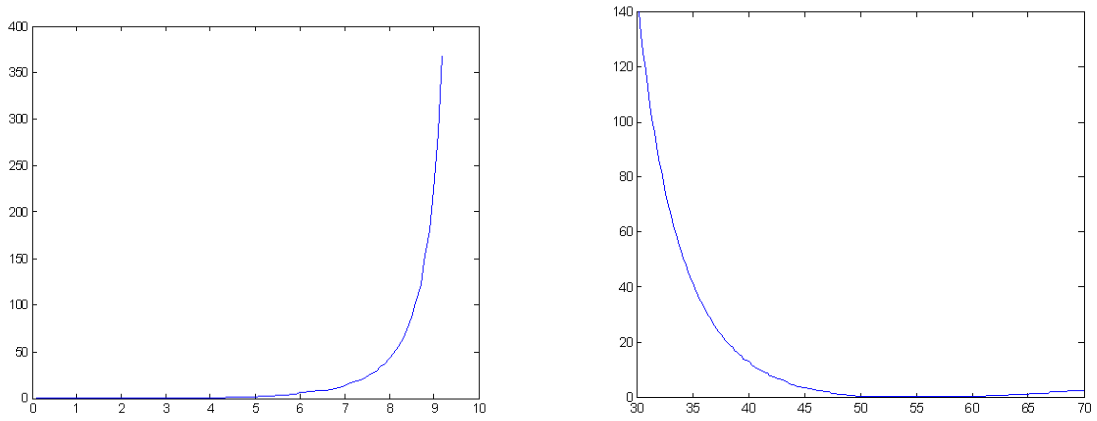

(a) (b)

Figure 4.5. Relationship between the linear approximation error and the rest length of (a) the structural spring and (b) the flexion spring.

From the discussion above we can see clearly how important it is that the two types of spring are not at rest for the natural rest state of the beam.

4.2.3 Linear Spring Operation Point Approximation

Since the springs work around their operation points which correspond to the natural rest state of the model, we can use the operation point approximation to achieve better approximation than above. Let

$$F_1(u) = F_1(u_0) + a_1'(u - u_0) \tag{4.21}$$

$$F_2(v) = F_2(v_0) + b_1'(v - v_0) \tag{4.22}$$

We have

$$u_0 = U - L_1 \tag{4.23}$$

$$v_0 = 2U - L_2 \tag{4.24}$$

According to (4.15), we have

$$F_1(u_0) = \lim_{\rho\to 0} W_1'(u(\rho)) = \lim_{\rho\to 0} \frac{2EI\rho^2}{1-\cos U\rho}\cos U\rho = \frac{4EI}{U^2} \tag{4.25}$$

Similarly, we can get

$$F_2(v_0) = \lim_{\rho\to 0} W_2'(v(\rho)) = -\frac{2EI}{U^2} \tag{4.26}$$

According to (4.16) and (4.9), we have

$$W_1''(u)=\frac{EI\rho^3\left(4\cos\frac{U\rho}{2}-U\rho\sin\frac{U\rho}{2}-4\cos U\rho\cos\frac{U\rho}{2}+U\rho\cos U\rho\sin\frac{U\rho}{2}-2U\rho\sin U\rho\cos\frac{U\rho}{2}\right)}{(1-\cos U\rho)^2(U\rho\cos\frac{U\rho}{2}-2\sin\frac{U\rho}{2})} \tag{4.27}$$

Then

$$a_1' = \lim_{\rho\to 0} W_1''(u(\rho)) = \frac{4EI}{U^3} \tag{4.28}$$

According to (4.15) and (4.10), we have

$$W_2''(v) = \frac{EI\rho(U\rho\sin U\rho + 2\cos U\rho - 2)}{(\cos U\rho - 1)^2(\frac{2U}{\rho}\cos U\rho - \frac{2}{\rho^2}\sin U\rho)} \tag{4.29}$$

Then

$$b_1' = \lim_{\rho\to 0} W_2''(v(\rho)) = \frac{EI}{2U^3} \tag{4.30}$$

We can see that $F_1(u) = F_1(u_0) + a_1'(u-u_0)$ and $W_1'(u)$ are both independent of L_1, so there is no way to use L_1 to optimize the approximation between them. Similar argument is also true for the approximation between $F_2(v) = F_2(v_0) + b_1'(v-v_0)$ and $W_2'(v)$.

From another point of view, there is no reason for not letting the force-displacement relationship pass though the origin. According to equation (4.25), (4.26), (4.28) and (4.30), we can obtain $L_1 = 0$ and $L_2 = 6U$. In this case, the operation point linear approximation is the best linear approximation through origin.

We calculate the numerical results so that we can compare the extent of approximation by using the same criterion that is used in subsection 4.2.2. We obtained $G_1(L_1) \approx 0.08$ and $G_2(L_2) \approx 0.58$. The two values are both very small compared to

the magnitudes of the reaction forces of the two types of spring, which means high accuracy of the approximation.

4.3 The 2D Structured MSD Model

4.3.1 Model Structure

In cloth simulation, a rectangular mesh is often used (Fig. 4.6 left). In this model structure, there are three types of springs: structural springs, shear springs and flexion springs [55]. The structural springs are used to model the interaction between adjacent parts of the cloth. The flexion springs are used to model the resistance of the cloth against bending. The shearing springs are used to model the shearing resistance. These three types of springs of the 2D MSD model are necessary to achieve basic realism for the cloth simulation. In this structure, a common mass has 12 springs connected to it. The rectangular structure is easy to implement, but one defect with the rectangular mesh is that it has a small resistance against bending, especially the diagonal bending. We can add diagonal flexion spring to solve this problem. Then we notice that we only need one shearing spring in one of the two diagonal directions to reduce the number of springs for each mass. After eliminating the shear springs in one diagonal direction, we can obtain a rectangular triangle mesh. In view of the symmetry, we instead use an equilateral triangle mesh (Fig. 4.6 right). In this model structure, since the triangular mesh itself can resist shearing action, there are only two types of springs: structural springs and flexion springs. For each mass, there are also 12 springs connected to it. So this structure has the same computation as the rectangular structure. And it has advantage over rectangular mesh since it has more even resistance against bending, shearing and stretching.

In this chapter we only optimize the static parameters of the MSD model while leaving the dynamic parameters (damping coefficients) out. Generally for the masses

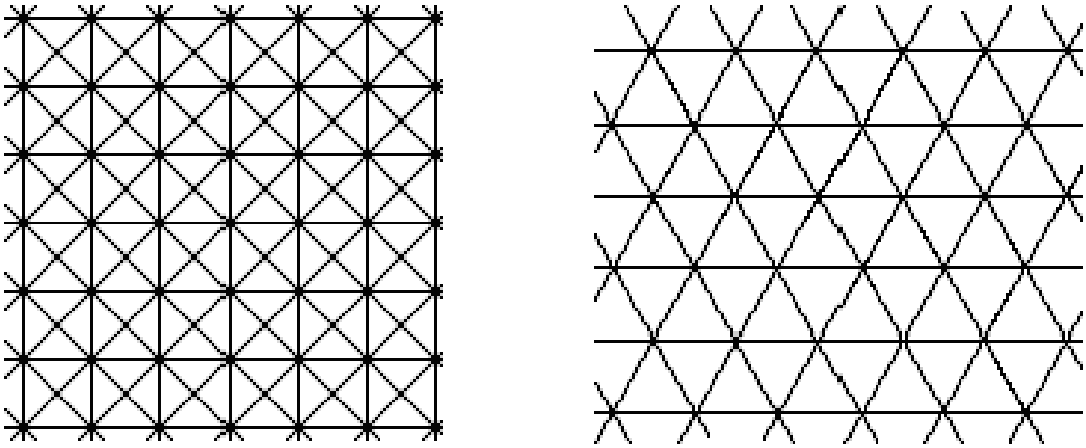

Figure 4.6. Structured meshes: (left) the rectangular meshes; (right) the equilateral triangle meshes.

of the MSD model, we assign their values proportional to their influence area, which is one third of the area of all the incident triangles or one fourth of the area of all the incident rectangles. Here we assign the same values for all the masses since the masses are evenly distributed. Generally, the MSD model has different resistance against bending in different directions. In this chapter we optimize parameters based on axisymmetric actions to make the average resistance against bending along different directions correct.

According to the elasticity theory of plate, when an isotropic circular plate is bent by a moment uniformly distributed along the edge, it will change its shape into a parabolic surface (Fig. 4.7). Assume the thickness and radius of the plate is h and a respectively ($h \ll a$). For a rotation angle of α on the edge of the plate, the displacement of the middle plane of the circular plate [71, 72] in the polar coordinate system in the direction of the z-axis is

$$w(r) = \frac{\alpha a}{2}\left[1 - (\frac{r}{a})^2\right]. \tag{4.31}$$

The moment applied per unit length is

$$M_r(\alpha) = \frac{(1+\nu)D\alpha}{a}, \tag{4.32}$$

where ν is the Poisson constant and $D = Eh^3/(12(1-\nu^2))$ is the flexural stiffness of the elastic plate.

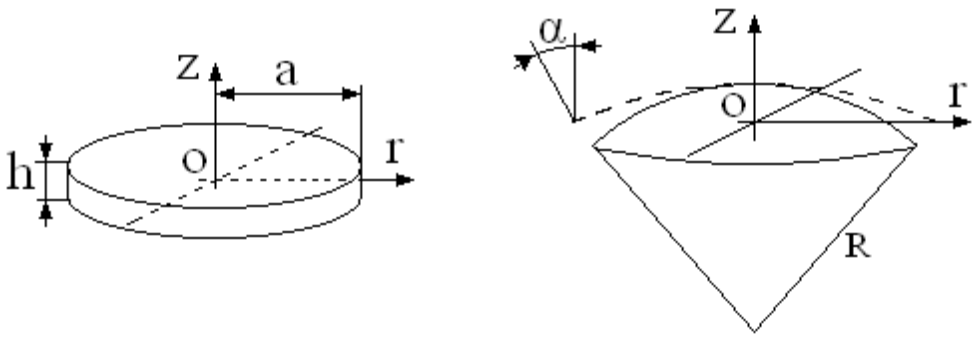

Figure 4.7. Left: the original flat circular plate; right: the circular plate under pure bending—parabolic middle surface (dashed line) and its spherical cap approximation (solid line).

So the strain energy of the plate when it is bent up to an angle of α at the edge is

$$E_p^b(\rho) = \int_0^\alpha 2\pi a M_r(\phi) d\phi = \pi(1+\nu) D a^2 \rho^2, \tag{4.33}$$

where the subscript p is used to indicate the plate and $\rho = \alpha/a$.

From (4.31), we can obtain the curvature of the generating curve of the revolutionary parabolic surface.

$$\kappa(r) = \frac{|d^2w/dr^2|}{(\sqrt{1+(dw/dr)^2})^3} = \frac{\rho}{\left(\sqrt{1+\frac{\alpha^2 r^2}{a^2}}\right)^3} \tag{4.34}$$

When $\alpha \ll 1$, we have $\kappa \approx \rho = \alpha/a$. In this situation, the curvature is approximately the same everywhere, and hence the parabolic surface can be approximated by a spherical cap with a radius of $R = 1/\rho$ (Fig. 4.7).

For the corresponding MSD model with equilateral triangle meshes, the energy stored in the same circular area should satisfy

$$N_1 W_1(u) + N_2 W_2(v) - N_1 W_1(u_0) - N_2 W_2(v_0) = \pi(1+\nu) D a^2 \rho^2 \tag{4.35}$$

where u and v are the displacements of the structural spring and the flexion spring respectively when the MSD system is bent into a spherical cap; u_0 and v_0 are the pre-displacements when the MSD system is in its natural rest state; N_1 and N_2 are the numbers of the two types of spring respectively.

In (4.35), N_1 and N_2 are the numbers of structural springs and flexion springs respectively. We know the area of the equilateral triangle mesh is $\frac{\sqrt{3}a^2}{4}$. Since each triangle has three vertices, and each vertex is shared between six triangles, each vertex corresponds to an area of $\frac{\sqrt{3}a^2}{2}$. For an circular area of radius a, when a is very large, the number of vertices it contains is approximately

$$N_v \approx \frac{\pi a^2}{\frac{\sqrt{3}U^2}{2}} = \frac{2\sqrt{3}\pi a^2}{3U^2} \tag{4.36}$$

Since each vertex connects to six structural (flexion) springs, and each structural (flexion) spring connects two vertices, the numbers of the two types of springs are

$$N_i \approx 3N_v \approx \frac{2\sqrt{3}\pi a^2}{U^2} \qquad (i = 1, 2) \tag{4.37}$$

From (4.35) and (4.37), when $a \gg U$, we have

$$W_1(u) + W_2(v) - W_1(u_0) - W_2(v_0) = \frac{\sqrt{3}(1+\nu)DU^2\rho^2}{6} \tag{4.38}$$

Next we derive the relationship between the elongations of the springs and the curvature of the surface. Let the rest length of the structural spring and the flexion spring be L_1 and L_2 respectively. Similar to what we have done in subsection 4.2.1, we can get

$$\theta = \frac{U\rho}{2} \tag{4.39}$$

$$u = \frac{2}{\rho}\sin\frac{U\rho}{2} - L_1 \tag{4.40}$$

$$v = \frac{2}{\rho}\sin U\rho - L_2 \tag{4.41}$$

$$\frac{du}{d\rho} = \frac{U}{\rho}\cos\frac{U\rho}{2} - \frac{2}{\rho^2}\sin\frac{U\rho}{2} \tag{4.42}$$

$$\frac{dv}{d\rho} = \frac{2U}{\rho}\cos U\rho - \frac{2}{\rho^2}\sin U\rho \tag{4.43}$$

In another aspect, for the same shape of bending, the masses of the MSD model that are not close to the edge should reach an equilibrium state without external force, i.e. the resultant force imposed by the springs on masses should be zero. We have

$$W_1'(u)\sin\theta = -W_2'(v)\sin 2\theta \tag{4.44}$$

So

$$W_1'(u) = -2W_2'(v)\cos\theta = -2W_2'(v)\cos\frac{U\rho}{2} \tag{4.45}$$

According to (4.38), (4.42), (4.43) and (4.45), we can obtain

$$W_2'(v) = \frac{\sqrt{3}(1+\nu)DU\rho^2}{3(\cos U\rho - 1)} \tag{4.46}$$

$$W_1'(u) = \frac{2\sqrt{3}(1+\nu)DU\rho^2}{3(1-\cos U\rho)}\cos\frac{U\rho}{2} \tag{4.47}$$

Similar to the 1D, we can obtain the numerical relationship of $W_1'(u)$ vs. u and $W_2'(v)$ vs. v as shown in Fig. 4.8(a) and Fig. 4.8(b).

We know

$$u_0 = U - L_1 \tag{4.48}$$

$$v_0 = 2U - L_2 \tag{4.49}$$

According to (4.46) and (4.47), we get

$$W_1'(u_0) = \lim_{\rho\to 0} W_1'(u(\rho)) = \lim_{\rho\to 0}\frac{2\sqrt{3}(1+\nu)DU\rho^2}{3(1-\cos U\rho)}\cos\frac{U\rho}{2} = \frac{4\sqrt{3}(1+\nu)D}{3U} \tag{4.50}$$

$$W_2'(v_0) = \lim_{\rho\to 0} W_2'(v(\rho)) = -\frac{2\sqrt{3}(1+\nu)D}{3U} \tag{4.51}$$

Fig. 4.8(a) and 4.8(b), (4.50) and (4.51) shows that the two types of spring are far from their rest state. So it is very important that we have u_0 and v_0 as optimization

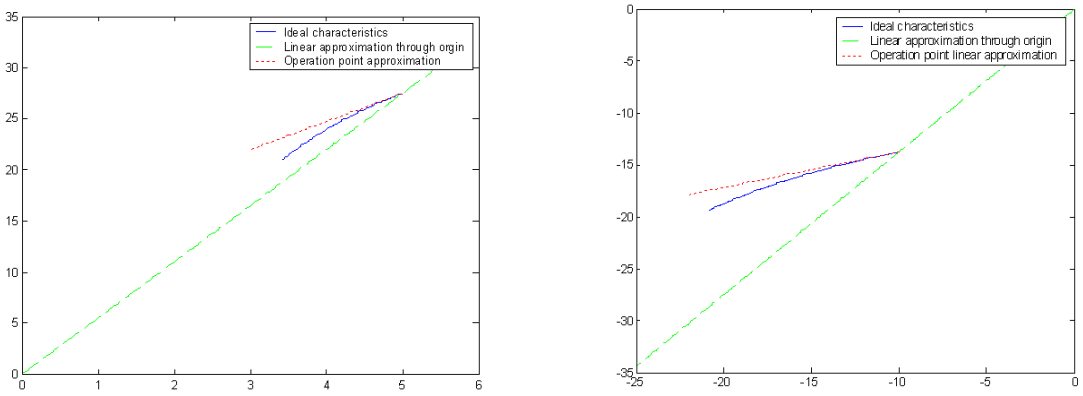

(a) (b)

Figure 4.8. (a) Ideal characteristics for the structural spring (solid line), its operation point linear approximation (dotted line) and linear approximation through origin (dashed line); (b) Ideal characteristics for the flexion spring (solid line), its operation point linear approximation (dotted line) and linear approximation through origin (dashed line) .

parameters. In the next subsection, we will show the relationship between the accuracy of the linear approximation and the values of u_0 and v_0.

4.3.2 Linear Spring Approximation

If we use linear springs to approximate structural springs and flexion springs, we can assume that the reaction force functions for the two types of spring are $F_1(x) = a_1 x$ and $F_2(x) = b_1 x$ respectively, where x is the elongation of the spring.

To ensure the equilibrium condition at the operation point that corresponds to the natural rest state of the model, $F_1(x) = a_1 x$ must pass through $(u_0, W_1'(u_0))$. According to (4.50) and (4.48), we have

$$a_1 = \frac{W_1'(u_0)}{u_0} = \frac{4\sqrt{3}(1+\nu)D}{3U(U-L_1)} \tag{4.52}$$

Similarly, we can obtain

$$b_1 = \frac{W_2'(v_0)}{v_0} = \frac{2\sqrt{3}(1+\nu)D}{3U(L_2-2U)} \tag{4.53}$$

Now there are still two unknowns L_1 and L_2 undetermined. We can optimize these two parameters to achieve a good approximation. From (4.40) and (4.47), we know that function $W_1'(u)$ will not change its shape but shift horizontally when L_1 changes. From Fig. 4.8(a), it is clear that for some particular value of L_1, $F_1(u) = a_1 u$ will be closest to $W_1'(u)$ in some sense. We take the square error as the approximation criterion.

$$G_1(L_1)=\int_{u(\rho_0)}^{u_0}(W_1'(u(\rho))-a_1(L_1)u(\rho))^2du$$
$$=\int_{\rho_0}^{0}\left(\frac{2\sqrt{3}(1+\nu)DU\rho^2}{3(1-\cos U\rho)}\cos\frac{U\rho}{2}-\frac{4\sqrt{3}(1+\nu)D}{3U(U-L_1)}(\frac{2}{\rho}\sin\frac{U\rho}{2}-L_1)\right)^2(\frac{U}{\rho}\cos\frac{U\rho}{2}-\frac{2}{\rho^2}\sin\frac{U\rho}{2})d\rho \quad (4.54)$$

Here we choose $\rho_0 = \frac{\sqrt{2}}{10U}$, which means 90 degrees bending for every the tenth structural spring, to obtain the numerical relationship between $G_1(L_1)$ and L_1 as shown in Fig. 4.9(a). We can see that $G_1(L_1)$ increases monotonically as L_1 increases from 0 to U. Based on this, we should L_1 choose around zero.

To optimize L_2 to obtain an optimal approximation between $F_2(v) = b_1 v$ and $W_2'(v)$, we also use the square error as the criterion

$$G_2(L_2)=\int_{v(\rho_0)}^{v_0}(W_2'(v(\rho))-b_1(L_2)v(\rho))^2dv$$
$$=\int_{\rho_0}^{0}\left(\frac{\sqrt{3}(1+\nu)DU\rho^2}{3(\cos U\rho-1)}-\frac{2\sqrt{3}(1+\nu)D}{3U(L_2-2U)}(\frac{2}{\rho}\sin U\rho-L_2)\right)^2(\frac{2U}{\rho}\cos U\rho-\frac{2}{\rho^2}\sin U\rho)d\rho \quad (4.55)$$

We also choose $\rho_0 = \frac{\sqrt{2}}{10U}$ to obtain the numerical relationship between $G_2(L_2)$ and L_2 as shown in Fig. 4.9(b). We can see that $G_2(L_2)$ decreases monotonically as L_2 increases from $2U$ to $6U$, and $G_2(L_2)$ increases monotonically as L_2 increases from 6U to infinity. Based on this, we should choose L_2 around $6U$.

From above we can again see clearly that it is necessary to have the two types of spring far from their rest states to obtain good bending behavior!

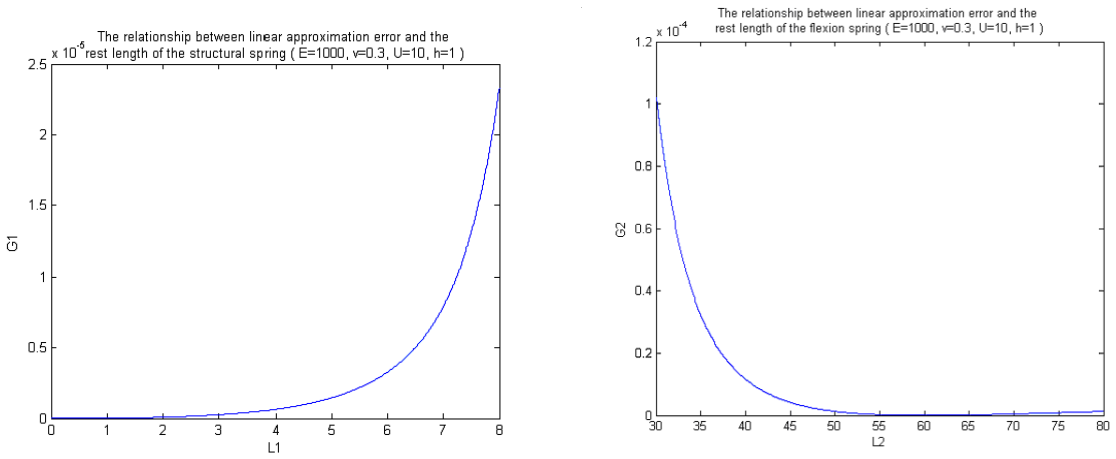

(a) (b)

Figure 4.9. The relationship between the error of the linear approximation through origin and the rest length of (a) the structural spring and (b) the flexion spring.

4.3.3 Linear Spring Operation Point Approximation

Since the springs work around their operation points that correspond to the natural rest state of the system, we can use the operation point approximation to achieve better result than general linear approximation through origin. Let

$$F_1(u) = F_1(u_0) + a_1'(u - u_0) \tag{4.56}$$

$$F_2(v) = F_2(v_0) + b_1'(v - v_0) \tag{4.57}$$

where $F_1(u_0) = W_1'(u_0)$ and $F_2(v_0) = W_2'(v_0)$.

According to equations (4.42) and (4.47), we have

$$W_1''(u) = \frac{2\sqrt{3}(1+\nu)DU\rho^3\left[(2\cos\frac{U\rho}{2} - \frac{U\rho}{2}\sin\frac{U\rho}{2})(1 - cosU\rho) - U\rho\sin U\rho\cos\frac{U\rho}{2}\right]}{3(1-\cos U\rho)^2(U\rho\cos\frac{U\rho}{2} - 2\sin\frac{U\rho}{2})} \tag{4.58}$$

Then

$$a_1' = \lim_{\rho\to 0} W_1''(u(\rho)) = \frac{4\sqrt{3}(1+\nu)D}{3U^2} \tag{4.59}$$

According to (4.43) and (4.46), we have

$$W_2''(v) = \frac{\sqrt{3}(1+\nu)DU\rho^3(U\rho\sin U\rho + 2\cos U\rho - 2)}{6(1-\cos U\rho)^2(U\rho\cos U\rho - \sin U\rho)} \tag{4.60}$$

Then

$$b_1' = \lim_{\rho \to 0} W_2''(v(\rho)) = \frac{\sqrt{3}(1+\nu)D}{6U^2} \tag{4.61}$$

The force-displacement relationship should pass though the origin. According to equation (4.50), (4.51), (4.59) and (4.61), we can obtain $L_1 = 0$ and $L_2 = 6U$. In this case, operation point linear approximation is the best linear approximation through origin.

Here we calculate the square error so that we can compare the extent of approximation between the general linear approximation and the operation point linear approximation. We obtain $G_1(L_1) \approx 4 \times 10^{-12}$ and $G_2(L_2) \approx 3 \times 10^{-11}$. The two values are both very small compared to the magnitudes of the reaction forces of the two types of spring, which means high accuracy of the approximation.

4.3.4 Boundary Effect

One problem with allowing nonzero preload in the MSD model is that the boundary masses are not in equilibrium. When the simulation starts, the finite boundary of the MSD system will contract to balance the internal force on the boundary masses, thus will change the pre-displacements. Fortunately, this contraction is only significant nearby the boundary. We experimented with structures of different sizes and found that the boundary effect decreases with the increase of the size of the structure. Fig. 4.10 shows the percentage of the change of the distance between adjacent masses at different positions for a 21×21 model structure. At positions more than 2 structural springs away from the boundary, the deviations fall below 1%. So using nonzero preload is feasible for the main part of the 2D MSD system.

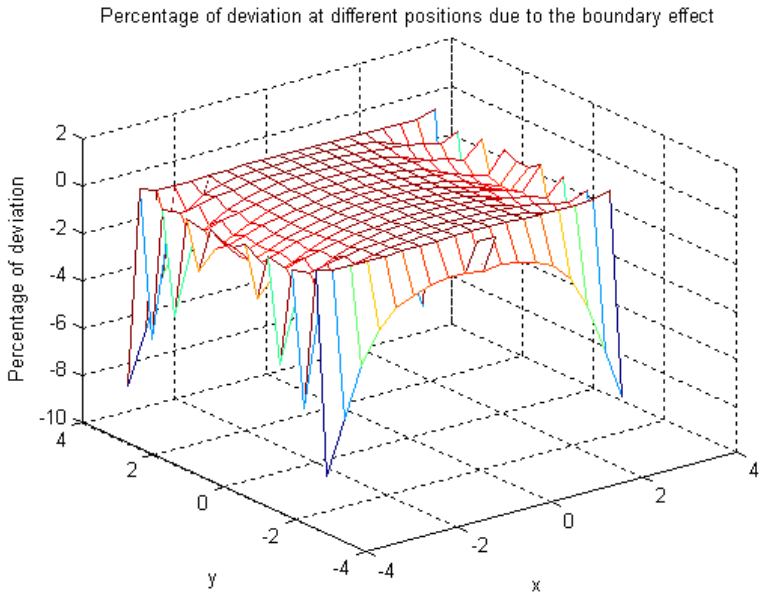

Figure 4.10. Percentage of deviation at different positions in the MSD system with equilateral triangle meshes due to the boundary effect.

4.3.5 Lateral Resistance against Displacement

Lateral resistance against displacement for a general plate of any shape and its MSD model are both very complicated. Therefore, in this subsection we only compare the lateral resistance for a circular plate and its MSD system.

According to the theory of plates [73], when a clamped circular plate of radius a is under central point load F, the central load is proportional to the displacement d when d is very small, particularly

$$F = \frac{16\pi D d}{a^2} \tag{4.62}$$

where D is the flexural stiffness of the plate.

For the 2D MSD system corresponding to the clamped circular plate above, we cannot obtain an analytical result about the lateral resistance against displacement for the general situation when $a = nU$ (n is an integer). However, we can obtain the analytical result for the simplest situation when $n = 1$. In this situation, the MSD

system has a mass corresponding to the central point of the plate and all the other masses are fixed. Assume the central mass has a small lateral displacement d. According to (4.56) and (4.57), the sum of spring energy involved with the mass is

$$\begin{aligned} W(d) &= 6(F_1(u_0) - a_1'u_0)(\sqrt{U^2+d^2} - L_1) + 3a_1'(\sqrt{U^2+d^2} - L_1)^2 + \\ &\quad 6(F_2(v_0) - b_1'v_0)(\sqrt{4U^2+d^2} - L_2) + 3b_1'(\sqrt{4U^2+d^2} - L_2)^2 \end{aligned} \tag{4.63}$$

Then the lateral resistance for such a displacement is

$$\begin{aligned} W'(d) &= 6(F_1(u_0) - a_1'U)\frac{d}{\sqrt{U^2+d^2}} + 6a_1'd + 6(F_2(v_0) - 2b_1'U)\frac{d}{\sqrt{4U^2+d^2}} + 6b_1'd \\ &= 6(F_1(u_0) + \frac{1}{2}F_2(v_0))\frac{d}{U} + (3a_1' + \frac{3}{4}b_1' - 3F_1(u_0) - \frac{3}{8}F_2(v_0))\frac{d^3}{U^3} + o(d^3) \\ &= \frac{6\sqrt{3}(1+\nu)Dd}{U^2} + O(d^3) \end{aligned} \tag{4.64}$$

According to (4.62) and (4.64), it is clear that the lateral resistance against displacement for the MSD system is smaller than its continuum counterpart when $a = U$. However, this result is still much better than that without preload, in which the lateral resistance indicated by (4.64) is a higher order infinitesimal of the displacement d.

For the general situation when $a = nU$, we did a series of experiments to obtain the numerical result about the relationship between lateral resistance and displacement at the center of the MSD system for different discretization sizes n. We modeled a plate with a radius of 10 and thickness of 0.01 and optimized the spring constants for $n = 1, 2, 4, 8, 16$ respectively and obtained the relationships between lateral resistance and displacement at the central point as shown in Fig. 4.11(a). The solid line is the relationship indicated by (4.64) for the continuum plate. We can see that for large n values, which mean high resolution of discretization, the relationship between lateral resistance and displacement is very close to that of its continuum counterpart when the displacement is small ($d < U$).

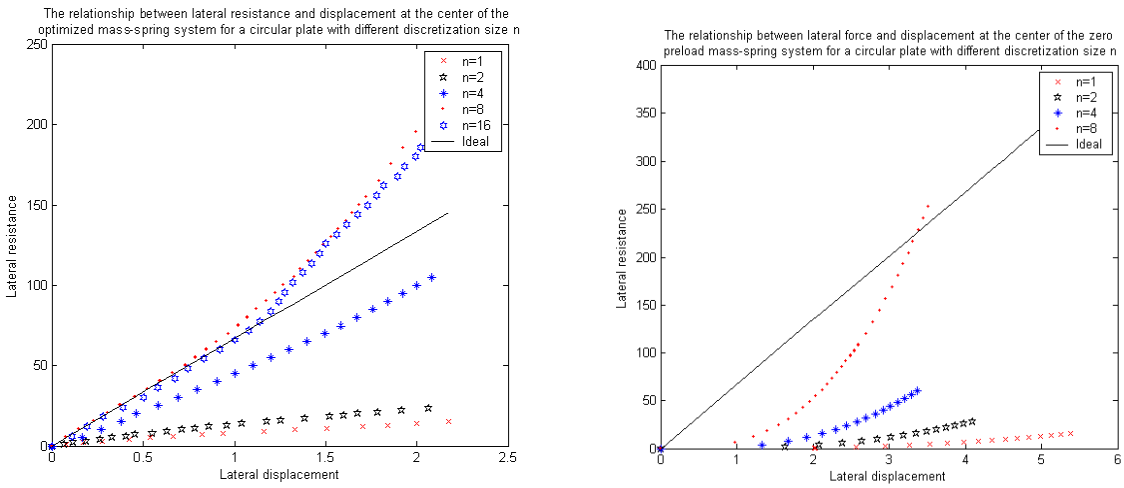

(a) (b)

Figure 4.11. (a) Lateral resistance vs. displacement of the optimized MSD system with preload for different discretization sizes; (b) lateral resistance vs. displacement of the MSD model without preload for different discretization sizes.

For comparison, we also tested the MSD system without preload and obtained the relationships between lateral resistance and displacement at the central point as shown in Fig. 4.11(b). The solid line is still the relationship indicated by (4.64) for the continuum plate. The relationships for different discretization sizes n are all nonlinear and the lateral resistance of the MSD system is much smaller than that of the continuum plate when the displacement d is small.

4.4 Simulation Result

We implemented our parameter optimization result by modifying Jeff Lander's implementation of cloth simulation [74]. First we will show that the new cloth has much more resistance against bending. In Fig. 4.12, we illustrate this point by showing the new cloth and the old cloth hung from two points along the diagonal direction under gravity for comparison. For the old cloth, the structural and the flexion spring coefficients are 4.0 and the shear spring coefficient is 2.4. For the new cloth, we use optimized parameters

with the coefficients of the structural spring and the flexion spring being 4.0 and 0.5 respectively. With the spring coefficients of close magnitude, the new cloth shows much more resistance against bending or lateral displacement. As shown in section 4.3.5, this property is mainly due to the nonzero preloads of the springs.

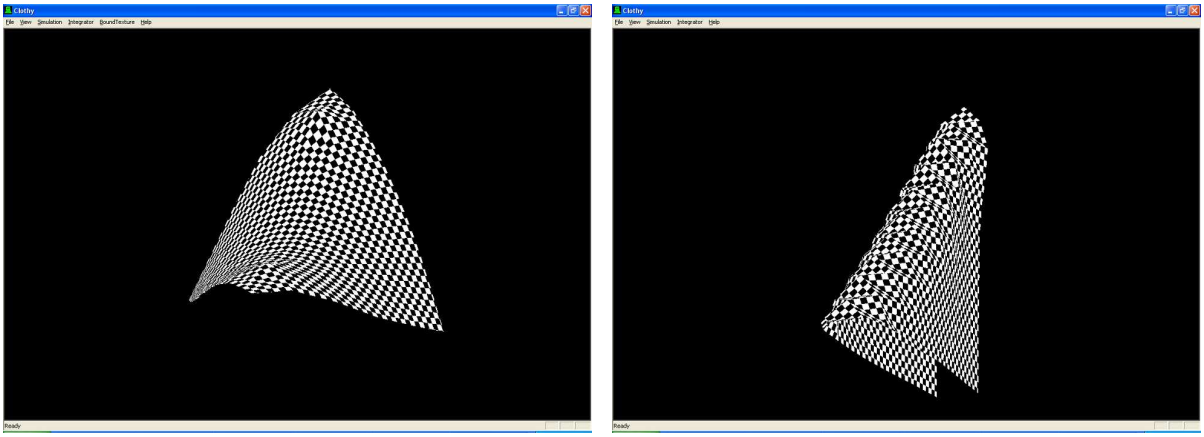

(a) (b)

Figure 4.12. (a) Cloth with preload hung from two points under gravity; (b) cloth without preload but with the same Hooke's constants hung from the same two points.

Besides the improvement on the static behavior of the cloth, the dynamic behavior of the new cloth also shows much more stiffness than the old cloth. In the sense of appearance, if the old cloth was silky, our new cloth is more like a piece of paper. To illustrate this, in Fig. 4.13 we compared the unrolling process of the new cloth and the old cloth which were rolled into cylinders beforehand. Both the pieces of cloth started to unroll at the same time. We can see that the old cloth barely unrolled when the new cloth finished unrolling, i.e. the new cloth unrolled much faster than the old cloth.

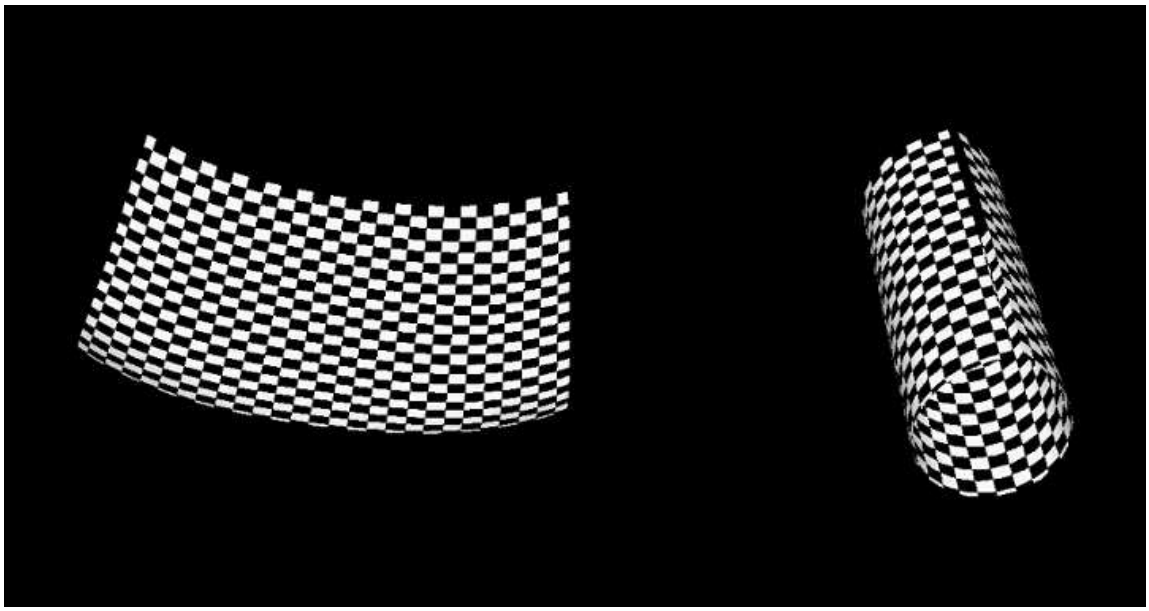

Figure 4.13. Comparison between the unrolling process of the new cloth (left) and the old cloth (right) (15×15 nodes) .

4.5 Conclusion

This chapter shows the necessity and feasibility of using nonzero preload for 1D and 2D structured MSD models, and thus provides extra degrees of freedom to improve the MSD model without increasing computation. As we have seen in section 4.4, the visual effect of the simulation is greatly improved. In fact, according to section 4.3.5, the 2D MSD model with preload can provide correct resistance against lateral displacement. Thus in an application requiring both graphics and haptics, both the two aspects will be much more realistic.

CHAPTER 5
PARAMETER OPTIMIZATION FOR THE 1D AND 2D STRUCTURED MSD MODELS

5.1 Introduction

The parameter optimization scheme proposed in chapter 4 for 1D and 2D structured MSD models has two major defects. First, the optimized MSD model usually provides too weak a resistance against stretching, although it can provide accurate bending resistance. Second, the optimization scheme is not applicable to the commonly used rectangular mesh structure because it results in negative Hooke's constants and further causes instability to the model. To overcome the first problem, in this chapter, we optimize the preloads and Hooke's constants by matching both the bending behavior and the stretching behavior of the MSD model and its continuum counterpart—a real beam or plate [75]. To overcome the second problem, instead of deriving the optimal spring characteristics and using linear approximation to obtain the preloads and Hooke's constants, we derive the optimal spring characteristics in the space of linear functions and obtain the preloads and Hooke's constants directly.

5.2 Parameter Optimization for the 1D Structured MSD Model

5.2.1 Optimizing the Spring Constants based on Pure Bending

In this section, we seek constraints on the parameters of the 1D MSD model for its best approximation to its continuum counterpart—the beam, under pure bending for the accurate modeling of the bending stiffness of the model. There are two conditions applicable to the MSD model. On the one hand, the model should have the same resistance against bending, i. e. it should consume the same amount of energy for the same

shape of bending as the real beam. On the other hand, the model should allow bending into the same shape under certain boundary condition as the real beam does under pure bending action, i.e. for that shape of bending, the masses that are not close to the two ends of the model should reach an equilibrium state without external forces. From (4.2), (4.3) and the first condition, we can obtain the energy constraint for pure bending of the model.

$$W_1(u)+W_2(v)-W_1(u_0)-W_2(v_0)=E_b^b(\rho)=\frac{1}{2}EIU\rho^2 \tag{5.1}$$

Let the rest lengths of the structural spring and the flexion spring be L_1 and L_2 respectively. The lengths of the structural spring and the flexion spring are U and $2U$ respectively when the MSD system is in its natural rest state. Thus $u_0 = U - L_1$ and $v_0 = 2U - L_2$. Let the force-displacement relationship functions of the structural spring and the flexion spring be $F_1(u)$ and $F_2(v)$ respectively, i.e.

$$F_1(u) = W_1'(u), \tag{5.2}$$

$$F_2(v) = W_2'(v). \tag{5.3}$$

Assume the springs to be linear.

$$F_1(u) = P_1 + k_1(u - u_0) \tag{5.4}$$

$$F_2(v) = P_2 + k_2(v - v_0) \tag{5.5}$$

where $P_1 = F_1(u_0)$ and $P_2 = F_2(v_0)$ are called the preloads of the two types of spring, k_1 and k_2 are the Hooke's constants.

From Fig. 4.2 bottom, we can see that the lengths of the structural spring and the flexion spring are $2R\sin\theta$ and $2R\sin 2\theta$ respectively, where θ is half the angle that the structural spring makes at the center of the curvature. So $u = 2R\sin\theta - L_1$ and $v = 2R\sin 2\theta - L_2$.

Since the neutral plane of the beam is not stretched or compressed during pure bending, the length of the arc between adjacent masses of the MSD model should always be U. Thus, we have

$$\theta = \frac{U}{2R} = \frac{U\rho}{2} \tag{5.6}$$

Then

$$u = \frac{2}{\rho}\sin\frac{U\rho}{2} - L_1 \tag{5.7}$$

$$v = \frac{2}{\rho}\sin U\rho - L_2 \tag{5.8}$$

$$\frac{du}{d\rho} = \frac{u}{\rho}\cos\frac{U\rho}{2} - \frac{2}{\rho^2}\sin\frac{U\rho}{2} = -\frac{U^3\rho}{12} + \frac{U^5\rho^3}{480} + O(\rho^5) \tag{5.9}$$

$$\frac{dv}{d\rho} = \frac{2U}{\rho}\cos U\rho - \frac{2}{\rho^2}\sin U\rho = -\frac{2U^3\rho}{3} + \frac{U^5\rho^3}{15} + O(\rho^5) \tag{5.10}$$

$$u - u_0 = \frac{2}{\rho}\sin\frac{U\rho}{2} - U = -\frac{U^3\rho^2}{24} + O(\rho^4) \tag{5.11}$$

$$v - v_0 = \frac{2}{\rho}\sin U\rho - 2U = -\frac{U^3\rho^2}{3} + O(\rho^4) \tag{5.12}$$

Taking derivative with respect to ρ on both sides of (5.1) and substituting (5.2) and (5.3) into it, we obtain

$$F_1(u)\frac{du}{d\rho} + F_2(u)\frac{dv}{d\rho} = EIU\rho \tag{5.13}$$

According to (5.4), (5.5), (5.9), (5.10), (5.11), (5.12) and (5.13), we have

$$EIU\rho = -\frac{P_1 + 8P_2}{12}U^3\rho + \left(\frac{P_1 + 32P_2}{480}U^5 + \frac{k_1 + 64k_2}{288}U^6\right)\rho^3 + O(\rho^5) \tag{5.14}$$

For the first order approximation of (5.14), we have

$$P_1 + 8P_2 = \frac{-12EI}{U^2} \tag{5.15}$$

By considering the equilibrium constraint (the second condition mentioned above) of a general mass in the radial direction (Fig. 4.2), we have

$$F_1(u)\sin\theta + F_2(v)\sin 2\theta = 0 \tag{5.16}$$

Note that since the pure bending of the beam does not consider the influence of gravity, for the corresponding MSD model, we do not consider the factor of gravity either. According to (5.4–5.6), (5.11), (5.12) and (5.16), we can obtain

$$P_1 + 2P_2 - \left(\frac{k_1 + 16k_2}{24}U^3 + \frac{P_2}{4}U^2\right)\rho^2 + O(\rho^4) = 0 \tag{5.17}$$

For the zeroth order approximation of (5.17), we have

$$P_1 + 2P_2 = 0 \tag{5.18}$$

According to (5.15) and (5.18), we have

$$P_1 = \frac{4EI}{U^2} \tag{5.19}$$

$$P_2 = -\frac{2EI}{U^2} \tag{5.20}$$

Considering the third order approximation of (5.14) and the second order approximation of (5.17), we obtain

$$k_1 = \frac{4EI}{U^3} \tag{5.21}$$

$$k_2 = \frac{EI}{2U^3} \tag{5.22}$$

The Hooke's constants specified by (5.21) and (5.22) are often too small to model the in-axis stretch or compression resistance of the beam. So it is necessary to optimize the Hooke's constants of the springs based on axial stretch or compression of the beam at the expense of the accuracy of the pure bending behavior.

Note that the two sides of (5.14) are bending resistance of the beam and the MSD model respectively. Obviously, if we do not use preloads, the linear part of the bending resistance of the model related to the bending curvature will be zero and fail to match that of the beam.

5.2.2 Optimizing the Hooke's Constants based on Stretching

In this subsection, we seek constraints on the parameters of the 1D MSD model for its best approximation to its continuum counterpart—the beam, under in-axis stretching for the accurate modeling of the in-axis stiffness of the model. For a beam of length U under axial compression or stretch with strain ε, we can obtain the strain energy by using volume integral

$$E_b^s(\varepsilon) = \int_\Omega \frac{E\varepsilon^2}{2} dV = \frac{E\varepsilon^2}{2} \cdot AU = \frac{EAU}{2}\varepsilon^2 \tag{5.23}$$

where the superscript s is used to indicate stretch or compression and A is the area of the cross section of the beam.

For the MSD model under the same strain, the energy consumed by each interval of U is

$$E_m^s(\varepsilon) \quad = \quad (P_1 + 2P_2)U\varepsilon + \frac{1}{2}(k_1 + 4k_2)U^2\varepsilon^2 \tag{5.24}$$

The MSD model and the beam should have the same tensile resistance. Thus

$$\frac{EAU}{2}\varepsilon^2 = (P_1 + 2P_2)U\varepsilon + \frac{1}{2}(k_1 + 4k_2)U^2\varepsilon^2 \tag{5.25}$$

Here we can obtain (5.18) and

$$k_1 + 4k_2 \quad = \quad \frac{EA}{U} \tag{5.26}$$

Since there are two parameters and one equation, we have one extra degree of freedom to choose the Hooke's constants, which can be utilized to minimize the boundary effect, as will be shown in subsection 5.2.4.

5.2.3 Lateral Resistance against Displacement

In this subsection, we check the accuracy of the lateral resistance against displacement that the MSD model with optimized parameters provides compared with the continuum beam, since it is a very important aspect of the physical accuracy of the model.

According to continuum mechanics [76], for a built-in beam of length L with central load F, we have

$$F = \frac{192EI}{L^3}d \tag{5.27}$$

where d is the lateral displacement.

Consider the MSD model of the beam with adjacent masses spaced by $U = L/2n$ (Fig. 4.2). Node V_{-1} and V_0 are fixed nodes. Central load F is exerted on node V_n. We can obtain (see appendix A.1 for details of the derivation)

$$\lim_{n\to\infty} \frac{F}{d_n} = \frac{192EI}{L^3} \tag{5.28}$$

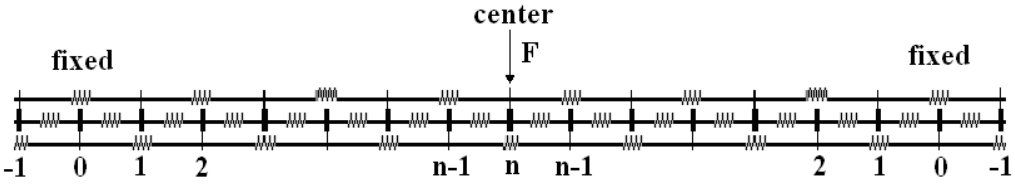

Figure 5.1. The 1D MSD model of a built-in beam under central load..

As n increases for the 1D MSD model of the beam, its central resistance force against displacement asymptotically approaches that of the continuum beam. Thus the MSD model of a beam with the optimized parameters can provide correct lateral resistance against displacement asymptotically as the discretization gets finer.

5.2.4 Boundary Effect

The side effect with allowing nonzero preloads in the MSD model is that the boundary masses are not in equilibrium. When the simulation starts, the boundary of the model will contract to balance the internal forces on the boundary masses and thus will change the pre-displacements. However, this contraction is only relatively larger near the boundary. Note that we have one extra degree of freedom to choose the Hooke's constants of

the two types of spring, which can be utilized to restrict the boundary effect to only the springs close to the boundary. Assume the ratio of the Hooke's constant of the structural spring to that of the flexion spring to be c. We modeled a beam of length 32 cm and a square cross section of depth 0.1 cm by a MSD model with 30 masses and experimented with different values of the ratio c, and found that the influence range of the boundary effect decreases with the increase of this ratio. Fig. 5.2 shows the ratio of the contraction of the structural springs (due to the boundary effect) to the desired length of the springs when the model is in its natural rest state for different values of c. When $c \geq 1$, at positions more than two structural springs away from the boundary, the ratio of contraction is negligible (see Fig. 5.2). So using nonzero preloads is feasible for the main part of the 1D MSD system.

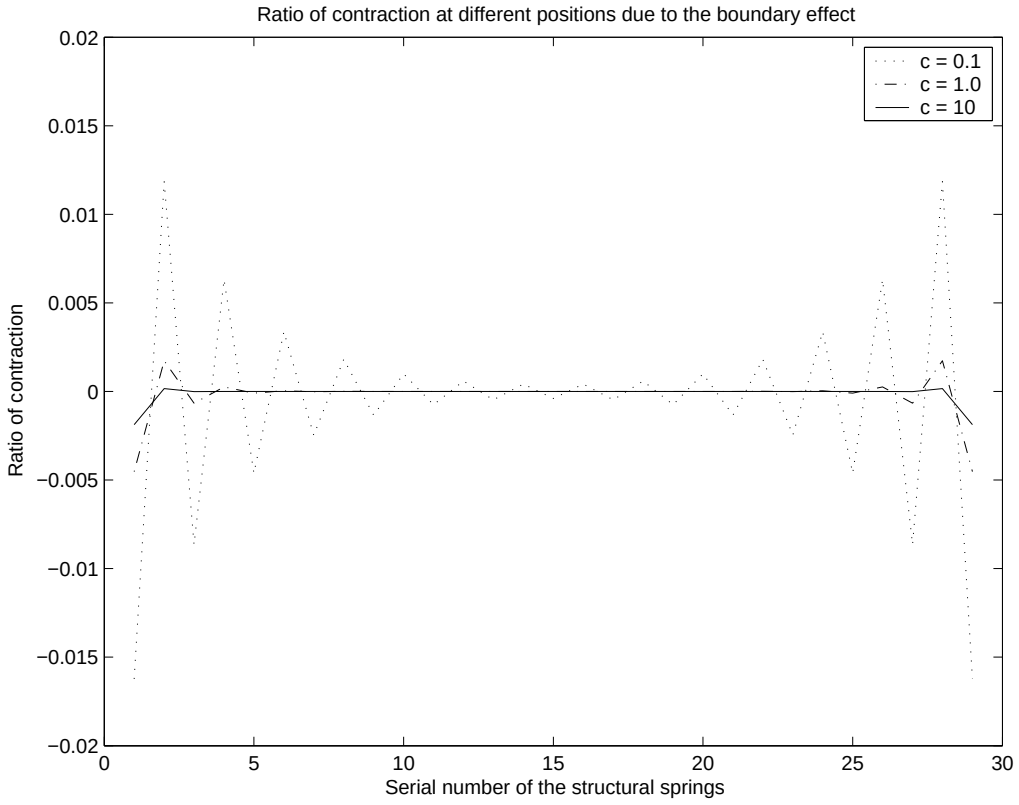

Figure 5.2. Ratio of contraction at different positions in the 1D MSD model.

Further, as shown in appendix B.1, we can restrict the boundary effect exactly to only the boundary springs by letting $k_2 = 0$ (i.e. $c = \infty$). From (5.26), we have

$$k_1 = \frac{EA}{U} \tag{5.29}$$

In this situation, according to appendix B.1, if the beam has a square cross section, the contractions of the boundary springs will be proportional to the square of the depth h and in inverse proportion to the space U between adjacent masses.

5.3 Parameter Optimization for the 2D Structured MSD Models

In this section, we investigate the 2D MSD model for two different structures, namely, rectangular meshes [55] and equilateral triangle meshes [70]. The former is the most frequently used structure and is easy to implement. The latter structure which has been used in chapter 4, is physically more accurate, as will be shown in section 5.3.4. We will optimize the static parameters of the MSD model by matching the axisymmetric bending and axisymmetric stretching of the MSD model and its continuum counterpart, minimizing the variations of both the bending resistance and stretching resistance in different directions (for isotropic materials), and restricting the boundary effect to only the boundary springs.

5.3.1 The 2D MSD Model with Rectangular Meshes

The MSD model with rectangular meshes is shown in Fig. 5.3, in which each of the $m \times n$ grids spaced by U corresponds to a lumped mass. The mass is designated by its position (i, j), in which i is the row number and j is the column number. Each mass is linked to its neighbors by massless springs. The springs linking masses (i, j) and $(i+1, j)$, and masses (i, j) and $(i, j + 1)$ are called *structural springs*. *The shearing springs* are

used to connect the diagonal neighboring masses. The springs connecting masses (i, j) and $(i + 2, j)$, and masses (i, j) and $(i, j + 2)$ are called *flexion springs*.

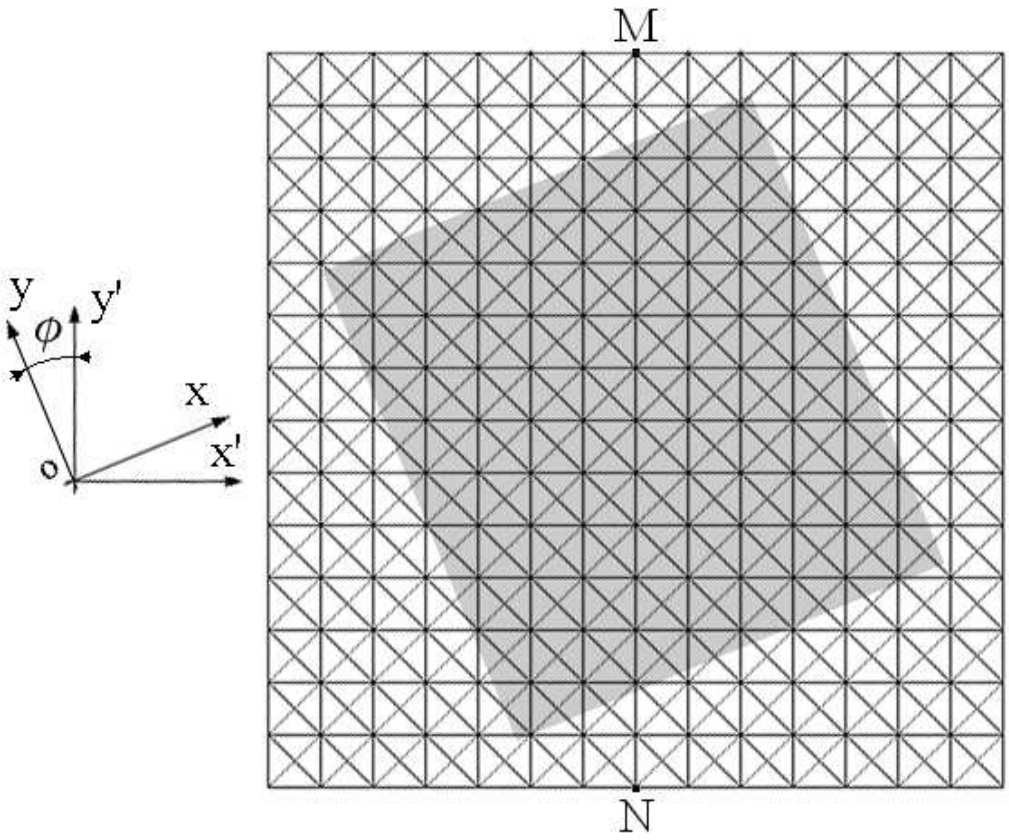

Figure 5.3. The 2D MSD model with rectangular meshes.

5.3.1.1 Optimizing the Spring Constants based on Axisymmetric Bending of a Circular Plate

Similar to the 1D situation, we aim to achieve correct bending resistance for the 2D MSD model by optimizing the parameters based on axisymmetric bending behavior. For the MSD model, the energy stored in the same circular area should satisfy

$$N_1W_1(u) + N_2W_2(v) + N_3W_3(w) - N_1W_1(u_0) \\ -N_2W_2(v_0) - N_3W_3(w_0) = E_p^b(\rho) = \pi(1+\nu)Da^2\rho^2 \tag{5.30}$$

where u, v and w are the displacements of the structural spring, the flexion spring and the shearing spring respectively when the MSD system is bent into a spherical cap; u_0, v_0 and w_0 are the pre-displacements when the model is in its natural rest state; N_1, N_2 and N_3 are the numbers of the three types of spring respectively.

According to Gauss's Circle Theorem [77], the number of masses within the circle of radius a in the lattice structure is

$$N(\frac{a}{U}) = \frac{\pi a^2}{U^2} + O(\frac{a}{U}). \tag{5.31}$$

Since every mass has four structural springs, flexion springs and shearing springs connected to it and each of these springs connects two masses, we get

$$N_i = \frac{2\pi a^2}{U^2} + O(\frac{a}{U}) \qquad (i = 1, 2, 3) \tag{5.32}$$

When $a \gg U$, from (5.30–5.32), we have

$$W_1(u) + W_2(v) + W_3(w) - W_1(u_0) - W_2(v_0) - W_3(w_0) = \frac{(1+\nu)DU^2\rho^2}{2} \tag{5.33}$$

Let the rest lengths of the three types of spring be L_1, L_2 and L_3 respectively. The lengths of the springs are U, $2U$ and $\sqrt{2}U$ respectively when the model is in its rest state. Then $u_0 = U - L_1$, $v_0 = 2U - L_2$ and $w_0 = \sqrt{2}U - L_3$. Let the force-displacement relationship functions be $F_1(u)$, $F_2(v)$ and $F_3(w)$ respectively. Then

$$F_1(u) = W_1'(u) \tag{5.34}$$

$$F_2(v) = W_2'(v) \tag{5.35}$$

$$F_3(w) = W_3'(w) \tag{5.36}$$

Note that (5.34) and (5.35) are the same as (5.2) and (5.3). We rewrite them for the convenience of reference.

Again,we assume the springs to be linear.

$$F_1(u) = P_1 + k_1(u - u_0) \tag{5.37}$$

$$F_2(v) = P_2 + k_2(v - v_0) \tag{5.38}$$

$$F_3(w) = P_3 + k_3(w - w_0) \tag{5.39}$$

where $P_1 = F_1(u_0)$, $P_2 = F_2(v_0)$ and $P_3 = F_3(w_0)$ are called the preloads of the three types of spring, k_1, k_2 and k_3 are the Hooke's constants.

Referring to Fig. 5.3, when the model is bent into the shape of a spherical cap, each spring is on the plane of certain great circle. Referring to Fig. 4.2, we define θ to be half the angle that the structural spring makes at the center of the curvature. Since the neutral plane of the plate is not stretched during the axisymmetric bending, the distance between masses of the model on the great circle should not change either. We have

$$\theta = \frac{u}{2R} = \frac{U\rho}{2} \tag{5.40}$$

We can obtain $u = 2R\sin\theta - L_1$, $v = 2R\sin 2\theta - L_2$ and $w = 2R\sin\sqrt{2}\theta - L_3$. Then

$$u - u_0 = \frac{2}{\rho}\sin\frac{U\rho}{2} - U = -\frac{U^3\rho^2}{24} + O(\rho^4) \tag{5.41}$$

$$v - v_0 = \frac{2}{\rho}\sin U\rho - 2U = -\frac{U^3\rho^2}{3} + O(\rho^4) \tag{5.42}$$

$$w - w_0 = \frac{2}{\rho}\sin\frac{\sqrt{2}U\rho}{2} - \sqrt{2}U = -\frac{\sqrt{2}U^3\rho^2}{12} + O(\rho^4) \tag{5.43}$$

$$\frac{du}{d\rho} = \frac{U}{\rho}\cos\frac{U\rho}{2} - \frac{2}{\rho^2}\sin\frac{U\rho}{2} = -\frac{U^3\rho}{12} + \frac{U^5\rho^3}{480} + O(\rho^5) \tag{5.44}$$

$$\frac{dv}{d\rho} = \frac{2U}{\rho}\cos U\rho - \frac{2}{\rho^2}\sin U\rho = -\frac{2U^3\rho}{3} + \frac{U^5\rho^3}{15} + O(\rho^5) \tag{5.45}$$

$$\frac{dw}{d\rho} = \frac{\sqrt{2}U}{\rho}\cos\frac{\sqrt{2}U\rho}{2} - \frac{2}{\rho^2}\sin\frac{\sqrt{2}U\rho}{2} = -\frac{\sqrt{2}U^3\rho}{6} + \frac{\sqrt{2}U^5\rho^3}{120} + O(\rho^5) \tag{5.46}$$

Taking derivative with respect to ρ on both sides of (5.33) and substituting (5.34–5.36) into it, we obtain

$$F_1(u)\frac{du}{d\rho} + F_2(v)\frac{dv}{d\rho} + F_3(w)\frac{dw}{d\rho} = (1+\nu)DU^2\rho \tag{5.47}$$

According to (5.37–5.39) and (5.41–5.47), we have

$$-\frac{P_1+8P_2+2\sqrt{2}P_3}{12}U^3\rho+\frac{P_1+32P_2+4\sqrt{2}P_3}{480}U^5\rho^3+ \\ \frac{k_1+64k_2+8k_3}{288}U^6\rho^3+O(\rho^5)=(1+\nu)DU^2\rho \tag{5.48}$$

For the first order approximation of (5.48), we have

$$P_1+8P_2+2\sqrt{2}P_3=\frac{-12(1+\nu)D}{U} \tag{5.49}$$

Similar to the 1D case, the equilibrium constraint is

$$F_1(u)\sin\theta+F_2(v)\sin 2\theta+F_3(w)\sin\sqrt{2}\theta=0 \tag{5.50}$$

According to (5.37–5.40) and (5.50), we have

$$\frac{P_1+2P_2+\sqrt{2}P_3}{2}U\rho-\frac{P_1+8P_2+2\sqrt{2}P_3}{48}U^3\rho^3-\frac{k_1+16k_2+4k_3}{48}U^4\rho^3+O(\rho^5)=0 \tag{5.51}$$

For the first order approximation of (5.51), we have

$$P_1+2P_2+\sqrt{2}P_3=0 \tag{5.52}$$

From (5.52), it is clear that Nonzero preloads are crucial for the modeling of the bending resistance of the MSD model. For the preloads of the three types of spring, we have only two linear constraints (5.49) and (5.52). So we have one extra freedom to choose the values of the three preloads. We can utilize this extra degree of freedom to minimize the variation of bending resistance of the MSD model in different directions (for isotropic materials). To minimize or at least limit the variations of the bending resistance to be small is very important. Otherwise, the model will tend to bend in the direction in which it has small bending resistance. In the worst case, if the model has negative bending resistance in a certain direction, its natural rest state will not be planar.

5.3.1.2 Minimizing the Variations of the Bending Resistance in Different Directions

Referring to Fig. 5.3, assume the 2D rectangle meshed MSD model to be bent cylindrically in the direction of the y-axis, which makes an angle of ϕ with the y'-axis. The MSD system will stretch or contract by strain μ in the longitudinal direction (the x-axis) to minimize the potential energy. This strain should be a function of the curvature of the cylinder. Let

$$\mu = f_r(\rho) = \eta_{1r}\rho + \eta_{2r}\rho^2 + o(\rho^2) \tag{5.53}$$

where the subscript r is used to indicate the rectangle meshed MSD system.

Consider the shaded $b \times b$ rectangular part of the MSD model in Fig. 5.3. We can obtain the energy required to bend it into a cylinder of curvature ρ.

$$\begin{aligned} E_m^b(\phi,\rho,\mu) \;=\; & \frac{b^2}{U^2}\big(W_1(u_1)+W_1(u_2)+W_2(v_1)+W_2(v_2)+W_3(w_1)+W_3(w_2)-W_1(u_{1,0}) \\ & -W_1(u_{2,0})-W_2(v_{1,0})-W_2(v_{2,0})-W_3(w_{1,0})-W_2(w_{2,0})\big) \end{aligned} \tag{5.54}$$

where u_1 and u_2 are the displacements of the structural springs aligned with the y'-axis and the x'-axis respectively; v_1 and v_2 are the displacements of the flexion springs aligned with the y'-axis and the x'-axis respectively; w_1 and w_2 are the displacements of the shearing springs in the directions that make an angle of $\pi/4$ and $3\pi/4$ respectively with the x'-axis; $u_{1,0}$, $u_{2,0}$, $v_{1,0}$, $v_{2,0}$, $w_{1,0}$ and $w_{2,0}$ are the pre-displacements of the corresponding springs when the MSD model is in its natural rest state.

According to Fig. 5.3, by projecting the springs on the x-axis and the y-axis, we can obtain

$$u_1 - u_{1,0} \;=\; \sqrt{\Big(\frac{2}{\rho}\sin\frac{U\cos\phi\rho}{2}\Big)^2 + U^2(1+\mu)^2\sin^2\phi} - U \tag{5.55}$$

$$u_2 - u_{2,0} \;=\; \sqrt{\Big(\frac{2}{\rho}\sin\frac{U\cos(\pi/2-\phi)\rho}{2}\Big)^2 + U^2(1+\mu)^2\sin^2(\pi/2-\phi)} - U \tag{5.56}$$

$$v_1 - v_{1,0} = \sqrt{\Big(\frac{2}{\rho}\sin U\cos\phi\rho\Big)^2 + 4U^2(1+\mu)^2\sin^2\phi} - 2U \quad (5.57)$$

$$v_2 - v_{2,0} = \sqrt{\Big(\frac{2}{\rho}\sin U\cos(\pi/2-\phi)\rho\Big)^2 + 4U^2(1+\mu)^2\sin^2(\pi/2-\phi)} - 2U \quad (5.58)$$

$$w_1 - w_{1,0} = \sqrt{\Big(\frac{2}{\rho}\sin\frac{\sqrt{2}U\cos(\frac{\pi}{4}-\phi)\rho}{2}\Big)^2 + 2U^2(1+\mu)^2\sin^2(\frac{\pi}{4}-\phi)} - \sqrt{2}U \quad (5.59)$$

$$w_2 - w_{2,0} = \sqrt{\Big(\frac{2}{\rho}\sin\frac{\sqrt{2}U\cos(\frac{\pi}{4}+\phi)\rho}{2}\Big)^2 + 2U^2(1+\mu)^2\sin^2(\frac{\pi}{4}+\phi)} - \sqrt{2}U \quad (5.60)$$

From (5.34–5.39) and (5.54–5.60), we obtain

$$\begin{aligned}
\frac{\partial E_m^b(\phi,\rho,\mu)}{\partial\mu} &= \frac{b^2}{U^2}\Big(F_1(u_1)\frac{\partial u_1}{\partial\mu} + F_1(u_2)\frac{\partial u_2}{\partial\mu} + F_2(v_1)\frac{\partial v_1}{\partial\mu} \\
&\qquad + F_2(v_2)\frac{\partial v_2}{\partial\mu} + F_3(w_1)\frac{\partial w_1}{\partial\mu} + F_3(w_1)\frac{\partial w_1}{\partial\mu}\Big) \\
&= \frac{b^2}{U^2}\Big\{UP_1 + 2UP_2 + \sqrt{2}UP_3 + \big[3/4U^2(k_1+4k_2+2k_3) + \\
&\quad 1/4U^2\cos 4\phi(k_1+4k_2-2k_3) + 1/4U(P_1+2P_2+\sqrt{2}P_3) \\
&\quad -1/4U\cos 4\phi(P_1+2P_2-\sqrt{2}P_3)\big]\mu + \big[-\frac{1}{192}(k_1+16k_2+4k_3)U^4 \\
&\quad +\frac{1}{192}(k_1+16k_2-4k_3)U^4\cos 4\phi + \frac{1}{192}(P_1+8P_2+2\sqrt{2}P_3)U^3 \\
&\quad -\frac{1}{192}(P_1+8P_2-2\sqrt{2}P_3)U^3\cos 4\phi\big]\rho^2 + \big[\frac{3}{16}(k_1+4k_2+2k_3)U^2 \\
&\quad -\frac{3}{16}(k_1+4k_2-2k_3)U^2\cos 4\phi - \frac{3}{16}(P_1+2P_2+\sqrt{2}P_3)U + \\
&\quad \frac{3}{16}(P_1+2P_2-\sqrt{2}P_3)U\cos 4\phi\big]\mu^2 + o(\rho^2) + o(\mu^2) + o(\mu\rho)\Big\} \\
&= \frac{b^2}{U^2}[B\mu + C\rho^2 + G\mu^2 + o(\rho^2) + o(\mu^2) + o(\mu\rho)] \qquad (5.61)
\end{aligned}$$

where

$$\begin{aligned}
B &= \frac{3U^2}{4}(k_1+4k_2+2k_3) + \frac{U^2}{4}\cos 4\phi(k_1+4k_2-2k_3) + \\
&\quad \frac{U}{4}(P_1+2P_2+\sqrt{2}P_3) - \frac{U}{4}\cos 4\phi(P_1+2P_2-\sqrt{2}P_3) \qquad (5.62) \\
C &= -\frac{U^4}{192}(k_1+16k_2+4k_3) + \frac{U^4}{192}(k_1+16k_2-4k_3)\cos 4\phi + \\
&\quad \frac{U^3}{192}(P_1+8P_2+2\sqrt{2}P_3) - \frac{U^3}{192}(P_1+8P_2-2\sqrt{2}P_3)\cos 4\phi \qquad (5.63)
\end{aligned}$$

$$\begin{aligned} G &= \frac{3U^2}{16}(k_1+4k_2+2k_3)-\frac{3U^2}{16}(k_1+4k_2-2k_3)\cos 4\phi \\ &\quad -\frac{3U}{16}(P_1+2P_2+\sqrt{2}P_3)+\frac{3U}{16}(P_1+2P_2-\sqrt{2}P_3)\cos 4\phi \end{aligned} \tag{5.64}$$

Here and later, we use the *Maple* system to do the symbolic calculations such as taking derivatives and Taylor expansions.

Since the strain μ will minimize the potential energy of the model, we can obtain it as a function of ρ by letting $\partial E_m^b(\phi,\rho,\mu)/\partial\mu = 0$. According to (5.53) and (5.61), we have

$$B\eta_{1r}\rho + B\eta_{2r}\rho^2 + C\rho^2 + G\eta_{1r}^2\rho^2 + o(\rho^2) = 0 \tag{5.65}$$

We have $\eta_{1r} = 0$, $\eta_{2r} = -\frac{C}{B}$. Clearly, μ is negligible when ρ is small. According to (5.53), we have

$$\mu = -\frac{C}{B}\rho^2 + o(\rho^2) \tag{5.66}$$

Taking derivative with respect to ρ on both sides of (5.54), according to (5.34–5.39), (5.52), (5.55–5.60) and (5.66), we can obtain the cylindrical bending resistance.

$$\begin{aligned} \frac{dE_m^b(\phi,\rho,\mu)}{d\rho} &= \frac{b^2}{U^2}\Big(F_1(u_1)\frac{du_1}{d\rho}+F_1(u_2)\frac{du_2}{d\rho}+F_2(v_1)\frac{dv_1}{d\rho}+ \\ &\quad F_2(v_2)\frac{dv_2}{d\rho}+F_3(w_1)\frac{dw_1}{d\rho}+F_3(w_2)\frac{dw_2}{d\rho}\Big) \\ &= \frac{b^2}{U^2}\Big[F_1(u_1)\Big(\frac{\partial u_1}{\partial\rho}+\frac{\partial u_1}{\partial\mu}\frac{d\mu}{d\rho}\Big)+F_1(u_2)\Big(\frac{\partial u_2}{\partial\rho}+\frac{\partial u_2}{\partial\mu}\frac{d\mu}{d\rho}\Big) \\ &\quad +F_2(v_1)\Big(\frac{\partial v_1}{\partial\rho}+\frac{\partial v_1}{\partial\mu}\frac{d\mu}{d\rho}\Big)+F_2(v_2)\Big(\frac{\partial v_2}{\partial\rho}+\frac{\partial v_2}{\partial\mu}\frac{d\mu}{d\rho}\Big)+ \\ &\quad F_3(w_1)\Big(\frac{\partial w_1}{\partial\rho}+\frac{\partial w_1}{\partial\mu}\frac{d\mu}{d\rho}\Big)+F_3(w_2)\Big(\frac{\partial w_2}{\partial\rho}+\frac{\partial w_2}{\partial\mu}\frac{d\mu}{d\rho}\Big)\Big] \\ &= \frac{b^2}{U^2}\Big[-\frac{P_1+8P_2+2\sqrt{2}P_3}{16}U^3\rho-\frac{(P_1+8P_2-2\sqrt{2}P_3)\cos 4\phi}{48}U^3\rho+o(\rho)\Big] \end{aligned} \tag{5.67}$$

To minimize the difference of bending resistance in different directions up to the first order of the bending curvature ρ, we have

$$P_1 + 8P_2 - 2\sqrt{2}P_3 = 0 \tag{5.68}$$

According to (5.49), (5.52) and (5.68), we have

$$P_1 = \frac{6(1+\nu)D}{U} = \frac{Eh^3}{2(1-\nu)U} \tag{5.69}$$

$$P_2 = -\frac{3(1+\nu)D}{2U} = -\frac{Eh^3}{8(1-\nu)U} \tag{5.70}$$

$$P_3 = -\frac{3\sqrt{2}(1+\nu)D}{2U} = -\frac{\sqrt{2}Eh^3}{8(1-\nu)U} \tag{5.71}$$

From (5.67–5.71) we have

$$\begin{aligned} \frac{dE_m^b(\phi,\rho,\mu)}{d\rho} &= \frac{b^2}{U^2}\Big[-\frac{3P_1+24P_2+6\sqrt{2}P_3}{48}U^3\rho+O(\rho^2)\Big] \\ &\approx \frac{3(1+\nu)Db^2}{4}\rho = \frac{Eh^3b^2}{16(1-\nu)}\rho \end{aligned} \tag{5.72}$$

For the continuum plate of size $b \times b$ and depth h being bent into a cylinder with a curvature of ρ in the direction of the y-axis, the strain and stress [72] are

$$\varepsilon_{yy} = \rho z \tag{5.73}$$

$$\sigma_{yy} = \frac{E}{1-\nu^2}\varepsilon_{yy} = \frac{E\rho z}{1-\nu^2} \tag{5.74}$$

Then we can obtain the strain energy

$$E_p^b(\rho) = \int_0^{\frac{h}{2}} \sigma_{yy}\varepsilon_{yy}b^2 dz = \frac{Eb^2h^3\rho^2}{24(1-\nu^2)} \tag{5.75}$$

Thus

$$\frac{dE_p^b(\rho)}{d\rho} = \frac{Eb^2h^3\rho}{12(1-\nu^2)} \tag{5.76}$$

So the relative error of the cylindrical bending resistance that the 2D MSD model can provide compared with that of the continuum plate is

$$err_m^b \approx \frac{12(1-\nu^2)}{16(1-\nu)} - 1 = \frac{3\nu-1}{4} \tag{5.77}$$

When $\nu = 0.3$, which is the Poisson constant of most metals [76], the percentage of error is about -2.5%. So by optimizing the axisymmetric bending behavior and minimizing

the bending resistance variations in different directions, we can obtain a MSD system that provides a little weaker resistance for cylindrical bending than desired. In fact, we can also optimize the preloads of the three types of spring according to the cylindrical bending, which has a similar procedure and will cause a slight stronger resistance against axisymmetric bending.

Note that from (5.67), if we do not use preload, the MSD model will not be able to provide linear resistance against cylindrical bending when the bending curvature ρ is small. It is also worth noting that error for bending resistance is approximately zero when $\nu = 1/3$, which is exactly the Poisson constant that the 2D MSD model can achieve.

5.3.1.3 Optimizing the Hooke's Constants based on the Axisymmetric Stretching

Similar to 1D case, in this subsection, we use the axisymmetric stretch or compression as the criterion behavior to optimize the Hooke's constants. Let the circular plate in Fig. 4.7 be under the action of axisymmetric circular stretch. Then the state of plane stress exists. Assume the radial strain to be ε. Then we can obtain the strain energy of the plate (see appendix C.1 for details).

$$E_p^s(\varepsilon) = \frac{\pi E h a^2 \varepsilon^2}{1-\nu} \tag{5.78}$$

The corresponding MSD model should consume the same amount of energy under the same action.

$$N_1 W_1(u) + N_2 W_2(v) + N_3 W_3(w) - N_1 W_1(u_0) - \\ N_2 W_2(v_0) - N_3 W_3(w_0) = E_p^s(\varepsilon) = \frac{\pi E h a^2 \varepsilon^2}{1-\nu} \tag{5.79}$$

Clearly,

$$u - u_0 = U\varepsilon \tag{5.80}$$

$$v - v_0 = 2U\varepsilon \tag{5.81}$$

$$w - w_0 = \sqrt{2}U\varepsilon \tag{5.82}$$

When $a \gg U$, from (5.32) and (5.79), we have

$$W_1(u) + W_2(v) + W_3(w) - W_1(u_0) - W_2(v_0) - W_3(w_0) = \frac{EhU^2\varepsilon^2}{2(1-\nu)} \tag{5.83}$$

Taking derivative with respect to ε on both sides of (5.83) and substituting (5.34–5.36) into it, we obtain

$$F_1(u)\frac{du}{d\varepsilon} + F_2(v)\frac{dv}{d\varepsilon} + F_3(w)\frac{dw}{d\varepsilon} = \frac{EhU^2\varepsilon}{1-\nu} \tag{5.84}$$

According to (5.37–5.39), (5.80–5.82) and (5.84), we have

$$(P_1+2P_2+\sqrt{2}P_3)U+(k_1+4k_2+2k_3)U^2\varepsilon=\frac{EhU^2\varepsilon}{1-\nu} \tag{5.85}$$

We can obtain (5.52) and

$$k_1 + 4k_2 + 2k_3 = \frac{Eh}{1-\nu} \tag{5.86}$$

5.3.1.4 Minimizing the Variations of the Resistance against Stretching in Different Directions

The 2D MSD model displays different resistance against stretch or compression in different directions. It is important to minimize or at least limit the variations to be small. We will give more details on this point later in this subsection. Similar to subsection 5.3.1.2, we consider the 2D MSD model being stretched or compressed by strain ε in the direction of the y-axis, which makes angle ϕ with the y'-axis (Fig. 5.3).

Obviously, the MSD model of the rectangular plate will stretch or contract in the direction of the x-axis to minimize the potential energy. Assume this longitudinal strain is μ. It should be a function of the strain ε in the direction of the y-axis. Let

$$\mu = g_r(\varepsilon) = \lambda_{1r}\varepsilon + o(\varepsilon) \tag{5.87}$$

For the shaded $b \times b$ rectangular part of the model in Fig. 5.3, we have

$$E_m^s(\phi,\varepsilon,\mu) = \frac{b^2}{U^2}\Big(W_1(u_1)+W_1(u_2)+W_2(v_1)+W_2(v_2)+W_3(w_1)+W_3(w_2) \\ -W_1(u_{1,0})-W_1(u_{2,0})-W_2(v_{1,0})-W_2(v_{2,0})-W_3(w_{1,0})-W_3(w_{2,0})\Big) \quad (5.88)$$

where u_1 and u_2 are the displacements of the structural springs aligned with the y'-axis and the x'-axis respectively; v_1 and v_2 are the displacements of the flexion springs aligned with the y'-axis and the x'-axis respectively; w_1 and w_2 are the displacements of the shearing springs in the directions that make an angle of $\pi/4$ and $3\pi/4$ respectively with the x'-axis; $u_{1,0}$, $u_{2,0}$, $v_{1,0}$, $v_{2,0}$, $w_{1,0}$ and $w_{2,0}$ are the pre-displacements of the corresponding springs when the model is in its natural rest state.

According to Fig. 5.3, by projecting the springs on the x-axis and the y-axis, we have

$$u_1 - u_{1,0} = U\sqrt{(1+\varepsilon)^2\cos^2\phi + (1+\mu)^2\sin^2\phi} - U \quad (5.89)$$

$$u_2 - u_{2,0} = U\sqrt{(1+\varepsilon)^2\cos^2(\pi/2-\phi) + (1+\mu)^2\sin^2(\pi/2-\phi)} - U \quad (5.90)$$

$$v_1 - v_{1,0} = 2(u_1 - u_{1,0}) \quad (5.91)$$

$$v_2 - v_{2,0} = 2(u_2 - u_{2,0}) \quad (5.92)$$

$$w_1 - w_{1,0} = U\sqrt{2(1+\varepsilon)^2\cos^2(\pi/4-\phi) + 2(1+\mu)^2\sin^2(\pi/4-\phi)} - \sqrt{2}U \quad (5.93)$$

$$w_2 - w_{2,0} = U\sqrt{2(1+\varepsilon)^2\cos^2(\pi/4+\phi) + 2(1+\mu)^2\sin^2(\pi/4+\phi)} - \sqrt{2}U \quad (5.94)$$

From (5.34–5.39), (5.52) and (5.88–5.94), we can obtain

$$\frac{\partial E_m^s(\phi,\varepsilon,\mu)}{\partial\mu} = \frac{b^2}{U^2}\Big(F_1(u_1)\frac{\partial u_1}{\partial\mu} + F_1(u_2)\frac{\partial u_2}{\partial\mu} + F_2(v_1)\frac{\partial v_1}{\partial\mu} \\ +F_1(v_2)\frac{\partial v_2}{\partial\mu} + F_3(w_1)\frac{\partial w_1}{\partial\mu} + F_3(w_2)\frac{\partial w_2}{\partial\mu}\Big) \\ = \frac{b^2}{U^2}\big\{P_1U + 2P_2U + \sqrt{2}P_3U + \big[\frac{1}{4}(k_1+4k_2+2k_3)U^2 \\ -\frac{1}{4}(k_1+4k_2-2k_3)U^2\cos 4\phi - \frac{1}{4}(P_1+2P_2+\sqrt{2}P_3)U +$$

$$\frac{1}{4}(P_1+2P_2-\sqrt{2}P_3)U\cos 4\phi\big]\varepsilon+\big[\frac{3}{4}(k_1+4k_2+2k_3)U^2+$$
$$\frac{1}{4}(k_1+4k_2-2k_3)U^2\cos 4\phi+\frac{1}{4}(P_1+2P_2+\sqrt{2}P_3)U$$
$$-\frac{1}{4}(P_1+2P_2-\sqrt{2}P_3)U\cos 4\phi\big]\mu+o(\rho)+o(\mu)\big\}$$
$$= \frac{b^2}{U^2}(H\varepsilon+I\mu+o(\varepsilon)+o(\mu)) \tag{5.95}$$

where

$$H = \frac{1}{4}(k_1+4k_2+2k_3)U^2-\frac{1}{4}(k_1+4k_2-2k_3)U^2\cos 4\phi+$$
$$\frac{1}{4}(P_1+2P_2-\sqrt{2}P_3)U\cos 4\phi \tag{5.96}$$
$$J = \frac{3}{4}(k_1+4k_2+2k_3)U^2+\frac{1}{4}(k_1+4k_2-2k_3)U^2\cos 4\phi$$
$$-\frac{1}{4}(P_1+2P_2-\sqrt{2}P_3)U\cos 4\phi \tag{5.97}$$

Let $\partial E_m^s(\phi,\varepsilon,\mu)/\partial\mu=0$, we have

$$\lambda_{1r}=-\frac{H}{J} \tag{5.98}$$

From (5.34–5.39), (5.52), (5.87–5.94) and (5.98), we can obtain the resistance against stretch or compression below.

$$\frac{dE_m^s(\phi,\varepsilon,\mu)}{d\varepsilon} = \frac{b^2}{U^2}\Big(F_1(u_1)\frac{du_1}{d\varepsilon}+F_1(u_2)\frac{du_2}{d\varepsilon}+F_2(v_1)\frac{dv_1}{d\varepsilon}$$
$$+F_2(v_2)\frac{dv_2}{d\varepsilon}+F_3(w_1)\frac{dw_1}{d\varepsilon}+F_3(w_2)\frac{dw_2}{d\varepsilon}\Big)$$
$$= \frac{b^2}{U^2}\Big[F_1(u_1)\Big(\frac{\partial u_1}{\partial\varepsilon}+\frac{\partial u_1}{\partial\mu}\frac{d\mu}{d\varepsilon}\Big)+F_1(u_2)\Big(\frac{\partial u_2}{\partial\varepsilon}+\frac{\partial u_2}{\partial\mu}\frac{d\mu}{d\varepsilon}\Big)$$
$$+F_2(v_1)\Big(\frac{\partial v_1}{\partial\varepsilon}+\frac{\partial v_1}{\partial\mu}\frac{d\mu}{d\varepsilon}\Big)+F_2(v_2)\Big(\frac{\partial v_2}{\partial\varepsilon}+\frac{\partial v_2}{\partial\mu}\frac{d\mu}{d\varepsilon}\Big)+$$
$$F_3(w_1)\Big(\frac{\partial w_1}{\partial\varepsilon}+\frac{\partial w_1}{\partial\mu}\frac{d\mu}{d\varepsilon}\Big)+F_3(w_2)\Big(\frac{\partial w_2}{\partial\varepsilon}+\frac{\partial w_2}{\partial\mu}\frac{d\mu}{d\varepsilon}\Big)\Big]$$
$$= \frac{b^2}{U^2}\Big[2(k_1+4k_2+2k_3)\Big(1-\frac{(k_1+4k_2+2k_3)U^2}{2J}\Big)U^2\varepsilon+o(\varepsilon)\Big] \tag{5.99}$$

To minimize the variations of stretch or compression resistance in different directions up to the first order of the strain ε, we have

$$k_1+4k_2-2k_3=\frac{P_1+2P_2-\sqrt{2}P_3}{U}=\frac{Eh^3}{2U^2(1-\nu)} \tag{5.100}$$

According to (5.86) and (5.100), we have

$$k_3 = \frac{Eh(2U^2-h^2)}{8(1-\nu)U^2} \tag{5.101}$$

$$k_1 + 4k_2 = \frac{Eh(2U^2+h^2)}{8(1-\nu)U^2} \tag{5.102}$$

The necessity to use the shearing springs is shown in (5.101). According to (5.99), if we do not use shear springs and preloads, when $\phi = \pi/4$, the linear part of the resistance against stretch or compression will be zero. In simulation, the MSD system will roll together in the diagonal direction. From another point of view, according to the affine transformation relationship between the shear strain (stress) and the tensile strain (stress), proper modeling of stretch and compression leads to proper modeling of of shearing, and vice versa. Minimizing or limiting the variations of the resistance against stretch or compression in different directions leads to very even shear resistance in different directions.

From (5.96–5.98) and (5.100), we can get $\lambda_{1r} = -1/3$. So the Poisson constant the 2D MSD model can achieve is 1/3. From (5.97), (5.99) and (5.100) we have

$$\frac{dE_m^s(\phi,\varepsilon,\mu)}{d\varepsilon} = \frac{2b^2}{3}(k_1+4k_2+2k_3)\varepsilon + o(\varepsilon) \tag{5.103}$$

According to (5.86) and (5.103), we have

$$\frac{dE_m^s(\phi,\varepsilon,\mu)}{d\varepsilon} \approx \frac{2b^2}{3}\frac{Eh}{1-\nu}\varepsilon = \frac{2Ehb^2}{3(1-\nu)}\varepsilon \tag{5.104}$$

For the continuum rectangular plate of size $b \times b$ and depth h under in-plane stretch or compression perpendicular to its two opposite sides, in the direction of the y-axis for example, there exists the state of plane stress. The strain energy is

$$E_p^s(\varepsilon) = \frac{1}{2} E\varepsilon^2 \cdot b^2 h = \frac{1}{2} E b^2 h \varepsilon^2 \tag{5.105}$$

Then

$$\frac{dE_p^s(\varepsilon)}{d\varepsilon} = Eb^2 h\varepsilon \tag{5.106}$$

Thus, the relative error of the stretch or compression resistance that the 2D MSD model can provide compared with that of the continuum plate is

$$err_m^s \approx \frac{2}{3(1-\nu)} - 1 = \frac{3\nu - 1}{3(1-\nu)} \tag{5.107}$$

When $\nu = 0.3$, the percentage of error is -4.76%. The error is approximately zero when $\nu = 1/3$.

5.3.2 The 2D MSD Model with Equilateral Triangle Meshes

In this subsection, we are going to optimize the parameters of the 2D MSD model with equilateral triangle meshes (Fig. 5.4), which can be viewed as the direct 2D extension of the 1D structured MSD model. In this model, since the triangle mesh itself can resist shear deformation, we use only two types of spring, namely, structural springs for the edges of the triangles and flexion springs between every other masses along the directions of the edges of the triangle meshes. The dashed line segments parallel to the y'-axis are used to even the boundary of the structure for graphics display (springs are not used for these edges of the boundary triangles).

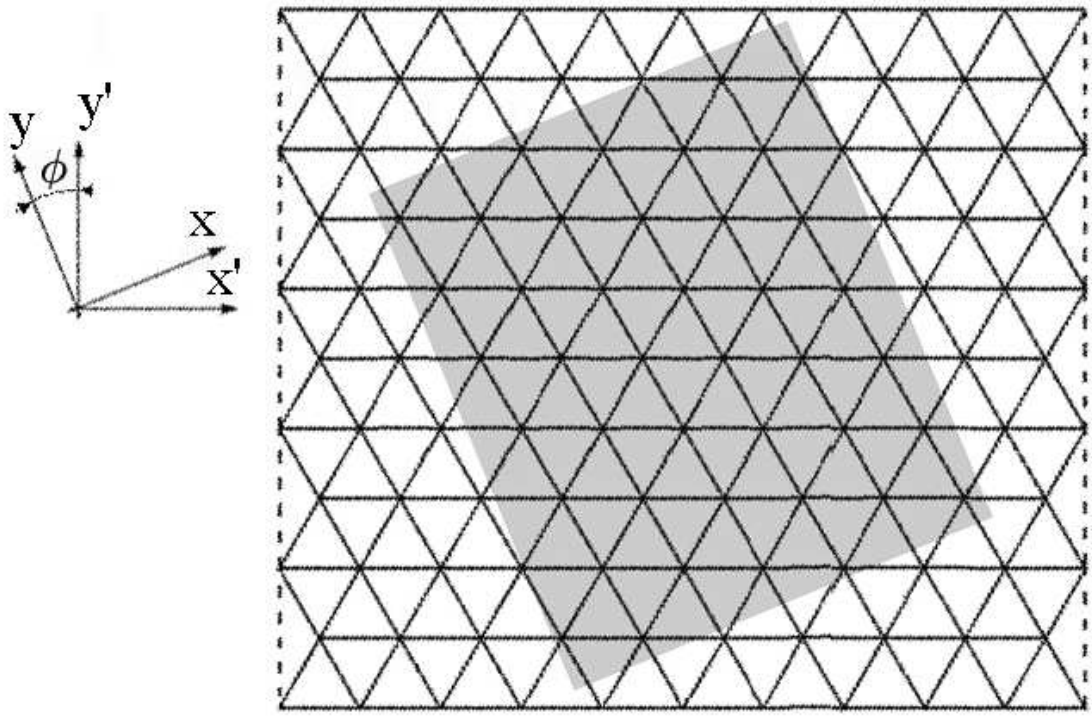

Figure 5.4. 2D equilateral triangle meshed MSD model.

5.3.2.1 Optimizing the Spring Constants based on Axisymmetric Bending

In the MSD model for the circular plate with a radius of a, assume the length of the edge of the equilateral triangle mesh to be U when the system is in its natural rest state. For the MSD system to have the same stiffness against axisymmetric bending, the energy increment in the system when bent into the same shape should be the same as its continuum counterpart. Thus

$$N_1 W_1(u) + N_2 W_2(v) - N_1 W_1(u_0) - N_2 W_2(v_0) = \pi(1+\nu) D a^2 \rho^2 \tag{5.108}$$

where u and v are the displacements of the structural springs and flexion springs and satisfy (5.7) and (5.8) respectively; N_1 and N_2 are the number of structural springs and flexion springs respectively. The area of the equilateral triangle mesh is $\sqrt{3}U^2/4$. Since each triangle has three vertices and each vertex is shared between six triangles, each

vertex corresponds to an area of $\sqrt{3}U^2/2$. For an circular area of radius a, when a is very large, the number of vertices it contains is approximately

$$N_v \approx \frac{\pi a^2}{\frac{\sqrt{3}U^2}{2}} = \frac{2\sqrt{3}\pi a^2}{3U^2} \tag{5.109}$$

Since each vertex connects to six structural (flexion) springs, and each structural (flexion) spring connects two vertices, the numbers of the two types of springs are

$$N_i \approx 3N_v \approx \frac{2\sqrt{3}\pi a^2}{U^2} \qquad (i = 1, 2) \tag{5.110}$$

From (5.108) and (5.110), when $a \gg U$, we have

$$W_1(u) + W_2(v) - W_1(u_0) - W_2(v_0) = \frac{\sqrt{3}(1+\nu)DU^2\rho^2}{6} \tag{5.111}$$

Similar to the 1D situation, we can obtain

$$-\frac{P_1 + 8P_2}{12}U^3\rho + \frac{P_1 + 32P_2}{480}U^5\rho^3 + \frac{k_1 + 64k_2}{288}U^6\rho^3 + O(\rho^5) = \frac{\sqrt{3}(1+\nu)DU^2\rho}{3} \tag{5.112}$$

For the first order approximation of (5.112), we have

$$P_1 + 8P_2 = -\frac{4\sqrt{3}(1+\nu)D}{U} \tag{5.113}$$

Similar to the 1D case, the equilibrium constraint is still (5.16). Further we can obtain (5.17) and (5.18). According to (5.18) and (5.113), we can obtain

$$P_1 = \frac{4\sqrt{3}(1+\nu)D}{3U} = \frac{\sqrt{3}Eh^3}{9(1-\nu)U} \tag{5.114}$$

$$P_2 = -\frac{2\sqrt{3}(1+\nu)D}{3U} = -\frac{\sqrt{3}Eh^3}{18(1-\nu)U} \tag{5.115}$$

For the third order approximation of (5.17) and (5.112), we can obtain

$$k_1 = \frac{4\sqrt{3}(1+\nu)D}{3U^2} = \frac{\sqrt{3}Eh^3}{9(1-\nu)U^2} \tag{5.116}$$

$$k_2 = \frac{\sqrt{3}(1+\nu)D}{6U^2} = \frac{\sqrt{3}Eh^3}{72(1-\nu)U^2} \tag{5.117}$$

The Hooke's constants specified by (5.116) and (5.117) can also be obtained by the operation point linear approximation method in chapter 4. Their values tend to be too small to model the in-plane stretch or compression resistance of the plate, which is the reason to optimize the Hooke's constants of the springs based on stretch or compression of the plate at the expense of the accuracy of the axisymmetric bending behavior.

5.3.2.2 Optimizing the Hooke's Constants based on the Axisymmetric Stretching

Similar to subsection 5.3.1.3, we can obtain the energy constraint for stretch or compression below.

$$N_1(W_1(u) - W_1(u_0)) + N_2(W_2(v) - W_2(v_0)) = \frac{\pi E h a^2 \varepsilon^2}{1-\nu} \tag{5.118}$$

Equations (5.80) and (5.81) are still valid in this case.

When $a \gg U$, from (5.110) and (5.118), we have

$$W_1(u) + W_2(v) - W_1(u_0) - W_2(v_0) = \frac{\sqrt{3} E h U^2 \varepsilon^2}{6(1-\nu)} \tag{5.119}$$

Taking derivative with respect to ε on both sides of (5.119), from (5.2–5.5), (5.80) and (5.81), we can obtain

$$(P_1 + 2P_2)U + (k_1 + 4k_2)U^2\varepsilon = \frac{\sqrt{3} E h U^2 \varepsilon}{3(1-\nu)} \tag{5.120}$$

Then we can obtain (5.18) and

$$k_1 + 4k_2 = \frac{\sqrt{3} E h}{3(1-\nu)} \tag{5.121}$$

We have one extra degree of freedom to decide k_1 and k_2, which can be used to minimize the boundary effect.

5.3.2.3 Analysis of the Bending Resistance of the Equilateral Triangle Meshed MSD Model in Different Directions

In this subsection, we check the accuracy of the cylindrical bending resistance in different directions that the equilateral triangle meshed MSD model can achieve. Similar to the case of rectangular meshes, the energy required to bend the model into a cylinder of curvature ρ in the direction of the y-axis is

$$\begin{aligned} E_m^b(\phi,\rho,\mu) &= \frac{2\sqrt{3}b^2}{3U^2}\big(W_1(u_1)+W_1(u_2)+W_1(u_3)+W_2(v_1)+W_2(v_2)+W_2(v_3) \\ &\quad -W_1(u_{1,0})-W_1(u_{2,0})-W_1(u_{3,0})-W_2(v_{1,0})-W_2(v_{2,0})-W_2(v_{3,0})\big) \quad (5.122) \end{aligned}$$

where u_1 and v_1 are the displacements of the structural spring and the flexion spring aligned with the x'-axis respectively; u_2 and v_2 are the displacements of the structural spring and the flexion spring which make an angle of $\pi/3$ with the x'-axis; u_3 and v_3 are the displacements of the structural spring and the flexion spring which make an angle of $2\pi/3$ with the x'-axis.

According to Fig. 5.4, by projecting the springs on the x-axis and the y-axis, we can obtain

$$u_1 - u_{1,0} = \sqrt{\Big(\frac{2}{\rho}\sin\frac{U\sin\phi\rho}{2}\Big)^2 + U^2(1+\mu)^2\cos^2\phi} - U \quad (5.123)$$

$$u_2 - u_{2,0} = \sqrt{\Big(\frac{2}{\rho}\sin\frac{U\sin(\pi/3-\phi)\rho}{2}\Big)^2 + U^2(1+\mu)^2\cos^2(\pi/3-\phi)} - U \quad (5.124)$$

$$u_3 - u_{3,0} = \sqrt{\Big(\frac{2}{\rho}\sin\frac{U\sin(2\pi/3-\phi)\rho}{2}\Big)^2 + U^2(1+\mu)^2\cos^2(2\pi/3-\phi)} - U \quad (5.125)$$

$$v_1 - v_{1,0} = \sqrt{\Big(\frac{2}{\rho}\sin(U\sin\phi\rho)\Big)^2 + 4U^2(1+\mu)^2\cos^2\phi} - 2U \quad (5.126)$$

$$v_2 - v_{2,0} = \sqrt{\Big(\frac{2}{\rho}\sin\big(U\sin(\pi/3-\phi)\rho\big)\Big)^2 + 4U^2(1+\mu)^2\cos^2(\pi/3-\phi)} - 2U \quad (5.127)$$

$$v_3 - v_{3,0} = \sqrt{\Big(\frac{2}{\rho}\sin\big(U\sin(2\pi/3-\phi)\rho\big)\Big)^2 + 4U^2(1+\mu)^2\cos^2(2\pi/3-\phi)} - 2U \quad (5.128)$$

From (5.2–5.5), (5.18) and (5.122–5.128), we have

$$\begin{aligned}
\frac{\partial E_m^b(\phi,\rho,\mu)}{\partial\mu} &= \frac{2\sqrt{3}b^2}{3U^2}\Big(F_1(u_1)\frac{\partial u_1}{\partial\mu}+F_1(u_2)\frac{\partial u_2}{\partial\mu}+F_1(u_3)\frac{\partial u_3}{\partial\mu}+\\
&\qquad F_2(v_1)\frac{\partial v_1}{\partial\mu}+F_2(v_2)\frac{\partial v_2}{\partial\mu}+F_2(v_3)\frac{\partial v_3}{\partial\mu}\Big)\\
&= \frac{2\sqrt{3}b^2}{3U^2}[\frac{3}{2}U(P_1+2P_2)+(\frac{3}{8}UP_1+\frac{3}{4}UP_2+\frac{9}{8}U^2k_1+\frac{9}{2}U^2k_2)\mu\\
&\quad +(\frac{9}{64}UP_1\cos6\phi+\frac{9}{32}UP_2\cos6\phi-\frac{9}{64}U^2k_1\cos6\phi\\
&\quad -\frac{9}{16}U^2k_2\cos6\phi-\frac{9}{32}UP_1-\frac{9}{16}UP_2+\frac{9}{32}U^2k_1+\frac{9}{8}U^2k_2)\mu^2+\\
&\quad (\frac{1}{256}U^3P_1\cos6\phi+\frac{1}{32}U^3P_2\cos6\phi-\frac{1}{256}U^4k_1\cos6\phi\\
&\quad -\frac{1}{16}U^4k_2\cos6\phi+\frac{1}{128}U^3P_1+\frac{1}{16}U^3P_2-\frac{1}{128}U^4k_1\\
&\quad -\frac{1}{8}U^4k_2)\rho^2+o(\rho^2)+o(\mu^2)+o(\mu\rho)]\\
&= \frac{2\sqrt{3}b^2}{3U^2}[B'\mu+C'\rho^2+G'\mu^2+o(\rho^2)+o(\mu^2)+o(\mu\rho)] \qquad (5.129)
\end{aligned}$$

where

$$\begin{aligned}
B' &= \frac{3}{8}UP_1+\frac{3}{4}UP_2+\frac{9}{8}U^2k_1+\frac{9}{2}U^2k_2=\frac{9}{8}U^2k_1+\frac{9}{2}U^2k_2 \qquad (5.130)\\
C' &= \frac{1}{256}U^3P_1\cos6\phi+\frac{1}{32}U^3P_2\cos6\phi-\frac{1}{256}U^4k_1\cos6\phi-\frac{1}{16}U^4k_2\cos6\phi+\\
&\quad \frac{1}{128}U^3P_1+\frac{1}{16}U^3P_2-\frac{1}{128}U^4k_1-\frac{1}{8}U^4k_2 \qquad (5.131)\\
G' &= \frac{9}{64}UP_1\cos6\phi+\frac{9}{32}UP_2\cos6\phi-\frac{9}{64}U^2k_1\cos6\phi-\frac{9}{16}U^2k_2\cos6\phi\\
&\quad -\frac{9}{32}UP_1-\frac{9}{16}UP_2+\frac{9}{32}U^2k_1+\frac{9}{8}U^2k_2 \qquad (5.132)
\end{aligned}$$

Since the strain μ will minimize the potential energy of the MSD system, we can obtain it as a function of ρ by letting $\partial E_m^b(\phi,\rho,\mu)/\partial\mu=0$. Assume

$$\mu=f_t(\rho)=\eta_{1t}\rho+\eta_{2t}\rho^2+o(\rho^2) \qquad (5.133)$$

where the subscript t is used to indicate the triangle meshed MSD model.

We have

$$B'\eta_{1t}\rho + B'\eta_{2t}\rho^2 + C'\rho^2 + G'\eta_{1t}^2\rho^2 + o(\rho^2) = 0 \tag{5.134}$$

Then we have $\eta_{1t} = 0$, $\eta_{2t} = -C'/B'$. Obviously, μ is negligible when ρ is very small. We have

$$\mu = -\frac{C'}{B'}\rho^2 + o(\rho^2) \tag{5.135}$$

Taking derivative with respect to ρ on both sides of (5.122), from (5.2–5.5), (5.18), (5.123–5.128) and (5.135), we can obtain the cylindrical bending resistance of the model with equilateral triangle meshes below.

$$\begin{aligned}
\frac{dE_m^b(\phi,\rho,\mu)}{d\rho} &= \frac{2\sqrt{3}b^2}{3U^2}\Big(F_1(u_1)\frac{du_1}{d\rho} + F_1(u_2)\frac{du_2}{d\rho} + F_1(u_3)\frac{du_3}{d\rho} + F_2(v_1)\frac{dv_1}{d\rho} + \\
&\qquad F_2(v_2)\frac{dv_2}{d\rho} + F_2(v_3)\frac{dv_3}{d\rho}\Big) \\
&= \frac{2\sqrt{3}b^2}{3U^2}\Big[F_1(u_1)\Big(\frac{\partial u_1}{\partial\rho} + \frac{\partial u_1}{\partial\mu}\frac{d\mu}{d\rho}\Big) + F_1(u_2)\Big(\frac{\partial u_2}{\partial\rho} + \frac{\partial u_2}{\partial\mu}\frac{d\mu}{d\rho}\Big) + \\
&\qquad F_1(u_3)\Big(\frac{\partial u_3}{\partial\rho} + \frac{\partial u_3}{\partial\mu}\frac{d\mu}{d\rho}\Big) + F_1(v_1)\Big(\frac{\partial v_1}{\partial\rho} + \frac{\partial v_1}{\partial\mu}\frac{d\mu}{d\rho}\Big) + \\
&\qquad F_1(v_2)\Big(\frac{\partial v_2}{\partial\rho} + \frac{\partial v_2}{\partial\mu}\frac{d\mu}{d\rho}\Big) + F_1(v_3)\Big(\frac{\partial v_3}{\partial\rho} + \frac{\partial v_3}{\partial\mu}\frac{d\mu}{d\rho}\Big)\Big] \\
&= \frac{2\sqrt{3}b^2}{3U^2}\Big(-\frac{3P_1 + 24P_2}{32}U^3\rho + O(\rho^2)\Big)
\end{aligned} \tag{5.136}$$

We can see that the bending resistance does not change in different directions when ρ is small. We can further obtain

$$\frac{dE_m^b(\phi,\rho,\mu)}{d\rho} \approx \frac{2\sqrt{3}b^2}{3U^2}\Big(-\frac{3P_1 + 24P_2}{32}U^3\rho\Big) = \frac{3(1+\nu)Db^2}{4}\rho = \frac{Eh^3b^2}{16(1-\nu)}\rho \tag{5.137}$$

It is interesting that the optimized MSD model with equilateral triangle meshes provides the same resistance against cylindrical bending as the one with rectangular meshes.

5.3.2.4 Analysis of the Resistance against Stretching of the Equilateral Triangle Meshed MSD Model in Different Directions

In this subsection, we check the resistance against stretch or compression in different directions that the MSD model with equilateral triangle meshes can provide. We again consider the 2D MSD model being stretched or compressed by strain ε in the direction of the y-axis, which makes an angle ϕ withe the y'-axis. The longitudinal strain associated with this strain to minimize the potential energy of the system is μ. Assume

$$\mu = g_t(\varepsilon) = \lambda_{1t}\varepsilon + o(\varepsilon) \tag{5.138}$$

For the shaded $b \times b$ rectangular part of the model in Fig. 5.4, we have

$$\begin{aligned} E_m^s(\phi, \varepsilon, \mu) \;=\; & \frac{2\sqrt{3}b^2}{3U^2}\big(W_1(u_1)+W_1(u_2)+W_1(u_3)+W_2(v_1)+W_2(v_2)+W_2(v_3) \\ & -W_1(u_{1,0})-W_1(u_{2,0})-W_1(u_{3,0})-W_2(v_{1,0})-W_2(v_{2,0})-W_2(v_{3,0})\big) \end{aligned} \tag{5.139}$$

According to Fig. 5.4, by projecting the springs on the x-axis and the y-axis, we have

$$u_1 - u_{1,0} = U\sqrt{(1+\varepsilon)^2\sin^2\phi + (1+\mu)^2\cos^2\phi} - U \tag{5.140}$$

$$u_2 - u_{2,0} = U\sqrt{(1+\varepsilon)^2\sin^2(\pi/3-\phi) + (1+\mu)^2\cos^2(\pi/3-\phi)} - U \tag{5.141}$$

$$u_3 - u_{3,0} = U\sqrt{(1+\varepsilon)^2\sin^2(2\pi/3-\phi) + (1+\mu)^2\cos^2(2\pi/3-\phi)} - U \tag{5.142}$$

$$v_1 - v_{1,0} = 2(u_1 - u_{1,0}) \tag{5.143}$$

$$v_2 - v_{2,0} = 2(u_2 - u_{2,0}) \tag{5.144}$$

$$v_3 - v_{3,0} = 2(u_3 - u_{3,0}) \tag{5.145}$$

From (5.2–5.5), (5.18), (5.139–5.145), we have

$$\begin{aligned} \frac{\partial E_m^s(\phi, \varepsilon, \mu)}{\partial \mu} \;=\; & \frac{2\sqrt{3}b^2}{3U^2}\Big(F_1(u_1)\frac{\partial u_1}{\partial \mu} + F_1(u_2)\frac{\partial u_2}{\partial \mu} + F_1(u_3)\frac{\partial u_3}{\partial \mu} + F_2(v_1)\frac{\partial v_1}{\partial \mu} + \\ & F_2(v_2)\frac{\partial v_2}{\partial \mu} + F_2(v_3)\frac{\partial v_3}{\partial \mu}\Big) \\ =\; & \frac{2\sqrt{3}b^2}{3U^2}\big(H'\varepsilon + J'\mu + o(\varepsilon) + o(\mu)\big) \end{aligned} \tag{5.146}$$

where

$$\begin{aligned} H' &= \frac{3}{8}U^2k_1 - \frac{1}{8}U^2k_1\cos 4\phi + \frac{1}{8}U^2k_1\sin\big(\frac{\pi}{6}+4\phi\big) + \frac{1}{8}U^2k_1\cos\big(\frac{\pi}{3}+4\phi\big) \\ &\quad +\frac{3}{2}U^2k_2 - \frac{1}{2}U^2k_2\cos 4\phi + \frac{1}{2}U^2k_2\sin\big(\frac{\pi}{6}+4\phi\big) + \frac{1}{2}U^2k_2\cos\big(\frac{\pi}{3}+4\phi\big) \\ &= \frac{3}{8}U^2(k_1+4k_2) \qquad (5.147) \\ J' &= U^2\left(1+\cos^4\phi - 2\cos^2\big(\frac{\pi}{6}+\phi\big) + \cos^4\big(\frac{\pi}{6}+\phi\big) + \cos^4\big(\frac{\pi}{3}+\phi\big)\right)(k_1+4k_2) \\ &= \frac{9}{8}U^2(k_1+4k_2) \qquad (5.148) \end{aligned}$$

Let $\partial E_m^s(\phi,\varepsilon,\mu)/\partial\mu = 0$, from (5.138) and (5.146–5.148) we have $\lambda_{1t} = -1/3$. Again we see that the MSD model with equilateral triangle meshes achieves the same Poisson constant as the one with rectangular meshes.

Then from (5.2–5.5), (5.18), (5.138–5.145) we can obtain the resistance of the model against stretching.

$$\begin{aligned} \frac{dE_m^s(\phi,\varepsilon,\mu)}{d\varepsilon} &= \frac{2\sqrt{3}b^2}{3U^2}\Big(F_1(u_1)\frac{du_1}{d\varepsilon} + F_1(u_2)\frac{du_2}{d\varepsilon} + F_1(u_3)\frac{du_3}{d\varepsilon} + \\ &\qquad F_2(v_1)\frac{dv_1}{d\varepsilon} + F_2(v_2)\frac{dv_2}{d\varepsilon} + F_2(v_3)\frac{dv_3}{d\varepsilon}\Big) \\ &= \frac{2\sqrt{3}b^2}{3U^2}\Big[F_1(u_1)\big(\frac{\partial u_1}{\partial\varepsilon} + \frac{\partial u_1}{\partial\mu}\frac{d\mu}{d\varepsilon}\big) + F_1(u_2)\big(\frac{\partial u_2}{\partial\varepsilon} + \frac{\partial u_2}{\partial\mu}\frac{d\mu}{d\varepsilon}\big) \\ &\qquad +F_1(u_3)\big(\frac{\partial u_3}{\partial\varepsilon} + \frac{\partial u_3}{\partial\mu}\frac{d\mu}{d\varepsilon}\big) + F_1(v_1)\big(\frac{\partial v_1}{\partial\varepsilon} + \frac{\partial v_1}{\partial\mu}\frac{d\mu}{d\varepsilon}\big) \\ &\qquad +F_1(v_2)\big(\frac{\partial v_2}{\partial\varepsilon} + \frac{\partial v_2}{\partial\mu}\frac{d\mu}{d\varepsilon}\big) + F_1(v_3)\big(\frac{\partial v_3}{\partial\varepsilon} + \frac{\partial v_3}{\partial\mu}\frac{d\mu}{d\varepsilon}\big)\Big] \\ &= \frac{2\sqrt{3}b^2}{3U^2}[U^2(k_1+4k_2)\varepsilon + o(\varepsilon)] \qquad (5.149) \end{aligned}$$

When ε is small, we have

$$\frac{dE_m^s(\phi,\varepsilon,\mu)}{d\varepsilon} \approx \frac{2\sqrt{3}b^2}{3U^2}\big[U^2(k_1+4k_2)\varepsilon\big] = \frac{2Ehb^2}{3(1-\nu)}\varepsilon \qquad (5.150)$$

This shows the MSD model with equilateral triangle meshes provides the same resistance against stretching as the one with rectangular meshes when the deformation is small.

As mentioned in subsection 5.3.1.4, the equilateral triangle meshed MSD model will also provide the same shear resistance in different directions as that with rectangular meshes.

5.3.3 Boundary Effect for 2D MSD Models of Two Different Mesh Structures

Similar to the 1D situation, the 2D MSD models with preload also have the side effect of contraction due to the imbalance of the boundary masses. As mentioned in subsection 5.3.1.3 and subsection 5.3.2.2, we have one extra degree of freedom to choose the Hooke's constants of the springs, which can be utilized to restrict the boundary effect within small ranges close to the boundary.

For the rectangle meshed MSD model, according to appendix D, we can restrict the boundary effect to the boundary springs by letting $k_2 = 0$. From (5.102), we have

$$k_1 = \frac{Eh(2U^2 + h^2)}{8(1-\nu)U^2} \tag{5.151}$$

In this situation, we modeled a plate of depth 0.1 cm and size 32 cm×24 cm with a 16×12 rectangular mesh structure. The ratio of the contraction of the structural springs (due to the boundary effect) to the desired length of the springs when the model is in its natural rest state is shown in Fig. 5.5(a). Although the boundary springs have relatively larger contractions, they are negligible in absolute terms.

For the MSD model with equilateral triangle meshes, its boundary effect is more difficult to analyze. But when $k_2 = 0$, the boundary effect is also very small. According to (5.121), we have

$$k_1 = \frac{\sqrt{3}Eh}{3(1-\nu)} \tag{5.152}$$

We modeled a plate of the same depth and same size with an equilateral triangle meshed MSD model and the boundary effect is shown in Fig. 5.5(b). We can see the boundary effect of the equilateral triangle meshed MSD model is smaller than that of the rectangle meshed MSD model.

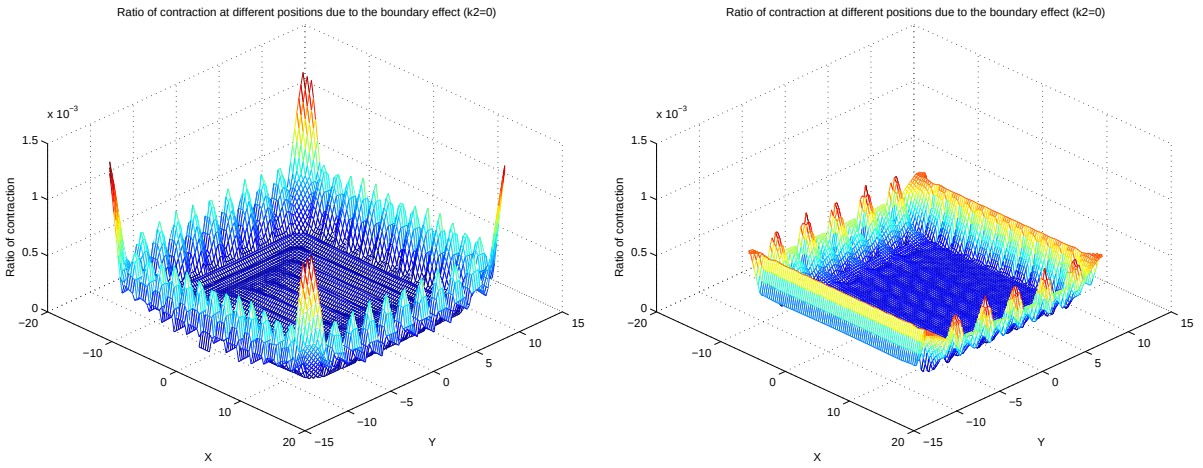

(a) (b)

Figure 5.5. (a) Ratio of contraction at different positions in the 2D MSD model with rectangular meshes; (b) ratio of contraction at different positions in the 2D MSD model with equilateral triangle meshes.

Similar to the 1D situation (see appendix B.1), when $k_2 = 0$, the boundary effects for the MSD model with two different structures above are proportional to the square of the depth h of the plate and in inverse proportion to U.

5.3.4 Lateral Resistance against Displacement for 2D MSD Models

Similar to subsection 4.3.5, in this subsection, we performed a series of experiments to obtain the numerical relationship between lateral resistance and displacement at the center of the MSD model for a circular plate of radius a for different discretization sizes n ($a = nU$). We modeled a plate with a radius of 10 cm and depth of 0.01 cm and optimized the spring constants for $n = 1$, 2, 4, 8 and 16 respectively and obtained the characteristics for two model structures as shown in Fig. 5.6(a) and 5.6(b). The solid line is the relationship indicated by (4.62) for the continuum plate. We can see that the rectangle meshed MSD model with optimized parameters does not provide correct

resistance against lateral displacement, instead, it provides much higher nonlinear lateral resistance. This is a disadvantage of the rectangle meshed model.

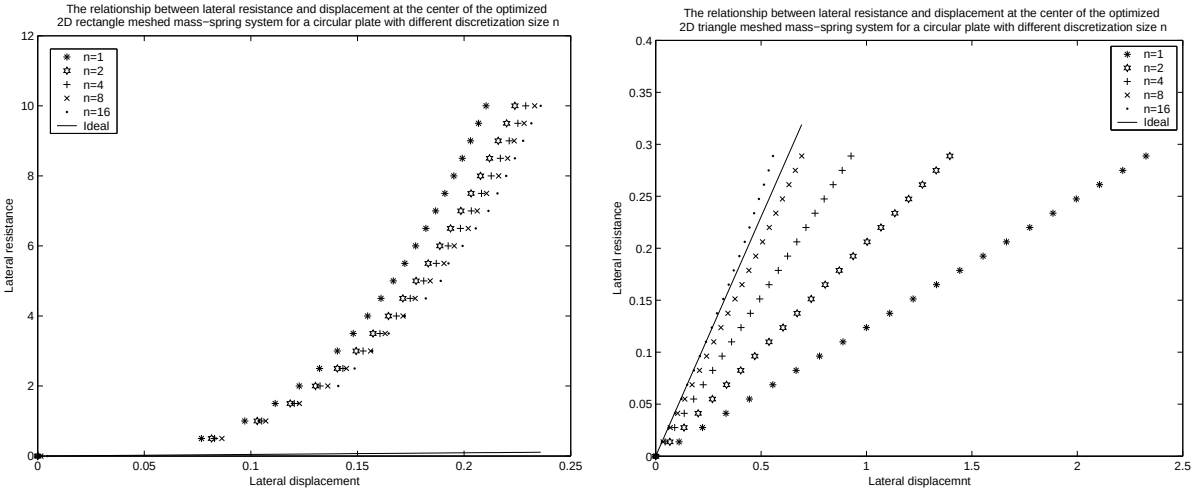

(a) (b)

Figure 5.6. (a) Lateral resistance against displacement of the rectangle meshed MSD system with preload for different discretization sizes; (b) Lateral resistance against displacement of the equilateral triangle meshed MSD system with preload for different discretization sizes.

However, for the MSD model with equilateral triangle meshes, as n increases (which means higher resolution of discretization) the relationship between lateral resistance and displacement approaches that of the continuum counterpart when the displacement is small ($d < U$). Note that the 2D MSD model with equilateral triangle meshes optimized in this chapter has the same preload as that optimized in chapter 4 but larger Hooke's constants.

In conclusion as shown in Table 5.1, the equilateral triangle mesh is superior.

Table 5.1. Comparison between the two model structures

	Rectangular mesh vs. equilateral triangle mesh
Axisymmetric bending	No difference
Cylindrical bending	No difference
Axisymmetric stretch	No difference
Stretch or shear	No difference
Lateral resistance	The equilateral triangle mesh is more accurate.
Boundary effect	The equilateral triangle mesh is smaller.
Implementation	The rectangular mesh is easier.

5.4 Conclusion

This chapter describes accurate modeling of bending (or out-of-axis or out-of-plane motion) resistance and stretching and shearing (or in-plane or in-axis motion) resistance of the MSD models for both visual effect and physical accuracy. For 1D and 2D MSD models, we demonstrate analytically and experimentally the necessity, feasibility and efficacy of using preloads for modeling bending resistance.

We demonstrate that by optimizing the bending behaviors and the stretching behaviors, we can obtain a set of parameters for the 1D and 2D MSD models to closely approximate their continuum counterparts. And for the 2D MSD models, the equilateral triangle mesh structure is shown to be more accurate than the commonly used rectangular mesh structure.

CHAPTER 6
PARAMETER OPTIMIZATION FOR THE 1D AND 2D UNSTRUCTURED MSD MODELS

6.1 Introduction

The two approaches proposed in chapter 4 and 5 for optimizing the parameters of the 1D and 2D MSD models are only suitable for structured models, while the 2D structured model is difficult to fit into an irregular shape: an ellipse and a rectangle with a hole for example. In this chapter, we extend the parameter optimization scheme to unstructured 1D and 2D MSD models by matching the influence area (range) of each node of the model and its continuum part [78]. Instead of deriving the optimal spring characteristics, we derive a set of constraints on the preloads and Hooke's constants and obtain the optimal preloads and Hooke's constants by solving two least square optimization problems under constraints. By doing so, we are also able to eliminate the undesirable boundary effect with the previous methods.

6.2 Optimizing the 1D MSD Model based on the Theory of Beam

6.2.1 Matching the Pure Bending

In this subsection, we seek constraints on the parameters of the 1D unstructured MSD model for its best approximation to its continuum counterpart—the beam, under pure bending. The beam is modeled by masses on its neutral plane linked by springs between neighboring masses and every second mass. For the MSD model to be realistic, it should be able to bend in a similar way as the beam does under certain boundary conditions (Fig. 4.2 bottom). Each spring is shared by two masses. Thus, for mass m

of the system, the energy increment in its influence range under pure bending on its N_m connecting spring is

$$W_{ms}^{b}(\rho) = \frac{1}{2}\sum_{i=1}^{N_m}\big(W_{mi}(u_{mi}) - W_{mi}(v_{mi})\big) \tag{6.1}$$

where the subscript m is used to indicate mass m, the subscript s is used to indicate the MSD model, $W_{mi}(\cdot)$ is the energy function of the ith spring connected to mass m, u_{mi} is the displacement of that spring, v_{mi} is the pre-displacement when the system is in its natural rest state. The key point is, here we don't restrict v_{mi} to be zero to give more freedom to parameter optimization. Note that for a boundary mass m, $N_m = 2$; for the mass connecting to the boundary mass, $N_m = 3$; for other masses, $N_m = 4$.

Let the force-displacement relationship function of the ith spring connected to node m be $F_{mi}(u_{mi})$. Then

$$F_{mi}(u_{mi}) = W'_{mi}(u_{mi}) \tag{6.2}$$

Assume the springs to be linear.

$$F_{mi}(u_{mi}) = P_{mi} + k_{mi}(u_{mi} - v_{mi}) \tag{6.3}$$

where $P_{mi} = F_{mi}(v_{mi})$. We call P_{mi} preload of the spring.

According to (4.2), the continuum bending elastic energy in the influence range of node m is

$$W_{mb}^{a} = \frac{1}{2}EIU\rho^2 = \frac{EI\rho^2}{4}(V_{m-1} + V_m) = B_m\rho^2 \tag{6.4}$$

where the subscript b indicates the beam, U_{mi} is the length of ith spring connected to mass m when the system is in its natural rest state, V_m is the distance between the $(m-1)$th mass and the mth mass, and

$$B_m = \frac{EI(V_{m-1} + V_m)}{4} \tag{6.5}$$

Then we have

$$\frac{1}{2}\sum_{i=1}^{N_m}\big(W_{mi}(u_{mi}) - W_{mi}(v_{mi})\big) = B_m\rho^2 \tag{6.6}$$

Next, we derive the relationship between the displacement of the spring and the bending curvature. Let θ_{mi} be the angle that the ith spring connecting to mass m faces to the center of the curvature. Let the rest length of the spring be L_{mi}. We can get

$$\theta_{mi} = \frac{U_{mi}\rho}{2} \tag{6.7}$$

$$\sin\theta_{mi} = \sin\frac{U_{mi}\rho}{2} = \frac{U_{mi}\rho}{2} - \frac{U_{mi}^3\rho^3}{48} + O(\rho^5) \tag{6.8}$$

$$\cos\theta_{mi} = \cos\frac{U_{mi}\rho}{2} = 1 - \frac{U_{mi}^2\rho^2}{8} + O(\rho^4) \tag{6.9}$$

$$u_{mi} = \frac{2}{\rho}\sin\frac{U_{mi}\rho}{2} - L_{mi} \tag{6.10}$$

$$u_{mi} - v_{mi} = \frac{2}{\rho}\sin\frac{U_{mi}\rho}{2} - U_{mi} = -\frac{U_{mi}^3\rho^2}{24} + O(\rho^4) \tag{6.11}$$

$$\frac{du_{mi}}{d\rho} = \frac{U_{mi}}{\rho}\cos\frac{U_{mi}\rho}{2} - \frac{2}{\rho^2}\sin\frac{U_{mi}\rho}{2} = -\frac{U_{mi}^3\rho}{12} + \frac{U_{mi}^5\rho^3}{480} + O(\rho^5) \tag{6.12}$$

Taking the derivative with respect to ρ on both sides of (6.6) and substitute (6.2) into it, we have

$$\frac{1}{2}\sum_{i=1}^{N_m} F_{mi}(u_{mi})\frac{du_{mi}}{d\rho} = 2B_m\rho \tag{6.13}$$

From (6.3), (6.11), (6.12) and (6.13), we have

$$\sum_{i=1}^{N_m} -\frac{P_{mi}U_{mi}^3\rho}{12} + \left(\frac{P_{mi}U_{mi}^5}{480} + \frac{k_{mi}U_{mi}^6}{288}\right)\rho^3 + O(\rho^5) = 4B_m\rho \tag{6.14}$$

For the first order approximation of (6.14), we have

$$\sum_{i=1}^{N_m} P_{mi}U_{mi}^3 = -48B_m \tag{6.15}$$

We can see that as long as we want to model the bending energy approximately, the preloads (or pre-displacements) of the springs cannot be all zero.

For the approximation of (6.14) up to the third order, we have

$$\sum_{i=1}^{N_m} 3P_{mi}U_{mi}^5 + 5k_{mi}U_{mi}^6 = 0 \tag{6.16}$$

Another point based on realism is that the masses that are not close to the boundary should be in equilibrium during axisymmetric bending without external force, i.e. the resultant force imposed by springs on the masses should be zero. Therefore,

$$\sum_{i=1}^{N_m} F_{mi} \sin \frac{U_{mi}\rho}{2} = 0 \tag{6.17}$$

and

$$\sum_{i=1}^{N_m} F_{mi}e_{mi} \cos \frac{U_{mi}\rho}{2} = 0 \tag{6.18}$$

where e_{mi} denotes the direction of the ith spring connected to node m. When the spring is on the left side of the node, $e_{mi} = 1$; otherwise, $e_{mi} = -1$.

From (6.2), (6.8), (6.11) and (6.17), we have

$$\sum_{i=1}^{N_m} \big(\frac{P_{mi}U_{mi}\rho}{2} - \frac{P_{mi}U_{mi}^3\rho^3}{48} - \frac{k_{mi}U_{mi}^4\rho^3}{48} + O(\rho^5)\big) = 0 \tag{6.19}$$

For the first order approximation of (6.19), we have

$$\sum_{i=1}^{N_m} P_{mi}U_{mi} = 0 \tag{6.20}$$

For the approximation of (6.19) up to the third order, we have

$$\sum_{i=1}^{N_m} (P_{mi}U_{mi}^3 + k_{mi}U_{mi}^4) = 0 \tag{6.21}$$

From (6.2), (6.9), (6.11) and (6.18), we have

$$\sum_{i=1}^{N_m} \big(P_{mi} - \frac{P_{mi}U_{mi}^2\rho^2}{8} - \frac{k_{mi}U_{mi}^3\rho^2}{24} + O(\rho^4)\big)e_{mi} = 0 \tag{6.22}$$

For the zeroth order approximation of (6.22), we have

$$\sum_{i=1}^{N_m} P_{mi}e_{mi} = 0 \tag{6.23}$$

Note that (6.23) is actually the equilibrium condition for each node when the system is at its natural rest state. For the approximation of (6.22) up to the second order, we have

$$\sum_{i=1}^{N_m} (3P_{mi}U_{mi}^2 + k_{mi}U_{mi}^3)e_{mi} = 0 \tag{6.24}$$

We use constraint (6.15), (6.20) and (6.23) to decide the preloads of the springs. Although we can combine them with (6.16), (6.21) and (6.24) to determine Hooke's constants, we don't do that. The first reason is that higher order approximation is much less important than the low order approximation since higher order approximation is meaningful only when the low order approximation is accurate. The second reason is that Hooke's constant is more crucial for the modeling of stretching or compressive behavior. So we will derive the constraints on Hooke's constants of the springs of the MSD model based on axial stretching in the next subsection.

6.2.2 Matching the Axial Stretching

For a beam of length U under axial stretching with strain ε, we can obtain the strain energy by using volume integral

$$E_b^s(\varepsilon) = \int_\Omega \frac{E\varepsilon^2}{2} dV = \frac{E\varepsilon^2}{2} \cdot AU = \frac{EAU}{2}\varepsilon^2 \tag{6.25}$$

where the superscript s is used to indicate stretch or compression and A is the area of the cross section of the beam.

For the MSD model under the same strain, the energy consumed by the influence range of mass m is

$$W_{ms}^s = \frac{1}{2}\sum_{i=1}^{N_m} (W_{mi}(u_{mi}) - W_{mi}(v_{mi})) \tag{6.26}$$

where

$$u_{mi} = U_{mi}(1+\varepsilon) - L_{mi} \tag{6.27}$$

Then we have

$$\frac{1}{2}\sum_{i=1}^{N_m}(W_{mi}(u_{mi})-W_{mi}(v_{mi}))=\frac{EA\varepsilon^2}{4}(V_{m-1}+V_m)=C_m\varepsilon^2 \tag{6.28}$$

where

$$C_m = \frac{EA(V_{m-1}+V_m)}{4} \tag{6.29}$$

Taking the derivative with respective to ε on both sides of (6.28), we can get

$$\frac{1}{2}\sum_{i=1}^{N_m} F_{mi}(u_{mi})\frac{du_{mi}}{d\varepsilon} = 2C_m\varepsilon \tag{6.30}$$

From (6.2), (6.11), (6.12) and (6.30), we have

$$\sum_{i=1}^{N_m} P_{mi}U_{mi} + k_{mi}U_{mi}^2\varepsilon = 4C_m\varepsilon \tag{6.31}$$

According to (6.31), (6.20) must be valid and

$$\sum_{i=1}^{N_m} k_{mi}U_{mi}^2 = 4C_m \tag{6.32}$$

Since the MSD model should be stretched uniformly, we can obtain the equilibrium equation for node m.

$$\sum_{i=1}^{N_m} (P_{mi} + k_{mi}U_{mi}\varepsilon)e_{mi} = 0 \tag{6.33}$$

According to (6.33), (6.23) must be valid and

$$\sum_{i=1}^{N_m} k_{mi}U_{mi}e_{mi} = 0 \tag{6.34}$$

Besides the constraints above, we note that the spring constants must be positive for the stability of the MSD system. And for real-time application, the spring constants must be less than some positive value M for certain time step and mass value so that the numerical integration is stable [62]. So we have

$$0 < k_{mi} < M \tag{6.35}$$

6.2.3 Solving the Spring Constants

Obviously, (6.15) is related to the accuracy of modeling the bending resistance. (6.20) and (6.23) are related to the shape of bending. i.e. if the MSD model can be bent into the circular shape by exerting proper boundary conditions. Similarly, (6.32) is related to the accuracy of modeling the stretch or compression resistance. (6.34) together with (6.23) is important for even resistance for stretch or compression at different positions. For the n-node MSD model described in subsection 6.2.1, there are $2n$–3 springs. So there are $4n-6$ unknowns ($2n-3$ preloads and $2n-3$ Hooke's constants) to be determined. At each node, (6.15) generates one instance of the linear constraint for the preloads. So (6.15) corresponds to n linear constraint for the preloads, and they are all independent. So does (6.23). However, (6.20) generates n linear constraints for the preloads among which $n-1$ are independent.

To optimize the preloads of the springs, we treat the $2n-1$ independent equations corresponding to (6.20) and (6.23) as constraints, and the n equations corresponding to (6.15) as multiple objectives. Generally it is impossible meet all those objectives simultaneously since we have $3n-1$ linear equations with $2n-3$ unknowns. In other words, we can not obtain the bending resistance around all nodes exactly.

For the optimization of the preloads, we treat (6.23) as constraints and the weighted sum of (6.15) and (6.20) as the objective function. By adjusting the weights, we obtained satisfactory results. For the optimization of the Hooke's constants, we treat (6.35) as the bounding constraint and the weighted sum of (6.32) and (6.34) as the objective function.

6.3 Optimizing the 2D MSD model based on the Theory of Plates

Figure 6.1 shows a 2D triangular mesh of a rectangular plate of constant depth with a hole and that of an elliptical plate, created by a Delaunay mesh generation software

called GMSH [79]. In the corresponding MSD model, we use "structural" springs for the edges of the triangles and assign masses for the vertices (nodes). To model bending resistance between adjacent triangles [68,69], we add "flexion" springs between the opposite vertices of adjacent triangles. We do not need "shearing" springs for the triangular meshes since this mesh structure itself can resist shear deformation. Note that structural springs and flexion springs are not defined according to specific meshes. Both types of springs interact to provide correct bending, stretching and shearing resistance.

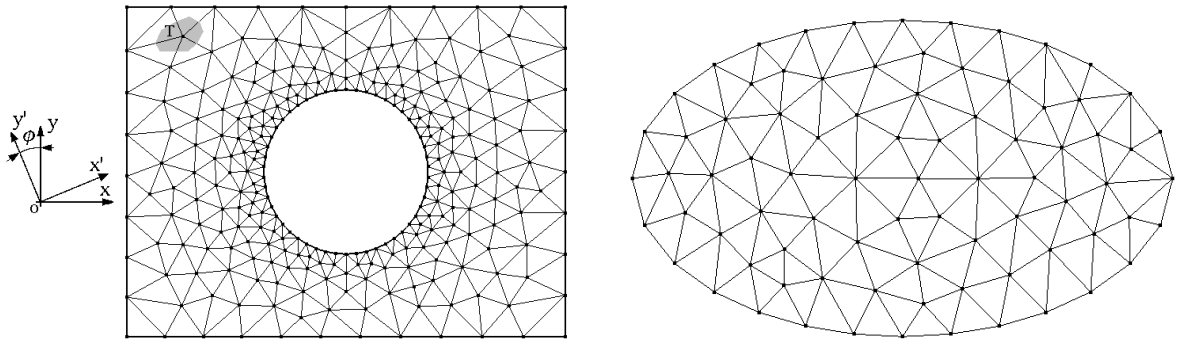

(a) (b)

Figure 6.1. (a) A 2D unstructured triangular mesh of a rectangular plate with a hole; (b) a 2D unstructured mesh of an ellipse.

We define the influence area of a vertex (node) according to the barycentric coordinate of the point in each triangle incident to this vertex. The influence area of each vertex is thus one third of the area of all the incident triangles (the shaded area in Fig. 6.1 for vertex T for example). If the plate has a constant mass density, each mass would be proportional to its influence area.

The deformation of the 2D MSD model is achieved through the *in-plane motion and out-of-plane motion* of the masses. Given a MSD model under certain external interactions, it is very hard to even tell whether the motion of an individual node is

realistic, let alone *ensure* such realism. However, we can tell the realism of the motion of a cluster of linked masses by analyzing whether they form a particular shape under certain load conditions. The primary load conditions we choose are *cylindrical bending and directional stretching* because those two loading conditions are representative of the in-plane motion and the out-of-plane motion respectively and the deformation of the plate for both cases has a simple analytic expression.

Everything that we say in this dissertation for stretch is true for compression as well. For visual realism, the MSD model should allow stretching and bending evenly without significant artifacts. Further, for physical accuracy, the model should match the physical plate in that it should have the same cylindrical bending resistance and directional stretching resistance as the physical plate.

6.3.1 Matching the Bending in Different Directions

According to continuum mechanics [72], when an isotropic plate is bent into a cylinder with a curvature of ρ under certain boundary conditions, there exists the state of plane strain. Let the x-y-z coordinate system be associated with the neutral plane of the plate with the z-axis aligned in the direction of depth and the y-axis in the direction of bending. The strain and the stress in the direction of the y-axis are

$$\varepsilon_{yy} = \rho z \tag{6.36}$$

$$\sigma_{yy} = \frac{E}{1-\nu^2}\varepsilon_{yy} = \frac{E\rho z}{1-\nu^2} \tag{6.37}$$

where E is the modulus of elasticity of the plate material and ν is the Poisson constant.

Assume the area of the plate to be A and depth to be h. We can obtain the strain energy of the plate.

$$W_p^b(\rho) = \int_0^{\frac{h}{2}} \sigma_{yy}\varepsilon_{yy} A dz = \frac{EAh^3\rho^2}{24(1-\nu^2)} \tag{6.38}$$

where the superscript b denotes the cylindrical bending and the subscript p indicates the plate.

Referring to Fig. 6.2, let the angle that the ith spring incident to node m makes with the x-axis be β_{mi}. Let the length of the ith spring incident to node m be U_{mi} when the model is in its natural rest (planar) state. Let the projection of the spring on the x'-axis be w_x and that on the y'-axis be w_y. We have $w_x = U_{mi}\cos(\beta_{mi} - \phi)$ and $w_y = U_{mi}\sin(\beta_{mi} - \phi)$.

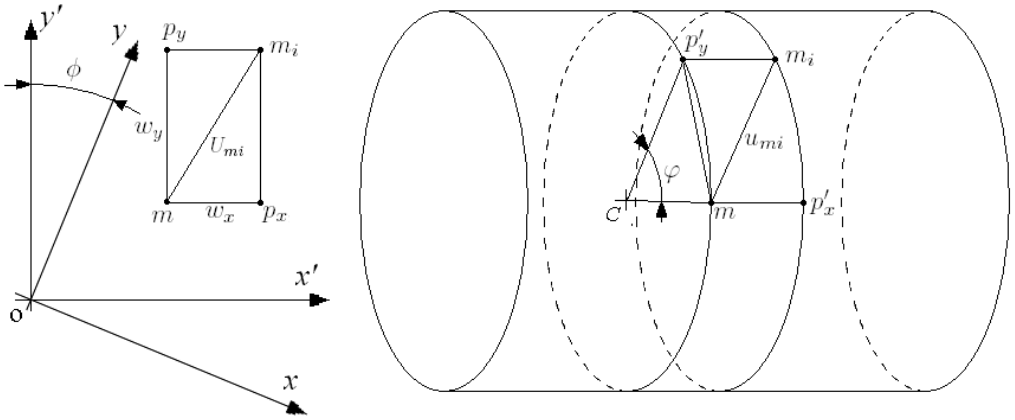

Figure 6.2. The ith spring incident to node m before and after cylindrical bending.

Assume that the 2D MSD model of the plate is bent into the shape of a cylinder of curvature ρ in the direction of the y'-axis (Fig. 6.1). The MSD model may stretch (or contract) in the longitudinal direction to minimize the potential energy of the system. Assume the associated longitudinal strain is μ. This passive strain should be small when the curvature ρ is small. We can assume

$$\mu = f(\rho) = \eta_1\rho + \eta_2\rho^2 + o(\rho^2) \tag{6.39}$$

The two projection components of the spring turn into line mp'_x and arc $\widehat{mp'_y}$ respectively (Fig. 6.2 right). Since the longitudinal strain is μ, we have

$$mp'_x = (1+\mu)w_x = (1+\mu)U_{mi}\cos(\beta_{mi}-\phi) \tag{6.40}$$

Since the neutral plane of the plate is not stretched in the latitudinal direction during the cylindrical bending, arc $\widehat{mp'_y}$ will not change its length either, i.e. $\widehat{mp'_y} = w_y$. Let the angle that this arc faces in the center C of the corresponding generating circle be φ. Then we have

$$\varphi = \rho\widehat{mp'_y} = \rho w_y = \rho U_{mi}\sin(\beta_{mi}-\phi) \tag{6.41}$$

Thus

$$mp'_y = \frac{2}{\rho}\sin\frac{\varphi}{2} = \frac{2}{\rho}\sin\frac{\rho U_{mi}\sin(\beta_{mi}-\phi)}{2} \tag{6.42}$$

Let the rest length of the ith spring incident to node m be L_{mi}, the displacement be u_{mi}, and the pre-displacement be v_{mi} when the MSD system is in its natural rest state. Obviously, $v_{mi} = U_{mi} - L_{mi}$. Here we do not restrict v_{mi} to zero to give more freedom to the parameter optimization, of which the importance will be shown later.

From (6.40) and (6.42), we can obtain

$$\begin{aligned} u_{mi} &= \sqrt{(mp'_x)^2 + (mp'_y)^2} - L_{mi} \\ &= \sqrt{(\frac{2}{\rho}\sin\frac{U_{mi}\rho\sin(\beta_{mi}-\phi)}{2})^2 + (1+\mu)^2U_{mi}^2\cos^2(\beta_{mi}-\phi)} - L_{mi} \end{aligned} \tag{6.43}$$

Let the energy function of the ith spring incident to node m be $W_{mi}(u_{mi})$, the force-displacement relationship function of the spring be $F_{mi}(u_{mi})$. Then

$$F_{mi}(u_{mi}) = W'_{mi}(u_{mi}) \tag{6.44}$$

We use linear springs. Thus

$$F_{mi}(u_{mi}) = P_{mi} + k_{mi}(u_{mi} - v_{mi}) \tag{6.45}$$

where k_{mi} is the Hooke's constant of the spring and $P_{mi} = F_{mi}(v_{mi})$. We call P_{mi} preload of the spring.

According to (6.43), we have

$$u_{mi} - v_{mi} = \sqrt{(\frac{2}{\rho}\sin\frac{U_{mi}\rho\sin(\beta_{mi}-\phi)}{2})^2 + (1+\mu)^2 U_{mi}^2\cos^2(\beta_{mi}-\phi)} - U_{mi} \quad (6.46)$$

Each spring of the MSD system is shared by two nodes. Thus, for node m of the system, the energy increment of the springs associated with its influence area under cylindrical bending is assumed to be half the energy increment of all its N_m incident springs.

$$W_{ms}^b(\phi,\rho,\mu) = \frac{1}{2}\sum_{i=1}^{N_m}(W_{mi}(u_{mi}) - W_{mi}(v_{mi})) \quad (6.47)$$

where the subscript s denotes the MSD model.

From (6.44), (6.45), (6.46) and (6.47), we obtain

$$\begin{aligned}\frac{\partial W_{ms}^b(\phi,\rho,\mu)}{\partial\mu} &= \frac{1}{2}\sum_{i=1}^{N_m}F_{mi}(u_{mi})\frac{\partial u_{mi}}{\partial\mu} \\ &= G_1 + G_2\mu + G_3\rho^2 + G_4\mu^2 + o(\mu^2) + o(\rho^2) + o(\mu\rho) \quad (6.48)\end{aligned}$$

where

$$G_1 = \sum_{i=1}^{N_m}\frac{P_{mi}U_{mi}}{4}(1+\cos 2(\beta_{mi}-\phi)) \quad (6.49)$$

$$G_2 = \sum_{i=1}^{N_m}\frac{P_{mi}U_{mi}}{8}\sin^2 2(\beta_{mi}-\phi) + \frac{k_{mi}U_{mi}^2}{2}\cos^4(\beta_{mi}-\phi) \quad (6.50)$$

$$G_3 = \sum_{i=1}^{N_m}\frac{3(k_{mi}U_{mi}-P_{mi})}{4}U_{mi}\cos^4(\beta_{mi}-\phi)\sin^2(\beta_{mi}-\phi) \quad (6.51)$$

$$G_4 = \sum_{i=1}^{N_m}\frac{P_{mi}-k_{mi}U_{mi}}{48}U_{mi}^3\cos^2(\beta_{mi}-\phi)\sin^4(\beta_{mi}-\phi) \quad (6.52)$$

Since the strain μ will minimize the potential energy of the MSD system, we can obtain it as a function of the curvature ρ by imposing $\frac{\partial W_{ms}^{b}(\phi,\rho,\mu)}{\partial \mu} = 0$. According to (6.39) and (6.48), we have

$$G_1+G_2\eta_1\rho+G_2\eta_2\rho^2+G_3\rho^2+G_4\eta_1^2\rho^2+o(\rho^2)=0 \tag{6.53}$$

From (6.49) and (6.53), we get

$$\sum_{i=1}^{N_m} \frac{P_{mi}U_{mi}}{2}(1+\cos 2(\beta_{mi}-\phi)) = 0 \tag{6.54}$$

Note that (6.54) is very important for the prevention of the irregular Poisson effect of the MSD model under cylindrical bending. If the summation on the left side is large, μ will not be small when ρ is small and the model will show undesired drastic transverse deformations under slight bending. Even worse, the model will not be able to maintain its planar shape when it is its natural rest state.

Since ϕ is an arbitrary angle, from (6.54), we have

$$\sum_{i=1}^{N_m} P_{mi}U_{mi} = 0 \tag{6.55}$$

$$\sum_{i=1}^{N_m} P_{mi}U_{mi}\sin 2\beta_{mi} = 0 \tag{6.56}$$

$$\sum_{i=1}^{N_m} P_{mi}U_{mi}\cos 2\beta_{mi} = 0 \tag{6.57}$$

Under the condition of (6.54), from (6.53), we can obtain $\eta_1 = 0$ and $\eta_2 = -\frac{G_3}{G_2}$. Thus μ is negligible when ρ is small, which is consistent with the plate theory. From (6.39), we have

$$\mu = -\frac{G_3}{G_2}\rho^2 + o(\rho^2) \tag{6.58}$$

Taking the derivative with respect to ρ on both sides of (6.47), from (6.44), (6.45), (6.46), (6.56), (6.57) and (6.58), we can obtain

$$\begin{aligned}
\frac{dW^b_{ms}(\phi,\rho,\mu)}{d\rho} &= \frac{1}{2}\sum_{i=1}^{N_m} F_{mi}(u_{mi})(\frac{\partial u_{mi}}{\partial \rho}+\frac{\partial u_{mi}}{\partial \mu}\frac{d\mu}{d\rho}) \\
&= \sum_{i=1}^{N_m}\Bigg[\frac{P_{mi}U_{mi}}{2}\eta_2(1+\cos 2\beta_{mi}\cos 2\phi+\sin 2\beta_{mi}\sin 2\phi)+ \\
&\qquad \frac{P_{mi}U^3_{mi}}{192}(-3+4\sin 2\beta_{mi}\sin 2\phi+4\cos 2\beta_{mi}\cos 2\phi \\
&\qquad\qquad -\sin 4\beta_{mi}\sin 4\phi-\cos 4\beta_{mi}\cos 4\phi)\Bigg]\rho+o(\rho) \\
&= \sum_{i=1}^{N_m}\frac{P_{mi}U^3_{mi}}{192}(-3+4\sin 2\beta_{mi}\sin 2\phi+4\cos 2\beta_{mi}\cos 2\phi \\
&\qquad -\sin 4\beta_{mi}\sin 4\phi-\cos 4\beta_{mi}\cos 4\phi)\rho+o(\rho) \qquad (6.59)
\end{aligned}$$

From (6.59), to have the same bending resistance in different directions, we can obtain

$$\sum_{i=1}^{N_m} P_{mi}U^3_{mi}\sin 2\beta_{mi}=0 \qquad (6.60)$$

$$\sum_{i=1}^{N_m} P_{mi}U^3_{mi}\cos 2\beta_{mi}=0 \qquad (6.61)$$

$$\sum_{i=1}^{N_m} P_{mi}U^3_{mi}\sin 4\beta_{mi}=0 \qquad (6.62)$$

$$\sum_{i=1}^{N_m} P_{mi}U^3_{mi}\cos 4\beta_{mi}=0 \qquad (6.63)$$

From (6.59), under the condition of (6.60–6.63), we obtain the cylindrical bending resistance corresponding to the influence area of node m.

$$\frac{dW^b_{ms}(\phi,\rho,\mu)}{d\rho} = -\frac{1}{64}\sum_{i=1}^{N_m} P_{mi}U^3_{mi}\rho+o(\rho) \qquad (6.64)$$

According to (6.38), the strain energy of the plate corresponding to the influence area of node m is

$$W_{pm}^{b}(\rho) = \int_{0}^{\frac{h}{2}} \sigma_{yy}\varepsilon_{yy} A dz = \frac{EA_m h^3 \rho^2}{24(1-\nu^2)} \tag{6.65}$$

where A_m is the influence area of node m.

To achieve physical accuracy, the MSD model in the influence area of an arbitrary node m should have the same cylindrical bending stiffness as the continuum plate. From (6.64) and (6.65), we can obtain

$$\sum_{i=1}^{N_m} P_{mi} U_{mi}^{3} = -\frac{16EA_m h^3}{3(1-\nu^2)} \tag{6.66}$$

From (6.66), we can clearly see the necessity to use preload on the springs for the correct modeling of the bending resistance. When we use preload on the springs, any node m should be in equilibrium when the MSD is in its natural rest state. Thus

$$\sum_{i=1}^{N_m} P_{mi} \sin\beta_{mi} = 0 \tag{6.67}$$

$$\sum_{i=1}^{N_m} P_{mi} \cos\beta_{mi} = 0 \tag{6.68}$$

6.3.2 Matching the Stretching in Different Directions

Assume the MSD model to be evenly stretched by strain ε in the direction of the y'-axis, which makes angle ϕ with the y-axis (Fig. 6.1). The model will contract in the direction of the x'-axis to minimize the potential energy. Assume this longitudinal strain is μ. It should be a function of the strain ε. To have a regular Poisson effect, let

$$\mu = g(\varepsilon) = \lambda_1\varepsilon + \lambda_2\varepsilon^2 + o(\varepsilon^2) \tag{6.69}$$

The energy increment associated with node m of the model is

$$W_{ms}^{s}(\phi,\varepsilon,\mu) = \frac{1}{2}\sum_{i=1}^{N_m}(W_{mi}(u_{mi}) - W_{mi}(v_{mi})) \tag{6.70}$$

where the superscript s indicates the stretching.

According to Fig. 6.1, by projecting the springs on the x'-axis and the y'-axis, we can obtain

$$u_{mi} - v_{mi} \;=\; U_{mi}\sqrt{(1+\varepsilon)^2\sin^2(\beta_{mi}-\phi)+(1+\mu)^2\cos^2(\beta_{mi}-\phi)} - U_{mi} \qquad (6.71)$$

According to (6.44), (6.45) and (6.69–6.71), under the condition of (6.55), (6.56) and (6.57), we obtain

$$\begin{aligned}\frac{\partial W^s_{ms}(\phi,\varepsilon,\mu)}{\partial\mu} &= \frac{1}{2}\sum_{i=1}^{N_m} F_{mi}(u_{mi})\frac{\partial u_{mi}}{\partial\mu} \\ &= \frac{1}{2}\big(2G_1 + H_1\mu + H_2\varepsilon + o(\mu) + o(\varepsilon)\big) \qquad (6.72)\end{aligned}$$

where

$$H_1 \;=\; \sum_{i=1}^{N_m}\frac{1}{4}P_{mi}U_{mi}\sin^2 2(\beta_{mi}-\phi) + k_{mi}U_{mi}^2\cos^4(\beta_{mi}-\phi) \qquad (6.73)$$

$$H_2 \;=\; \sum_{i=1}^{N_m}\frac{1}{4}(k_{mi}U_{mi}-P_{mi})U_{mi}\sin^2 2(\beta_{mi}-\phi) \qquad (6.74)$$

Note that (6.54) (or (6.55), (6.56) and (6.57)) is also crucial for the prevention of the irregular Poisson effect of the model under directional stretching.

By letting $\frac{\partial W^s_{ms}(\phi,\varepsilon,\mu)}{\partial\mu} = 0$, from (6.69) and (6.72) we can obtain $H_1\lambda_1 + H_2 = 0$. Under the condition of (6.55), we get

$$\begin{aligned}&(3\lambda_1+1)\sum_{i=1}^{N_m}k_{mi}U_{mi}^2 + 4\lambda_1\sum_{i=1}^{N_m}k_{mi}U_{mi}^2\sin 2\beta_{mi}\sin 2\phi + \\ &4\lambda_1\sum_{i=1}^{N_m}k_{mi}U_{mi}^2\cos 2\beta_{mi}\cos 2\phi + (1-\lambda_1)\sum_{i=1}^{N_m}(P_{mi}U_{mi}-k_{mi}U_{mi}^2)\sin 4\beta_{mi}\sin 4\phi + \\ &(1-\lambda_1)\sum_{i=1}^{N_m}(P_{mi}U_{mi}-k_{mi}U_{mi}^2)\cos 4\beta_{mi}\cos 4\phi = 0\end{aligned}$$

Since $-\lambda_1$ corresponds to the Poisson constant, it is desired not to change with angle ϕ. Thus $\lambda_1 = -\frac{1}{3}$ and

$$\sum_{i=1}^{N_m} k_{mi} U_{mi}^2 \sin 2\beta_{mi} = 0 \tag{6.75}$$

$$\sum_{i=1}^{N_m} k_{mi} U_{mi}^2 \cos 2\beta_{mi} = 0 \tag{6.76}$$

$$\sum_{i=1}^{N_m} (P_{mi} U_{mi} - k_{mi} U_{mi}^2) \sin 4\beta_{mi} = 0 \tag{6.77}$$

$$\sum_{i=1}^{N_m} (P_{mi} U_{mi} - k_{mi} U_{mi}^2) \cos 4\beta_{mi} = 0 \tag{6.78}$$

Taking the derivative with respect to ε on both sides of (6.70), from (6.44), (6.45), (6.55), (6.56), (6.57), (6.75), (6.76), (6.77) and (6.78), we can obtain the tensile resistance of the MSD model corresponding to the influence area of node m.

$$\frac{dW_{ms}^s(\phi, \varepsilon, \mu)}{d\varepsilon} = \frac{1}{2} \sum_{i=1}^{N_m} F_{mi}(u_{mi}) \left(\frac{\partial u_{mi}}{\partial \varepsilon} + \frac{\partial u_{mi}}{\partial \mu} \frac{d\mu}{d\varepsilon} \right) = \frac{1}{2} \sum_{i=1}^{N_m} \frac{k_{mi} U_{mi}^2}{3} \varepsilon + o(\varepsilon) \tag{6.79}$$

For a plate of area A_m and depth h under stretching in a certain direction, there exists the state of plane stress. The strain energy of the plate corresponding to the influence area of node m is

$$W_{mp}^s(\varepsilon) = \frac{1}{2} E \varepsilon^2 \cdot A_m h = \frac{1}{2} E A_m h \varepsilon^2 \tag{6.80}$$

To achieve physical accuracy for the MSD model, the model should have the same stretching stiffness in the influence are of node m as the plate. From (6.79) and (6.80), we can obtain

$$\sum_{i=1}^{N_m} k_{mi} U_{mi}^2 = 6 E A_m h \tag{6.81}$$

Besides the constraints above, the Hooke's constants must be nonnegative for the stability of the MSD system.

$$k_{mi} \geq 0 \tag{6.82}$$

6.3.3 Analysis of the Axisymmetric Bending Stiffness

In this section, we are going to check the axisymmetric bending stiffness of the MSD model under the constraints we have derived, to partially validate our optimization method. According to the elasticity theory of plate [71, 72], when an isotropic circular plate of constant depth is bent by moments uniformly distributed along its edge, it will deform into a parabolic surface. Assume the depth and radius of the plate to be h and a respectively ($h \ll a$). Let the rotation angle on the edge of the plate be α. When $\alpha \ll 1$, the curvature is approximately the same everywhere, and hence the parabolic surface can be approximated by a spherical cap with a radius of $R = 1/\rho$ (Fig. 4.7). Then the elastic energy distribution is approximately uniform. Thus, from (4.33), for any region of area A on the plate, the bending elastic energy is

$$W_p^a(\rho) = (1+\nu)DA\rho^2 \tag{6.83}$$

Assume that the 2D MSD model of the circular plate is bent into a spherical cap of curvature ρ. Since the middle plane of the plate is assumed to be unstrained in the continuum theory of plates, we assume the geodesic between adjacent masses of the MSD system for the plate does not change either. Let the length of the ith spring incident to node m be U_{mi} when the model is in its natural rest (planar) state and the angle it faces to the center of the great circle be $2\theta_{mi}$ when the model is bent into a spherical cap (Fig. 6.3).

According to Fig. 6.3, we can get

$$\theta_{mi} = U_{mi}\rho \tag{6.84}$$

$$u_{mi} - v_{mi} = \frac{2}{\rho}\sin\frac{\theta_{mi}}{2} - U_{mi} = \frac{2}{\rho}\sin\frac{U_{mi}\rho}{2} - U_{mi} = -\frac{U_{mi}^3\rho^2}{24} + O(\rho^4) \tag{6.85}$$

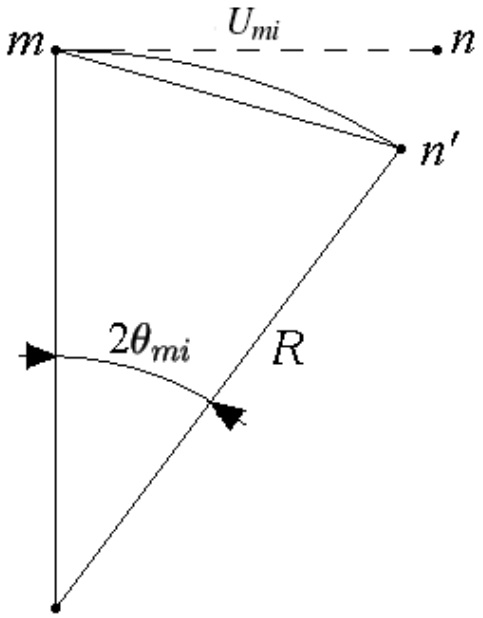

Figure 6.3. The ith spring incident to node m before (dashed line) and after (solid line) the axisymmetric bending.

The energy increment of the springs associated with the influence area of node m under axisymmetric bending is half the energy increment of all its N_m incident springs, i.e.

$$W_{ms}^{a}(\rho) = \frac{1}{2}\sum_{i=1}^{N_m}(W_{mi}(u_{mi}) - W_{mi}(v_{mi})) \tag{6.86}$$

where the superscript a is used to indicate axisymmetric bending.

According to (6.44), (6.45), (6.85) and (6.86), we can obtain the bending resistance of the MSD model in the influence area of node m.

$$\frac{\partial W_{ms}^{a}(\rho)}{\partial \rho} = -\sum_{i=1}^{N_m}\frac{P_{mi}U_{mi}^{3}}{24}\rho + o(\rho) = \frac{2EA_m h^3}{9(1-\nu^2)}\rho + o(\rho) \tag{6.87}$$

So if all the constraints are satisfied, the relative error of the axisymmetric bending resistance that the 2D MSD model can provide compared with that of the continuum plate is

$$err_m^b \approx \frac{12}{9(1+\nu)} - 1 = \frac{1-3\nu}{3(1+\nu)} \tag{6.88}$$

When $\nu = 1/3$, which is exactly the only Poisson constant that the 2D MSD model can achieve, the relative error is approximately zero.

6.3.4 Analysis of the Axisymmetric Stretching Stiffness

In this section, we are going to check the axisymmetric stretching stiffness of the MSD model under the constraints we have derived. Assume the MSD model is axisymmetircally stretched by a radial strain of ε. For node m of the MSD model under axisymmetric stretching, the corresponding energy increment is

$$W_{ms}^{c}(\varepsilon) = \frac{1}{2}\sum_{i=1}^{N_m}\left(W_{mi}(u_{mi}) - W_{mi}(v_{mi})\right) \tag{6.89}$$

where $u_{mi} = U_{mi}(1+\varepsilon) - L_{mi}$ and the superscript c indicates the axisymmetric stretching. We have

$$u_{mi} - v_{mi} = U\varepsilon \tag{6.90}$$

From (6.44), (6.45), (6.55), (6.89) and (6.90), we can obtain the axisymmetric stretching resistance.

$$\frac{dW_{ms}^{c}(\varepsilon)}{d\varepsilon} = \frac{1}{2}\sum_{i=1}^{N_m} P_{mi}U_{mi} + k_{mi}U_{mi}^{2}\varepsilon = \frac{1}{2}\sum_{i=1}^{N_m} k_{mi}U_{mi}^{2}\varepsilon = 3EA_m h\varepsilon \tag{6.91}$$

Let the circular plate in Fig. 4.7 be axisymmetrically stretched. Then a state of plane stress exists. Assume the change of radius to be Δa, and then we can obtain the radial strain, tangential strain and shear strain.

$$\varepsilon_{rr} = \varepsilon_{\theta\theta} = \frac{\Delta a}{a} = \varepsilon \tag{6.92}$$

$$\gamma_{r\theta} = 0 \tag{6.93}$$

Further we can obtain the strain energy of the plate.

$$W_{p}^{c}(\varepsilon) = \int_{0}^{\Delta a} 2\pi a h\sigma_{rr}(r)dr = \int_{0}^{\Delta a}\frac{2\pi a h E r}{(1-\nu)a}dr = \frac{\pi E h a^{2}\varepsilon^{2}}{1-\nu} \tag{6.94}$$

The strain energy is the same everywhere when a plate is under axisymmetric stretching. Thus for area A_m on the plate corresponding to the influence area of node m, the strain energy is

$$W^c_{mp}(\varepsilon) = \frac{EA_m h\varepsilon^2}{1-\nu} \tag{6.95}$$

Then the axisymmetric resistance is

$$\frac{dW^c_{mp}(\varepsilon)}{d\varepsilon} = \frac{2EA_m h\varepsilon}{1-\nu} \tag{6.96}$$

Thus, if all the constraints are satisfied, the relative error of the tensile resistance that the 2D MSD model provides compared with that of the continuum plate is

$$err^s_m = \frac{3(1-\nu)}{2} - 1 = \frac{1-3\nu}{2} \tag{6.97}$$

When $\nu = 1/3$, the relative error is approximately zero.

6.3.5 Solving the Spring Constants

In subsection 6.3.1, we derived ten constraints (6.55), (6.56), (6.57), (6.60), (6.61), (6.62), (6.63), (6.66), (6.67) and (6.68) on the preloads of the springs in the MSD system by matching the cylindrical bending of the model and the plate in different directions. Equation (6.67) and (6.68) are hard constraints since they are the equilibrium conditions for the masses of the model in its natural rest state. Equation (6.55), (6.56) and (6.57) are soft constraints allowing for small errors, and they are important for the regularity of the cylindrical bending shape (and also zero bending resistance threshold). Practically, violation of these constraints often result in annoying artifacts. Equation (6.60), (6.61), (6.62) and (6.63) are soft constraints to limit the variations of the cylindrical bending resistance in different directions. Equation (6.66) is also a soft constraint, which determines the magnitude of the cylindrical bending stiffness.

Similarly, in subsection 6.3.2, we obtained five equality constraints (6.75), (6.76), (6.77), (6.78) and (6.81) on the Hooke's constants of the MSD model, among which (6.75), (6.76), (6.77) and (6.78) constrain the model to have the same Poisson effect and tensile stiffness in different directions, and (6.81) determines the magnitude of the directional stretching stiffness. Note that (6.55), (6.56) and (6.57) are also essential for the model to have a regular Poisson effect under directional stretching (and also zero stretching resistance threshold).

From another point of view, for visual realism of the cylindrical bending in terms of limiting the artifacts, we have constraints (6.55), (6.56) and (6.57). For the physical accuracy with respect to bending, we have constraints (6.60), (6.61), (6.62), (6.63) and (6.66). With constraint (6.67), (6.68) for the equilibrium of the model in its natural rest state, we have ten equality constraints on the preloads of the springs at each node. Similarly, for the visual realism of the directional stretching, we have constraints (6.55), (6.56) and (6.57). For the physical accuracy, we have constraint (6.75), (6.76), (6.77), (6.78) and (6.81). With constraint (6.82) for the stability of the model, we have five equality constraints and one inequality constraint on the Hooke's constants of the springs at each node. Note that (6.77) and (6.78) are viewed as the constraints on the Hooke's constants because we will optimize the preloads on the spring in the first phase and the Hooke's constants in the second.

Assume the triangular mesh (obtained by Delaunay triangulation) has N_v vertices with N_b of them on the boundary, N_h holes, N_t triangles and N_e edges with N_g of them on the boundary. Assume the MSD model has N_s springs. Since every triangle has three edges and each edge is shared by two adjacent triangles except those on the boundary, we have

$$2N_e - N_g = 3N_t \tag{6.98}$$

Since the flexion springs are added between the opposite vertices of adjacent triangles, each edge corresponds to a flexion spring except those on the boundary. In the triangular mesh obtained through Delaunay triangulation, usually there are very few interior vertices that have a valence of 4. Fig. 6.4 (a) shows a vertex M of valence 4. For triangle pair $\triangle MM_1M_2$ and $\triangle MM_4M_1$, we need to add a flexion spring between M_2 and M_4. For triangle pair $\triangle MM_2M_3$ and $\triangle MM_3M_4$, we need to add another flexion spring between M_2 and M_4. These two flexion springs are dependent, and thus we only add one flexion spring between M_2 and M_4. Similar argument is true for the flexion spring between M_1 and M_4.

Even more rare, there are interior vertices of valence 3, which is only present in the vicinity of the small input angle on the boundary for Delaunay triangulation. For a vertex of valence 3, as shown in Fig. 6.4 (b), we will not add a flexion spring for triangle pair QQ_1Q_2 and QQ_3Q_1 since this spring, if added, is not independent of the structural spring between Q_2 and Q_3. Similarly we will not add flexion springs between Q_1 and Q_2, and Q_1 and Q_3 either.

For an interior vertex of valence greater than 4, we can always add an independent flexion spring striding each of its incident edges. Assume the numbers of interior vertices that have valences of 3 and 4 to be N_3 and N_4 respectively. Then the number of flexion springs is $N_e - N_g - 3N_3 - 2N_4$. Thus we have

$$N_s - N_e = N_e - N_g - 3N_3 - 2N_4 \tag{6.99}$$

From (6.98) and (6.99), we have

$$N_s = 3N_t - 3N_3 - 2N_4 \tag{6.100}$$

Next we calculate the sum of all the angles of the triangles of the mesh. For each interior vertex, the sum of all the angles incident to it is 360. For the N_{b0} vertices on

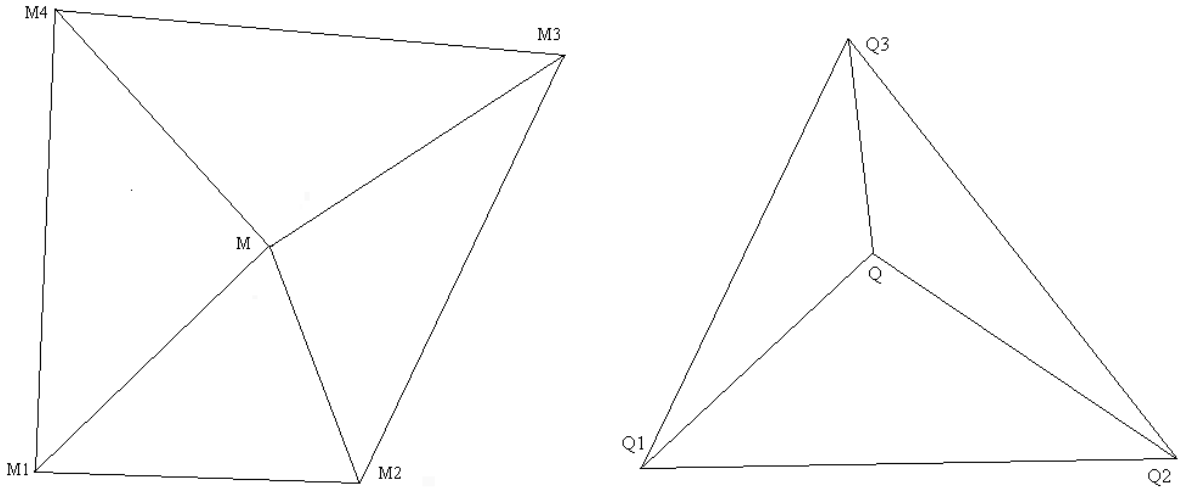

Figure 6.4. (a) Triangles incident to vertex M of valence 4; (b) Triangles incident to vertex Q of valence 3.

the outer boundary of the mesh, the sum of the angles incident to them is $180(N_{b0}-2)$. For the N_{bi} vertices of the ith hole ($i=1,2,\cdots,N_h$), the sum of the angles incident to them is $180(N_{bi}+2)$. Obviously, $N_b=\sum_{i=0}^{N_h} N_{bi}$. Then the sum of all the angles of the triangles of the mesh obtained by adding the angles incident to each vertex is

$$\begin{aligned} S &= 360(N_v-N_b)+180(N_{b0}-2)+\sum_{i=1}^{N_h}180(N_{bi}+2) \\ &= 360(N_v+N_h-N_b-1)+180N_b \end{aligned} \tag{6.101}$$

Since the sum of the angles of each triangle is 180 degrees, we have

$$N_t=\frac{S}{180}=2(N_v+N_h-1)-N_b \tag{6.102}$$

Usually $N_h, N_3, N_4 \ll N_v$. From (6.100) and (6.102), we have

$$N_s=6(N_v+N_h-1)-3N_b-3N_3-2N_4\approx 6N_v-3N_b \tag{6.103}$$

For the MSD model of a 2D planar plate with triangular meshes, we have $10N_v-2$ independent equations (constraints (6.67) and (6.68) each generate N_v-1 independent

equations) to solve the N_s preloads of the springs, and $5N_v$ equations and N_v inequations to solve the N_s Hooke's constants. Thus they are both overdetermined problems and can be solved by the constrained linear-least square method. Of course, the resulting MSD system will be less accurate than the ideal case in subsection 6.3.1 and 6.3.2 where all the constraints can be met. To obtain the preloads of the springs, we minimize the objective function below and treat (6.67) and (6.68) as hard constraints.

$$\begin{aligned}\Psi_1 = \sum_{m=1}^{N_v}\Bigg\{ & w_1\Big(\sum_{i=1}^{N_m} P_{mi}U_{mi}\Big)^2 + w_2\Big(\sum_{i=1}^{N_m} P_{mi}U_{mi}^3 + 48B_m\Big)^2 + w_3\Big(\sum_{i=1}^{N_m} P_{mi}U_{mi}\sin 2\beta_{mi}\Big)^2 + \\ & w_3\Big(\sum_{i=1}^{N_m} P_{mi}U_{mi}\cos 2\beta_{mi}\Big)^2 + w_4\Big(\sum_{i=1}^{N_m} P_{mi}U_{mi}^3\sin 2\beta_{mi}\Big)^2 + w_4\Big(\sum_{i=1}^{N_m} P_{mi}U_{mi}^3\cos 2\beta_{mi}\Big)^2 + \\ & w_5\Big(\sum_{i=1}^{N_m} P_{mi}U_{mi}^3\sin 4\beta_{mi}\Big)^2 + w_5\Big(\sum_{i=1}^{N_m} P_{mi}U_{mi}^3\cos 4\beta_{mi}\Big)^2\Bigg\} \end{aligned} \tag{6.104}$$

where w_1, w_2, w_3, w_4 and w_5 are the weights.

After obtaining P_{mi}'s ($i = 1, 2, \cdots, N_m$, $m = 1, 2, \cdots, N_v$), we solve another minimization problem under the inequality constraint (6.82) to obtain the Hooke's constants k_{mi}'s. The objective function can be formulated in a similar way as (6.104).

6.4 Simulation

6.4.1 Comparing the optimized MSD model and the FEM

First, we simulate the MSD model of a $32\,\text{cm}\times 24\,\text{cm}$ plate of depth $0.1\,\text{cm}$ ($E = 1.0\times 10^7\,\text{N/cm}^2$, ν=0.3) clamped horizontally at one short end and loaded by a force $F = 1\,\text{N}$ at one corner on the other end (Fig. 6.5(a)). Unlike chapter 5, here we use the unstructured MSD model with triangular meshes. We compare the deformations of the MSD model with preload and without preload with the deformation obtained by ANSYS (an FEM software package). The relative errors for the largest deformations of the MSD model with preload and without preload are 7.8% and 20 times respectively. The deformation comparison is shown in Fig. 6.5(b). For the preloaded MSD model, the

deformation is very close to and almost indistinguishable from that obtained by FEM, which validates our parameter optimization scheme.

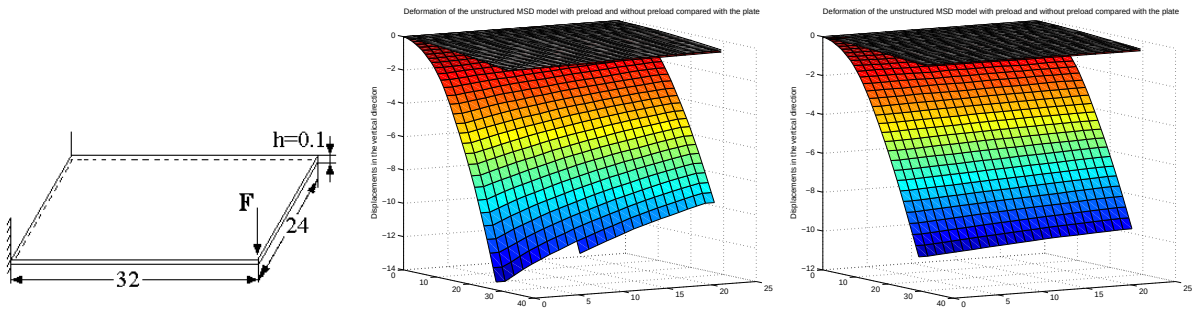

(a) (b) (c)

Figure 6.5. (a) A plate clamped at one end and loaded at one of the corners on the other end; (b) Comparison of the results from the unstructured MSD model with preload (middle), without preload (bottom) and the FEM result (top) under point load at one corner; (c) Comparison of the results from the unstructured MSD model with (middle) and without (bottom) preload, and the FEM result (top) under pressure load.

We also simulate the MSD model of the clamped plate above under downward pressure $P = 0.002\text{N/cm}^2$. The relative errors for the largest deformations are 28% and 33.5 times respectively. The deformation comparison is shown in Fig. 6.5(c).

Second, we simulate the unstructured MSD model of a $32\,\text{cm} \times 24\,\text{cm}$ plate of depth $0.1\,\text{cm}$ with a hole of radius $6.0\,\text{cm}$ at the center clamped horizontally at one short end and loaded by a force $F = 1\,\text{N}$ at one corner on the other end. The relative errors for the largest deformations are 16% and 19.2 times respectively. The deformation comparison is shown in Fig. 6.6(a).

We also simulate the MSD model of the clamped plate above under downward pressure $P = 0.002\,\text{N/cm}^2$. The relative errors for the largest deformations are 45% and 39.3 times respectively. The deformation comparison is shown in Fig. 6.6(b). The

deformation of the preloaded MSD model is also very close to that from FEM, which further validates our parameter optimization scheme.

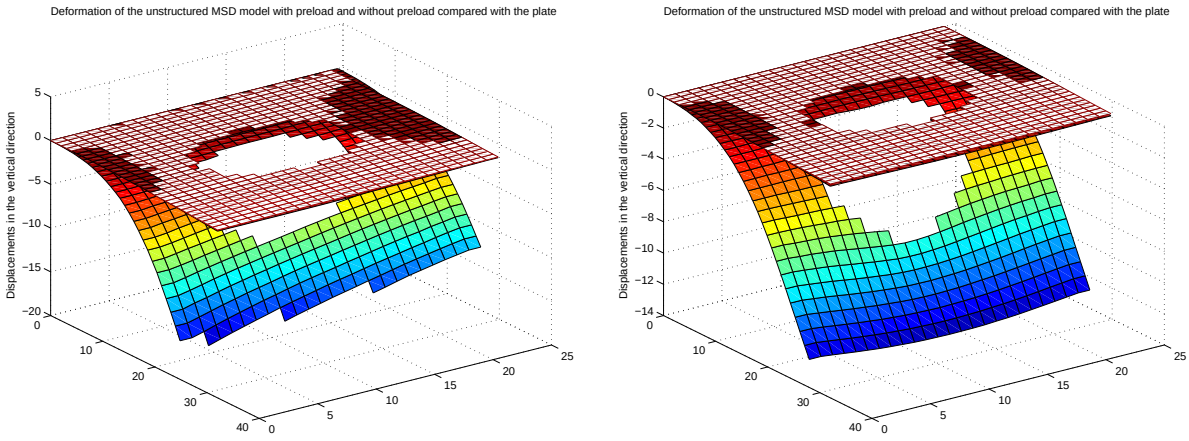

(a) (b)

Figure 6.6. Comparison of the results from the unstructured MSD model with preload (middle), without preload (bottom) and the FEM result (top) under point load at one corner (a) and under pressure load (b).

6.4.2 Simulation of the mesh placement procedure

In traditional MSD model based cloth simulation, all the springs were assumed to be at rest when the system is in its natural rest state. As shown in subsection 6.3.3 and 6.3.1, such a scheme will not be physically correct with respect to bending resistance.

In this subsection we will simulate the mesh placement procedure in a VR based hernia surgery simulation, in which a plastic mesh is placed upon the defective area of the abdominal wall of the patient. During the procedure, the plastic mesh is trimmed into a proper shape (close to an ellipse), rolled into a cylinder by hand. The it is inserted into the abdominal area where it unrolls itself. The surgeon use instruments to place and fix the mesh at a proper position. There are two problems for the traditional MSD model to model this plastic mesh. First, the traditional model usually uses rectangular

meshes, which has difficulty modeling irregular shapes. Second, the traditional model has zero first order resistance against bending, thus it flattens out very slowly when the curvature is very small.

For this simulation, we preset the MSD model rolled spirally. In the polar coordinate system with origin at the center of the cylinder of the outer tube, let the position of the masses be

$$r(\beta) = R_t(1 - c\beta) \tag{6.105}$$

When the simulation starts, the MSD model will span out to achieve an equilibrium condition in the tube: the outer layer is constrained by the tube and the inner layers are constrained by outer layers of the model. The penetration of the inner layer into the outer layers is resolved by forcing the inner layer and its adjacent outer layer spaced between a certain interval $[T_l, T_h]$. The initial setting of the MSD model is shown in Fig. 6.7(a) and a snap shot of the simulation is shown in Fig. 6.7(b). The MSD model with preload unrolls very fast (much faster than that without preload) and looks very realistic.

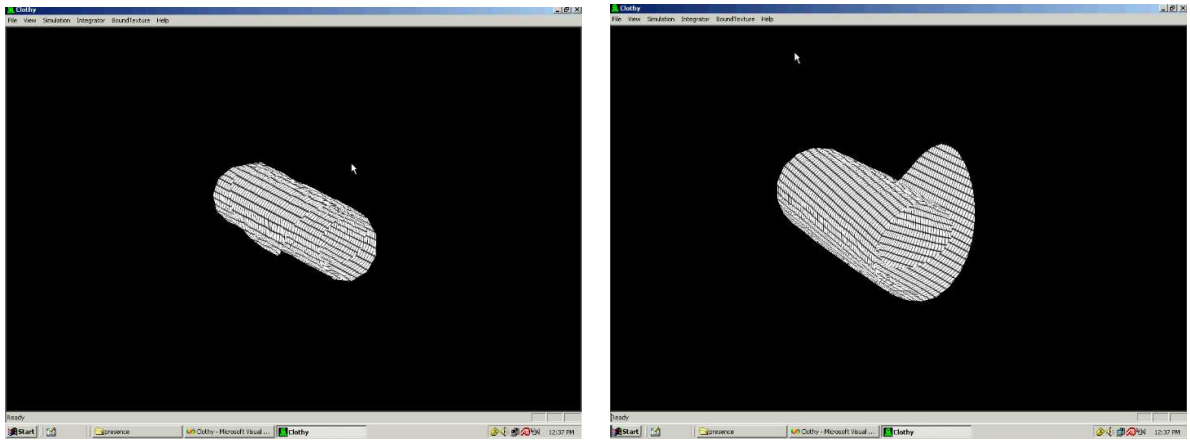

(a) (b)

Figure 6.7. The initial setting (a) and the unrolling process (b) of the plastic mesh.

6.5 Conclusion

This chapter investigates accurate modeling of bending resistance, stretching resistance and shearing resistance of the 2D MSD models with unstructured triangular meshes. We show analytically and experimentally the necessity and efficacy of using preloads for modeling bending resistance. We believe our work exploits the potential of the 2D MSD model and makes it much more realistic and usable where physical accuracy of the model is critical.

We demonstrate that by optimizing the bending behaviors and the stretching behaviors, we can obtain a set of parameters for the 2D MSD model to closely approximate its continuum counterpart. The resulting MSD model can be applied in surgical simulations or computer games supporting haptics.

CHAPTER 7

3D MSD MODEL PARAMETER OPTIMIZATION

7.1 Introduction

In this chapter, the parameter optimization scheme is extended to 3D MSD models for both structured meshes and unstructured meshes [80]. Since the 3D MSD model does not have the same difficulty modeling bending resistance as the 1D and 2D MSD models, preload is not indispensable for its physical accuracy. From another point of view, using preload will make the optimization scheme much more complicated without significant payoff in terms of accuracy. Therefore, we choose not to use preloads for the 3D MSD model.

Usually, hexahedral meshes are adopted for the 3D MSD model. The MSD model with this structured meshes can be viewed as a discrete approximation method for integrating the Lagrange differential equation of motion [81] or as a finite difference of the wave equation [82] [83]. Although the parameters of the structured MSD model can be estimated from the material properties by either method, the coupling effect between shearing resistance and tensile resistance modeling has not been resolved.

Generally we have to use the 3D unstructured MSD model to fit the irregular boundary of the deformable object. Since the tetrahedron mesh is the most common 3D unstructured mesh, we propose a method to optimize the parameters of the MSD model with tetrahedral meshes based on continuum mechanics theory. This method can also be applied to 3D structured MSD models. Particularly, this method can resolve the coupling effect between shearing resistance and tensile resistance completely and results in a very effective and accurate model.

7.2 3D Unstructured MSD Model Parameter Optimization

7.2.1 Matching the Model and the Real Object in Different Directions

The 3D MSD model of a real object is constructed based on its tetrahedral meshes by applying springs for all the edges of the tetrahedra and masses for all the vertices. Fig. 7.1 shows the 3D MSD model with tetrahedral meshes of a circular shaft.

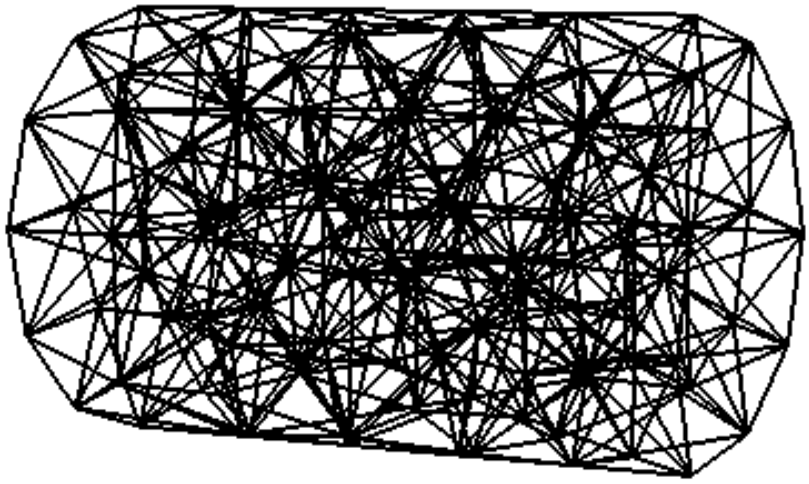

Figure 7.1. The 3D MSD model with tetrahedral meshes of a circular shaft.

Let the angle that the ith spring emanating from node m makes with the z-axis be α_{mi}, and the angle that its projection on the x–y plane makes with the x-axis be β_{mi}. Then the unit directional vector of the spring is $\vec{e}_{mi} = (\sin\alpha_{mi}\cos\beta_{mi},\ \sin\alpha_{mi}\sin\beta_{mi},\ \cos\alpha_{mi})$. Assume the ith spring incident to node m to be at rest when the model is in its natural rest state, its rest length to be U_{mi}, and its displacement to be u_{mi} when the model deforms.

Let the energy function of the ith spring incident to node m be $W_{mi}(u_{mi})$, and the force-displacement relationship function of the spring be $F_{mi}(u_{mi})$. Then

$$F_{mi}(u_{mi}) = W'_{mi}(u_{mi}) \tag{7.1}$$

We use linear springs (without preload). Thus

$$F_{mi}(u_{mi}) = k_{mi}u_{mi} \tag{7.2}$$

where k_{mi} is the Hooke's constant of the spring.

Assume the MSD model to be evenly stretched by strain ε in the direction of vector $\vec{n}$. The model will contract transversely to minimize the potential energy. Assume this longitudinal strain to be μ. It should be a function of the strain ε in the direction of the y-axis. To have regular Poisson effects, we can assume

$$\mu = g(\varepsilon) = \lambda_1\varepsilon + \lambda_2\varepsilon^2 + o(\varepsilon^2) \tag{7.3}$$

Assume that $\vec{n} = (\sin\alpha\cos\beta, \sin\alpha\sin\beta, \cos\alpha)$. Let the angle that vector $\vec{e}_{mi}$ makes with vector $\vec{n}$ be ϕ_{mi}. Then

$$\cos\phi_{mi} = \sin\alpha\cos\beta\sin\alpha_{mi}\cos\beta_{mi} + \sin\alpha\sin\beta\sin\alpha_{mi}\sin\beta_{mi} + \cos\alpha\cos\alpha_{mi} \tag{7.4}$$

By projecting the spring in the direction of $\vec{n}$, we can obtain

$$u_{mi} = \left(\sqrt{(1+\varepsilon)^2\cos^2\phi_{mi} + (1+\mu)^2\sin^2\phi_{mi}} - 1\right)U_{mi} \tag{7.5}$$

Each spring of the MSD system is shared by two nodes. Thus, for node m of the system, the energy increment of the springs associated with its influence volume under directional stretching is half the energy increment of all its N_m incident springs.

$$W^s_{ms}(\alpha, \beta, \varepsilon, \mu) = \frac{1}{2}\sum_{i=1}^{N_m} W_{mi}(u_{mi}) \tag{7.6}$$

where the superscript s indicates the stretch and the subscript s is used to indicate the MSD system.

Then

$$\begin{aligned}\frac{\partial W^s_{ms}(\alpha,\beta,\varepsilon,\mu)}{\partial\mu} &= \frac{1}{2}\sum_{i=1}^{N_m} F_{mi}(u_{mi})\frac{\partial u_{mi}}{\partial\mu} \\ &= \frac{1}{2}\sum_{i=1}^{N_m} k_{mi}U^2_{mi}(\sin^4\phi_{mi}\mu + \sin^2\phi_{mi}\cos^2\phi_{mi}\varepsilon) + o(\varepsilon) + o(\mu) \\ &= \frac{1}{2}(A_1\mu + A_2\varepsilon) + o(\varepsilon) + o(\mu) \qquad (7.7)\end{aligned}$$

where

$$A_1 = \sum_{i=1}^{N_m} k_{mi}U^2_{mi}\sin^4\phi_{mi} \qquad (7.8)$$

$$A_2 = \sum_{i=1}^{N_m} k_{mi}U^2_{mi}\sin^2\phi_{mi}\cos^2\phi_{mi} \qquad (7.9)$$

From (7.3) and (7.7), we have $\lambda_1 A_1 + A_2 = 0$. Then

$$\sum_{i=1}^{N_m}\frac{k_{mi}U^2_{mi}}{8}[1 + 3\lambda_1 - 4\lambda_1\cos 2\phi_{mi} + (\lambda_1 - 1)\cos 4\phi_{mi}] = 0 \qquad (7.10)$$

From (7.4), we can obtain

$$\begin{aligned}\cos 2\phi_{mi} &= \sum_{m,n}[a_{m,n}\cos(m\alpha+n\beta) + b_{m,n}\sin(m\alpha+n\beta)] \\ &\quad (m = 0, 2, n = 0, \pm1, \pm2) \qquad (7.11)\\ \cos 4\phi_{mi} &= \sum_{m,n}[c_{m,n}\cos(m\alpha+n\beta) + d_{m,n}\sin(m\alpha+n\beta)] \\ &\quad (m = 0, 2, 4, n = 0, \pm1, \pm2, \pm3, \pm4) \qquad (7.12)\end{aligned}$$

where the nonzero coefficients are listed in appendix E.1.

From (7.10-7.12), we can obtain

$$\sum_{i=1}^{N_m} k_{mi}U^2_{mi}[1 + 3\lambda_1 - 4\lambda_1 a_{0,0} + (\lambda_1 - 1)c_{0,0}] = 0 \qquad (7.13)$$

$$\sum_{i=1}^{N_m} k_{mi}U^2_{mi}[-4\lambda_1 a_{m,n} + (\lambda_1 - 1)c_{m,n}] = 0 \qquad (7.14)$$

$$\sum_{i=1}^{N_m} k_{mi}U^2_{mi}[-4\lambda_1 b_{m,n} + (\lambda_1 - 1)d_{m,n}] = 0 \qquad (7.15)$$

Since α and β are arbitrary, from (7.10-7.12), (E.1), (E.3), (E.13), (E.16) and (E.25), we can obtain

$$\sum_{i=1}^{N_m} k_{mi}U_{mi}^2[69 + 251\lambda_1 + (4 - 68\lambda_1)\cos 2\alpha_{mi} + 9(\lambda_1 - 1)\cos 4\alpha_{mi}] = 0 \quad (7.16)$$

$$\sum_{i=1}^{N_m} k_{mi}U_{mi}^2[1 - 17\lambda_1 + (4 - 52\lambda_1)8\cos 2\alpha_{mi} + 5(\lambda_1 - 1)\cos 4\alpha_{mi}] = 0 \quad (7.17)$$

$$\sum_{i=1}^{N_m} k_{mi}U_{mi}^2[9 + 20\cos 2\alpha_{mi} + 35\cos 4\alpha_{mi}] = 0 \quad (7.18)$$

Let $x = \sum_{i=1}^{N_m} k_{mi}U_{mi}^2$, $y = \sum_{i=1}^{N_m} k_{mi}U_{mi}^2 \cos 2\alpha_{mi}$, $z = \sum_{i=1}^{N_m} k_{mi}U_{mi}^2 \cos 4\alpha_{mi}$. From (7.16), (7.17) and (7.18), we have

$$(69 + 251\lambda_1)x + (4 - 68\lambda_1)y + (9\lambda_1 - 9)z = 0 \quad (7.19)$$

$$(1 - 17\lambda_1)x + (4 - 52\lambda_1)y + (5\lambda_1 - 5)z = 0 \quad (7.20)$$

$$9x + 20y + 35z = 0 \quad (7.21)$$

It is desired λ_1 is the same negative value at every node for arbitrary values of α and β. To have nonzero solutions to the equation system above, we have $\lambda_1 = -\frac{1}{4}$ or $\frac{1}{8}$. Thus $\lambda_1 = -\frac{1}{4}$. Further we can get

$$y = -\frac{1}{3}x \quad (7.22)$$

$$z = -\frac{1}{15}x \quad (7.23)$$

From (7.10-7.12) and (E.1–E.51), we can obtain

$$\sum_{i=1}^{N_m} k_{mi}U_{mi}^2[69 + 251\lambda_1 + (4 - 68\lambda_1)\cos 2\alpha_{mi} + 9(\lambda_1 - 1)\cos 4\alpha_{mi}] = 0 \quad (7.24)$$

$$\sum_{i=1}^{N_m} k_{mi}U_{mi}^2[(20\lambda_1 - 4)\cos 2\alpha_{mi}\cos 2\beta_{mi} + (1-17\lambda_1)\cos 2\beta_{mi} + 3(1-\lambda_1)\cos 4\alpha_{mi}\cos 2\beta_{mi}] = 0 \quad (7.25)$$

$$\sum_{i=1}^{N_m} k_{mi}U_{mi}^2[(20\lambda_1 - 4)\cos 2\alpha_{mi}\sin 2\beta_{mi} + (1-17\lambda_1)\sin 2\beta_{mi} +$$

$$3(1-\lambda_1)\cos 4\alpha_{mi}\sin 2\beta_{mi}]=0 \tag{7.26}$$

$$\sum_{i=1}^{N_m} k_{mi}U_{mi}^2[1-17\lambda_1+(4-52\lambda_1)\cos 2\alpha_{mi}+5(1-\lambda_1)\cos 4\alpha_{mi}]=0 \tag{7.27}$$

$$\sum_{i=1}^{N_m} k_{mi}U_{mi}^2[(18\lambda_1-2)\sin 2\alpha_{mi}\sin\beta_{mi}+(1-\lambda_1)\sin 4\alpha_{mi}\sin\beta_{mi}]=0 \tag{7.28}$$

$$\sum_{i=1}^{N_m} k_{mi}U_{mi}^2[(18\lambda_1-2)\sin 2\alpha_{mi}\cos\beta_{mi}+(1-\lambda_1)\sin 4\alpha_{mi}\cos\beta_{mi}]=0 \tag{7.29}$$

$$\sum_{i=1}^{N_m} k_{mi}U_{mi}^2[(5\lambda_1-1)\cos 2\beta_{mi}-4\lambda_1\cos 2\alpha_{mi}\cos 2\beta_{mi}+$$
$$(1-\lambda_1)\cos 4\alpha_{mi}\cos 2\beta_{mi}=0 \tag{7.30}$$

$$\sum_{i=1}^{N_m} k_{mi}U_{mi}^2[(5\lambda_1-1)\sin 2\beta_{mi}-4\lambda_1\cos 2\alpha_{mi}\sin 2\beta_{mi}+$$
$$(1-\lambda_1)\cos 4\alpha_{mi}\sin 2\beta_{mi}=0 \tag{7.31}$$

$$\sum_{i=1}^{N_m} k_{mi}U_{mi}^2[9\cos 4\beta_{mi}-12\cos 2\alpha_{mi}\cos 4\beta_{mi}+3\cos 4\alpha_{mi}\cos 4\beta_{mi}]=0 \tag{7.32}$$

$$\sum_{i=1}^{N_m} k_{mi}U_{mi}^2[9\sin 4\beta_{mi}-12\cos 2\alpha_{mi}\sin 4\beta_{mi}+3\cos 4\alpha_{mi}\sin 4\beta_{mi}]=0 \tag{7.33}$$

$$\sum_{i=1}^{N_m} k_{mi}U_{mi}^2[2\sin 2\alpha_{mi}\sin 3\beta_{mi}-\sin 4\alpha_{mi}\sin 3\beta_{mi}]=0 \tag{7.34}$$

$$\sum_{i=1}^{N_m} k_{mi}U_{mi}^2[2\sin 2\alpha_{mi}\cos 3\beta_{mi}-\sin 4\alpha_{mi}\cos 3\beta_{mi}]=0 \tag{7.35}$$

$$\sum_{i=1}^{N_m} k_{mi}U_{mi}^2[35\cos 4\alpha_{mi}+20\cos 2\alpha_{mi}+9]=0 \tag{7.36}$$

$$\sum_{i=1}^{N_m} k_{mi}U_{mi}^2[2\sin 2\alpha_{mi}\sin\beta_{mi}+7\sin 4\alpha_{mi}\sin\beta_{mi}]=0 \tag{7.37}$$

$$\sum_{i=1}^{N_m} k_{mi}U_{mi}^2[2\sin 2\alpha_{mi}\cos\beta_{mi}+7\sin 4\alpha_{mi}\cos\beta_{mi}]=0 \tag{7.38}$$

$$\sum_{i=1}^{N_m} k_{mi}U_{mi}^2[3\cos 2\beta_{mi}+4\cos 2\alpha_{mi}\cos 2\beta_{mi}-7\cos 4\alpha_{mi}\cos 2\beta_{mi}]=0 \tag{7.39}$$

$$\sum_{i=1}^{N_m} k_{mi}U_{mi}^2[3\sin 2\beta_{mi}+4\cos 2\alpha_{mi}\sin 2\beta_{mi}-7\cos 4\alpha_{mi}\sin 2\beta_{mi}]=0 \tag{7.40}$$

Equation (7.25), (7.30) and (7.39) are not independent since we can obtain (7.25) by adding (7.30) multiplied by -4 and (7.39) multiplied by $\lambda_1 - 1$. We have a similar argument for (7.26), (7.31) and (7.40).

From (7.28–7.29) and (7.37–7.38), we can obtain

$$\sum_{i=1}^{N_m} k_{mi} U_{mi}^2 \sin 2\alpha_{mi} \sin \beta_{mi} = 0 \tag{7.41}$$

$$\sum_{i=1}^{N_m} k_{mi} U_{mi}^2 \sin 2\alpha_{mi} \cos \beta_{mi} = 0 \tag{7.42}$$

$$\sum_{i=1}^{N_m} k_{mi} U_{mi}^2 \sin 4\alpha_{mi} \sin \beta_{mi} = 0 \tag{7.43}$$

$$\sum_{i=1}^{N_m} k_{mi} U_{mi}^2 \sin 4\alpha_{mi} \cos \beta_{mi} = 0 \tag{7.44}$$

Substituting $\lambda_1 = -\frac{1}{4}$ into (7.24), (7.27-7.31), we have

$$\sum_{i=1}^{N_m} k_{mi} U_{mi}^2 (25 + 84 \cos 2\alpha_{mi} - 45 \cos 4\alpha_{mi}) = 0 \tag{7.45}$$

$$\sum_{i=1}^{N_m} k_{mi} U_{mi}^2 (21 + 68 \cos 2\alpha_{mi} - 25 \cos 4\alpha_{mi}) = 0 \tag{7.46}$$

$$\sum_{i=1}^{N_m} k_{mi} U_{mi}^2 (5 \sin 4\alpha_{mi} \sin \beta_{mi} - 26 \sin 2\alpha_{mi} \sin \beta_{mi}) = 0 \tag{7.47}$$

$$\sum_{i=1}^{N_m} k_{mi} U_{mi}^2 (5 \sin 4\alpha_{mi} \cos \beta_{mi} - 26 \sin 2\alpha_{mi} \cos \beta_{mi}) = 0 \tag{7.48}$$

$$\sum_{i=1}^{N_m} k_{mi} U_{mi}^2 (9 \cos 2\beta_{mi} - 4 \cos 2\alpha_{mi} \cos 2\beta_{mi} - 5 \cos 4\alpha_{mi} \cos 2\beta_{mi}) = 0 \tag{7.49}$$

$$\sum_{i=1}^{N_m} k_{mi} U_{mi}^2 (9 \sin 2\beta_{mi} - 4 \cos 2\alpha_{mi} \sin 2\beta_{mi} - 5 \cos 4\alpha_{mi} \sin 2\beta_{mi}) = 0 \tag{7.50}$$

From (7.5), (7.6), (7.11) and (7.12), we obtain

$$\frac{dW_{ms}^s(\alpha, \beta, \varepsilon, \mu)}{d\varepsilon} = \frac{1}{2} \sum_{i=1}^{N_m} F_{mi}(u_{mi}) \left(\frac{\partial u_{mi}}{\partial \mu} \frac{d\mu}{d\varepsilon} + \frac{\partial u_{mi}}{\partial \varepsilon} \right)$$

$$
\begin{aligned}
&= \frac{1}{2}\sum_{i=1}^{N_m} k_{mi}U_{mi}^2\big[(\sin^2\phi_{mi}\cos^2\phi_{mi} + \lambda_1\sin^4\phi_{mi})\mu + \\
&(\cos^4\phi_{mi} + \lambda_1\sin^2\phi_{mi}\cos^2\phi_{mi})\varepsilon\big] + o(\mu) + o(\varepsilon) \\
&= \frac{1}{2}\sum_{i=1}^{N_m} k_{mi}U_{mi}^2(\cos^2\phi_{mi} + \lambda_1\sin^2\phi_{mi})^2\varepsilon + o(\varepsilon) \\
&= \frac{1}{16}\sum_{i=1}^{N_m} k_{mi}U_{mi}^2\big[3\lambda_1^2 + 2\lambda_1 + 3 + 4(1-\lambda_1^2)\cos 2\phi_{mi} + \\
&\qquad (\lambda_1 - 1)^2\cos 4\phi_{mi}\big]\varepsilon + o(\varepsilon) \qquad (7.51)
\end{aligned}
$$

The MSD model should have the same stiffness in different directions, thus $4(1+\lambda_1)\cos 2\phi_{mi} + (1-\lambda_1)\cos 4\phi_{mi}$ should be same for different values of α and β. From (E.2-E.12), (E.14-E.20) and (E.34-E.39), we have two additional independent constraints.

$$\sum_{i=1}^{N_m} k_{mi}U_{mi}^2(38\sin 2\alpha_{mi}\sin\beta_{mi} + 5\sin 4\alpha_{mi}\sin\beta_{mi}) = 0 \qquad (7.52)$$

$$\sum_{i=1}^{N_m} k_{mi}U_{mi}^2(38\sin 2\alpha_{mi}\cos\beta_{mi} + 5\sin 4\alpha_{mi}\cos\beta_{mi}) = 0 \qquad (7.53)$$

From (7.22–7.23), (7.51) and (7.52-7.53), we obtain

$$
\begin{aligned}
\frac{dW_{ms}^s(\alpha,\beta,\varepsilon,\mu)}{d\varepsilon} &= \frac{1}{16}\sum_{i=1}^{N_m} k_{mi}U_{mi}^2\Big[3\lambda_1^2 + 2\lambda_1 + 3 + (1-\lambda_1^2)(\cos 2\alpha_{mi} - 1) + \\
&\qquad \frac{(\lambda_1-1)^2}{64}(9\cos 4\alpha_{mi} - 4\cos 2\alpha_{mi} - 5)\Big]\varepsilon + o(\varepsilon) \\
&= \frac{1}{30}(8\lambda_1^2 + 4\lambda_1 + 3)\sum_{i=1}^{N_m} k_{mi}U_{mi}^2\varepsilon + o(\varepsilon) \\
&= \frac{1}{12}\sum_{i=1}^{N_m} k_{mi}U_{mi}^2\varepsilon + o(\varepsilon) \qquad (7.54)
\end{aligned}
$$

Assume a real object is stretched evenly by a strain of ε in the direction of unit vector $\vec{n}$ and the material is isotropic. Then the elastic energy for a region of volume V is

$$W_r(\varepsilon) = \frac{EV\varepsilon^2}{2} \qquad (7.55)$$

where the subscript r is used to indicate the real object.

According to (7.55), the stretching elastic energy of the object in the influence volume of node m is

$$W^s_{mr} = \frac{EV_m\varepsilon^2}{2} = \frac{1}{8}E\varepsilon^2\sum_{i=0}^{t_m} V_{mi} = \frac{1}{2}S_m\varepsilon^2 \tag{7.56}$$

where V_m is the influence volume of node m, V_{mi} is the area of the ith tetrahedron incident to it, t_m is the number of tetrahedra incident to it and

$$S_m = EV_m = \frac{E}{4}\sum_{i=1}^{t_m} V_{mi} \tag{7.57}$$

Thus

$$\frac{dW^s_{mr}}{d\varepsilon} = S_m\varepsilon \tag{7.58}$$

For the MSD model to be physically accurate, the energy increment for the springs in the MSD system should be the same as the stretching elastic energy of the object under the same strain. Then, the stretching resistance of the MSD model associated with the influence volume of node m should also be the same as that of the real object in that volume. From (7.54) and (7.57), we have

$$\frac{1}{12}\sum_{i=1}^{N_m} k_{mi}U^2_{mi} = S_m \tag{7.59}$$

In addition, the Hooke's constants must be nonnegative for the stability of the model and not too large for fast evolving of the model, i.e.

$$0 \le k_{mi} \le M \tag{7.60}$$

7.2.2 Solving the Spring Constants

In the previous section, we derived eighteen constraints on the Hooke's constant of the springs incident to each node, among which (7.32–7.40) and (7.45–7.50) constrain the

MSD to have regular Poisson effects, (7.52–7.53) constrain the model to have the same characteristics in different directions and (7.59) constrains the MSD model to have the desired stiffness. Besides, the Hooke's constants must be nonnegative for the stability of the dynamic system.

Generally, we will have more constraints than the number of springs. So those constraints will not be met exactly and thus the MSD model will not have the exact stiffness and Poisson effect as the theoretical result. Here we solve this over-determined optimization problem under hard constraint (7.60) by the constrained least square optimization method.

7.3 3D Structured MSD Model Parameter Optimization

The 3D structured MSD model is often constructed on the cubic meshes. Let the height of the cube be h. For simplicity, assume the cubic mesh is aligned with the Cartesian coordinate system x-y-z (7.2).

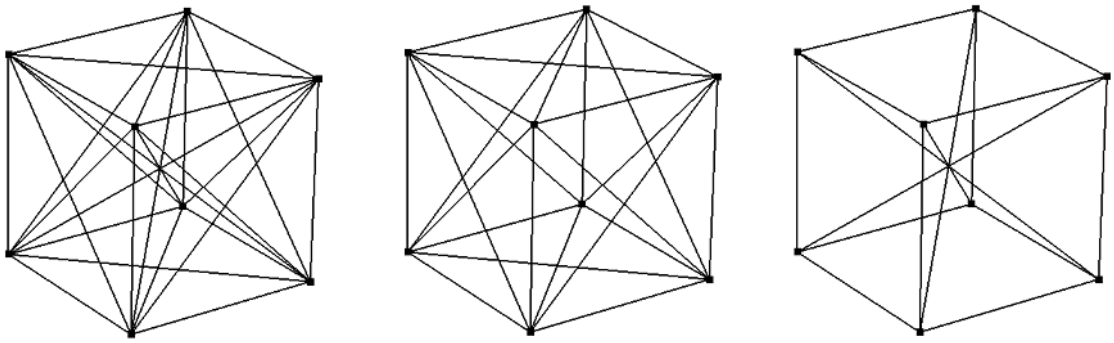

Figure 7.2. Springs on the cubic mesh of the three types of structured MSD model.

Nodes on the same cube are connected by springs along the edges, along the diagonals of the six surfaces and along the center diagonals. Then each node that is not on the boundary has 6 edge springs, 12 surface diagonal springs and 8 center diagonal springs.

Let the Hooke's constants of the springs along the x-axis, y-axis and z-axis be k_1. Let the Hooke's constants of the springs along the main and auxiliary surface diagonal be k_2. Let the Hooke's constants of the center diagonal springs be k_3. Then according to Fig. 7.2 left We can obtain the angles between the springs emanating from each node and the positive z-axis and the angles between the projections of the springs on the x-y plane and the positive x-axis below.

$$\begin{aligned}\alpha_{px} = \alpha_{nx} = \alpha_{py} = \alpha_{ny} = \alpha_{pxpy} = \alpha_{pxny} = \alpha_{nxny} = \alpha_{nxpy} = \beta_{py} = -\beta_{ny} \\ = \beta_{pypz} = \beta_{pynz} = -\beta_{nypz} = -\beta_{nynz} = \frac{\pi}{2}\end{aligned} \tag{7.61}$$

$$\alpha_{pz} = \beta_{px} = \beta_{pz} = \beta_{nz} = \beta_{pxpz} = \beta_{pxnz} = 0 \tag{7.62}$$

$$\begin{aligned}\beta_{pxpy} = \beta_{pxpypz} = \beta_{pxpynz} = -\beta_{pxny} = -\beta_{pxnypz} = -\beta_{pxnynz} = \alpha_{pypz} \\ = \alpha_{nypz} = \alpha_{pxpz} = \alpha_{nxpz} = \frac{\pi}{4}\end{aligned} \tag{7.63}$$

$$\beta_{nxpy} = \beta_{nxpypz} = \beta_{nxpynz} = \alpha_{pynz} = \alpha_{nynz} = \alpha_{pxnz} = \alpha_{nxnz} = \frac{3\pi}{4} \tag{7.64}$$

$$\beta_{nx} = \beta_{nxpz} = \beta_{nxnz} = \alpha_{nz} = \pi \tag{7.65}$$

$$\alpha_{pxpypz} = \alpha_{nxpypz} = \alpha_{nxnypz} = \alpha_{pxnypz} = \arctan\sqrt{2} \tag{7.66}$$

$$\alpha_{pxpynz} = \alpha_{nxpynz} = \alpha_{nxnynz} = \alpha_{pxnynz} = \pi - \arctan\sqrt{2} \tag{7.67}$$

$$\beta_{nxny} = \beta_{nxnypz} = \beta_{nxnynz} = \frac{5\pi}{4} \tag{7.68}$$

where the subscript px (or py or pz) indicates the springs pointing to the positive x-axis (or y-axis or z-axis) direction; the subscript nx (or ny or nz) indicates the springs pointing to the negative x-axis (or y-axis or z-axis) direction; the subscripts $pxpy$, $nxpy$, $pxny$ and $nxny$, (or $pypz$, $nypz$, $pynz$ and $nynz$ or $pxpz$, $nxpz$, $pxnz$ and $nxnz$) indicate the diagonal springs on the surfaces parallel to the x-y (or y-z or x-z) plane; the subscript $pxpypz$ (or $pxpynz$) denotes the center diagonal springs pointing upper (or lower) northeast; the subscript $pxnypz$ (or $pxnynz$) denotes the center diagonal springs pointing upper (or lower) southeast; the subscript $nxnypz$ (or $nxnynz$) denotes the center diag-

onal springs pointing upper (or lower) southwest and the subscript $nxpypz$ (or $nxpynz$) denotes the center diagonal springs pointing upper (or lower) northwest.

Applying constraints (7.32–7.40), (7.45–7.50) and (7.52–7.53), interestingly, we obtain only one constraint on the Hooke's constants of the springs.

$$3k_1 - 3k_2 - 8k_3 = 0 \tag{7.69}$$

And from (7.59), we have

$$k_1 + 4k_2 + 4k_3 = 4Eh \tag{7.70}$$

Totally, there are only two constraints (7.69) and (7.70) on the Hooke's constants of the three types of springs. Thus we can get rid of one type of springs to reduce computation without significantly influencing the behavior of the MSD model. Note that edge springs have to be used because the Hooke's constants have to be positive for the stability of the model.

If we choose not to use the diagonal springs of the cube (Fig. 7.2 middle), i.e. $k_3 = 0$, we have

$$k_1 = k_2 = \frac{4Eh}{5} \tag{7.71}$$

If we choose not to use the diagonal springs on the surfaces of the cube (Fig. 7.2 right), i.e. $k_2 = 0$, we have

$$k_1 = \frac{8Eh}{5} \tag{7.72}$$

$$k_3 = \frac{3Eh}{5} \tag{7.73}$$

Equations (7.71–7.73) are valid for the springs that are not on the boundary. For those surface diagonal springs on the boundary, since they are otherwise shared by two adjacent hexahedra, we should use half the spring constants. For those edge springs on the boundary, since they are otherwise shared by four adjacent hexahedra, we should use $i/4$ of the spring constants if they are shared by i hexahedra, where $i = 1, 2, 3$.

7.4 Validation

7.4.1 Simulating an Elastic Cube

First, we experiment with an MSD model of a $10\,\mathrm{cm}\times10\,\mathrm{cm}\times10\,\mathrm{cm}$ cube ($E = 10\,\mathrm{N/cm^2}$) with hexahedral meshes. We stretch and compress the MSD model in the direction of the x-axis, y-axis and then z-axis by a series of displacements. Theoretically, for the real cube under axial stretching [76] we have

$$F = EA\varepsilon = \frac{EA\Delta L}{L} = 1000\Delta L \tag{7.74}$$

where A is the area of the cross section of the cube, ε is the axial strain, L is the original dimension of the cube and ΔL is the elongation.

For the structured MSD model with parameters obtained from (7.71), the Poisson effects in the lateral directions and the applied force are shown in Fig. 7.3. It is clear that the properties of the model are very close to that of the real object, which validates our parameter optimization scheme.

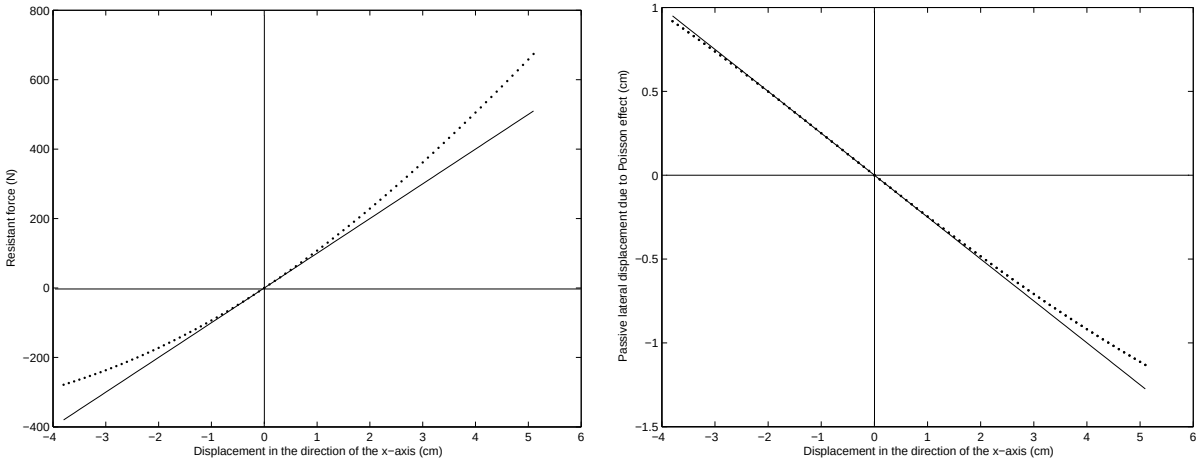

(a) (b)

Figure 7.3. (a) Comparision between the tensile resistance of the structured MSD model (dotted line) and that of the real cube (solid line); (b) comparison between the Poisson effect of the structured MSD model (dotted line) and that of the real cube (solid line).

For the MSD model with parameters obtained from (7.72) and (7.73), usually the model is not robust enough and often collapses. This shows that the constraints we derived are necessary conditions but not sufficient conditions for the physical accuracy of the MSD model.

Second, we simulate the unstructured MSD model with tetrahedral meshes. The Poisson effects in the lateral directions of the model with optimized parameters and the relationship between the applied force and displacement are shown in Fig. 7.4. We can see that the tensile resistance of the model is very close to that of the real cube, while the Poisson effect is not accurately achieved. The Poisson effects are not even the same in two lateral directions. The uneven Poisson effects may cause some artifacts, which is a limitation of the unstructured MSD model.

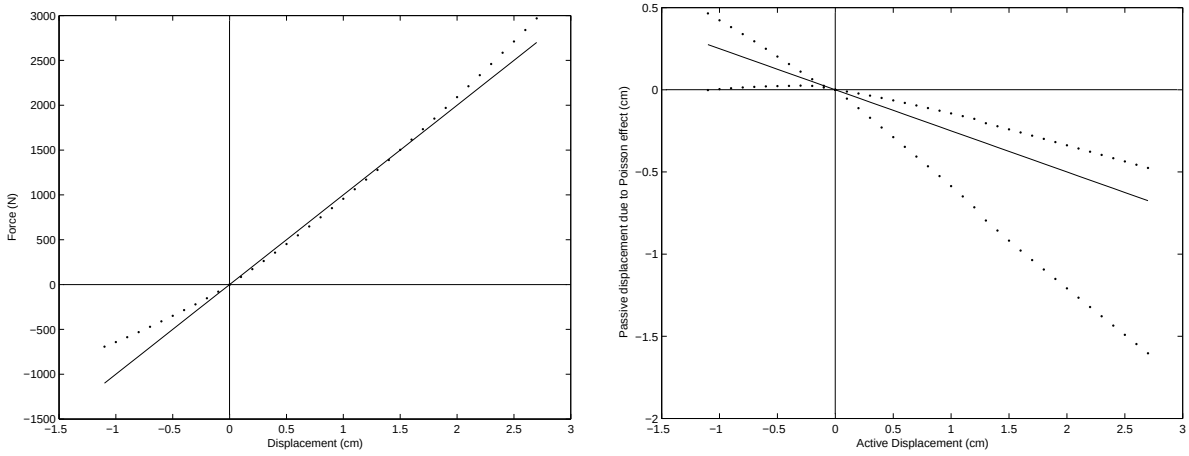

(a) (b)

Figure 7.4. (a) Comparison between the tensile resistance of the unstructured MSD model (dotted) and that of the real cube (solid); (b) comparison between the Poisson effects of the unstructured MSD model (dotted) and those of the real cube (solid).

7.4.2 Simulation of a Circular Shaft

First, we simulate a circular shaft of radius 5 cm and length 15 cm. Theoretically, for the real shaft under axial stretching [76] we have

$$F = E\pi R^2 \varepsilon = \frac{\pi E R^2 \Delta L}{L} = 523.6\Delta L \tag{7.75}$$

For the unstructured MSD model of the shaft with tetrahedral meshes, the tensile resistance against displacement and the Poisson effects in the lateral directions are shown in Fig. 7.5.

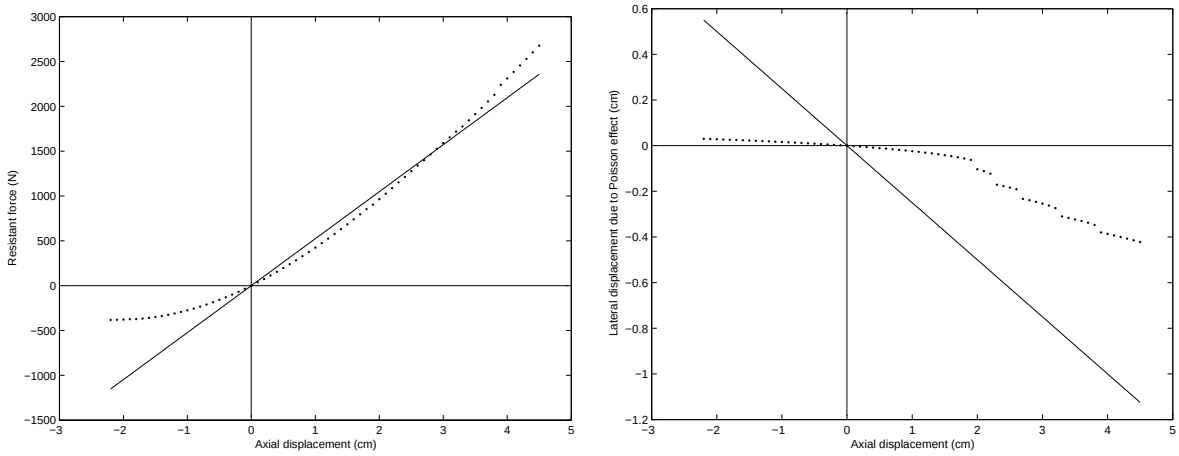

(a) (b)

Figure 7.5. Comparison between the tensile resistance and the Poisson effect of the unstructured MSD model of a circular shaft (dotted line) and those of the real shaft (solid line).

Second, we experiment with twisting the unstructured MSD model of the shaft. Theoretically, for a circular shaft of radius R subjected to a twisting moment (torque) M_z at the free end and restrained against both displacement and rotation at the other end, if we assume the angle of rotation per unit length (the rate of twist) to be α, then

$$M_z = \frac{G\alpha\pi R^4}{2} = G\alpha J_c \tag{7.76}$$

where $J_c = \pi R^4/2$ is called the polar moment of inertia and $G = E/2(1+\nu)$ is called the shear modulus.

The comparison of the resistance torque against the rate of twist is shown in Fig. 7.6, from which we can see that the characteristics of torsion of the optimized unstructured MSD model is very close to that of the real shaft, which validates our parameter optimization scheme.

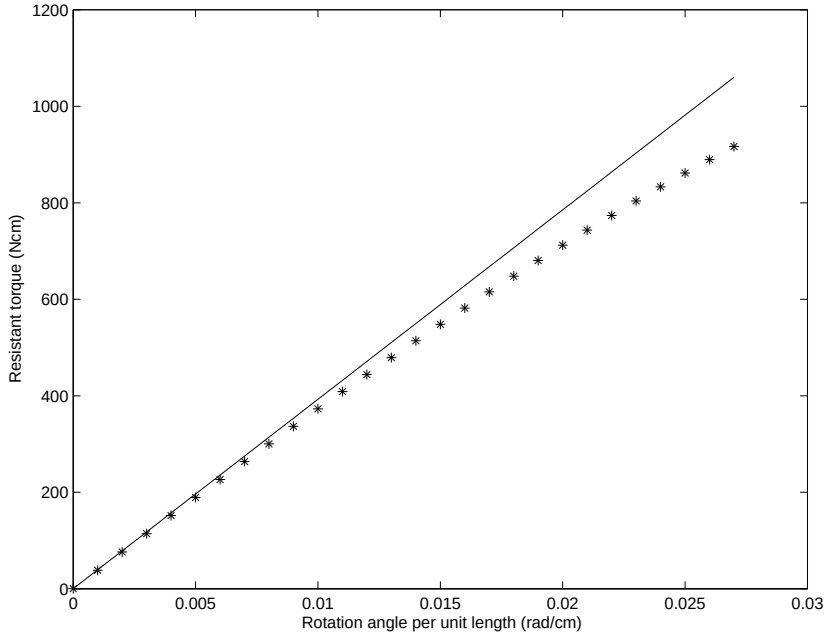

Figure 7.6. Comparison between the resistant torque for rotating the MSD model (dotted) and a real shaft (solid).

7.5 Conclusion

The parameter optimization method proposed in this chapter is shown to be able to achieve very accurate deformations for 3D structured MSD models. While the unstructured MSD model has the advantage of being able to fit into irregular shaped objects, it cannot achieve the same accuracy as the structured models for specific mesh struc-

tures. Further research needs to be done to optimize the mesh structure and the Hooke's constants together to achieve better accuracy for the unstructured MSD model.

CHAPTER 8

Hernia Surgery Simulator

8.1 What Is Hernia?

Hernia refers to the protrusion of an organ through a weak area in the muscles or tissue that surround and contain it. Most commonly, the word hernia is used to refer to an abdominal hernia because most hernias occur in the abdomen. The abdominal wall, which is a sheet of tough muscle and tendon that runs down from the ribs to the legs at the groins, acts as "nature's corset". Its function, amongst other things, is to hold in the abdominal contents, principally the intestines. If a weakness should open up in that wall, then the "corset effect" is lost and what pushes against it from the inside (the intestines) simply pushes through the "window". The ensuing bulge, which is often quite visible against the skin, is the hernia [84]. The development of a general hernia condition is shown Fig. 8.1. Hernia can give rise to discomfort as it enlarges and can sometimes be dangerous if a piece of intestine becomes trapped (strangulted) inside.

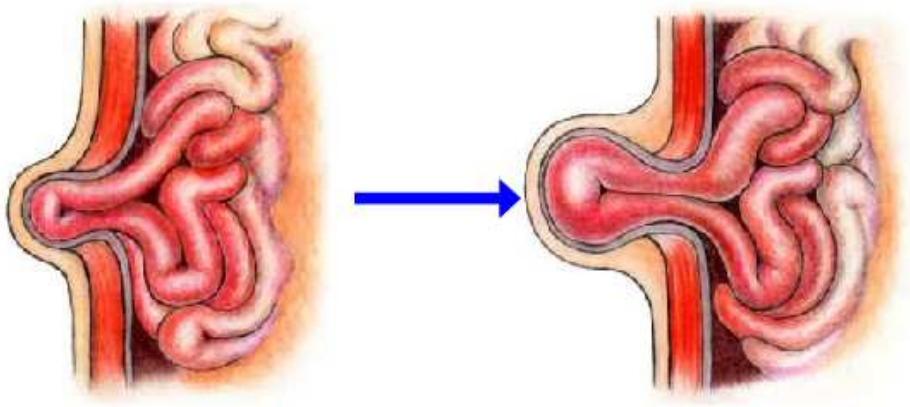

Figure 8.1. The development of a general hernia condition [4].

The “windows of weakness” commonly occurs where there are natural weaknesses in our abdominal wall, such as where the “plumbing” goes through it [84]. Examples of these are the canals (inguinal and femoral) which allow passage of vessels down to the scrotum and the legs, respectively. The umbilical area (navel) is another area of natural weakness frequently prone to hernia. Another area of potential weakness can be the site of any previous abdominal surgery.

The most common location for hernias is the groin area as shown in Fig. 8.2, which accounts for 80% of all hernias [4]. There are several reasons for this tendency. First, there is a natural anatomical weakness in groin region, which results from incomplete muscle coverage. Second, the upright position of human posture results in a greater force at the bottom of the abdomen, thereby increasing the stress on these weaker tissues. The combination of these factors over time breaks down the support tissues enlarging any pre-existing hole, or leading to a tear, resulting in a new hole. Several different types of hernia may occur, and frequently coexist, in the groin area. These include indirect inguinal hernia, direct inguinal hernia and femoral hernia, which are defined by the location of the opening of the hernia from the abdomen to the groin.

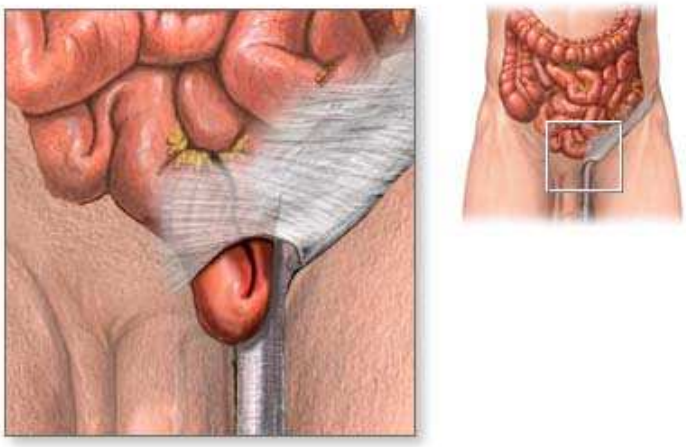

Figure 8.2. Intestine passes through into scrotum or groin [4].

An indirect hernia follows the pathway that the testicles made during pre-birth development. It descends from the abdomen into the scrotum through a weak spot in the inguinal canal, which is a triangle-shaped opening between layers of abdominal muscle near the groin. The direct inguinal hernia occurs slightly to the inside of the site of the indirect hernia, in a place where the abdominal wall is naturally slightly thinner. It rarely will protrude into the scrotum.

The femoral canal is the way that the femoral artery, vein, and nerve leave the abdominal cavity to enter the thigh. Although normally a tight space, sometimes it becomes large enough to allow abdominal contents (usually intestine) into the canal. A femoral hernia causes a bulge below the inguinal crease in roughly the middle of the thigh. Femoral hernias are particularly at risk of becoming irreducible and strangulated.

According to the sites and causes of formation, the other types of hernia over the abdomen area are epigastric, lumbar, umbilical, obturator, stoma, internal, incisional and spigelian hernias as shown in Fig. 8.3. With the exception of internal hernias (within the abdomen), these hernias are commonly recognized as a lump or swelling and are often associated with pain or discomfort at the site. Internal hernias can be extremely difficult to diagnose until the intestine has become trapped and obstructed.

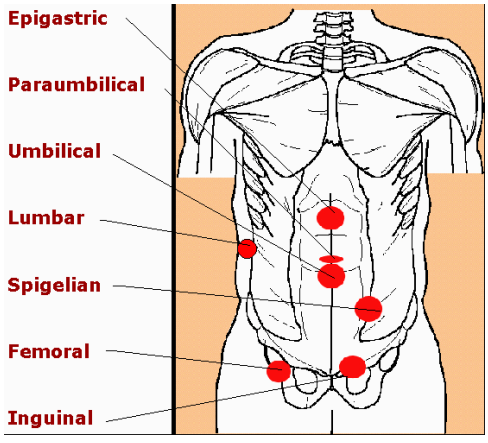

Figure 8.3. Hernias at different sites [4].

Hernia can also happen in the chest area, which is called hiatus hernia [84] and affects the digestive system. Where the oesophagus goes down, it passes the diaphragm through a gap called the hiatus. Immediately below that, it goes into the stomach which sits just below the diaphragm. This hiatus causes a narrowing of the opening into the stomach and this helps prevent stomach contents from going the wrong way, i.e. upwards, which is called reflux. If the area of the hiatus is weak, the function of "clamping down" on the entry to the stomach is weakened, the result being the reflux of acidic digestive juices up into the oesophagus, which is not protected against the action of these acids. The outcome of this is often a quite painful burning sensation.

8.2 Hernia Surgery

Nowadays, there are generally two types of treatments for hernias—the traditional open hernia repair and the laparoscopy technique. Some hernia in the elderly do not require surgery, and can either be left alone or treated with a truss. A truss is a surgical appliance which helps to keep the hernia under control.

8.2.1 The Traditional Hernia Repair

The traditional and still widely used method of hernia repair is to admit the patient to hospital, whether as a day-case or for a few days, and under general anaesthesia, the surgeon would push back the bulge of peritoneum through the opening and then close the defect by stitching one side firmly to the other, as shown in Fig. 8.4. Because the patient depends upon this stitching for the rest of his life to hold the abdominal wall closed, the surgeon will normally have to place several stitches, under a degree of tension in the deep tissue, repeating the process until he is satisfied that the join will hold.

Unfortunately, this stitching distorts sensitive tissue. This will cause tension and subsequent pain with all movements (including coughing and sneezing). The patient can

expect to feel the results of the stitching long after he leaves hospital. He is therefore restricted in physical activity for some weeks.

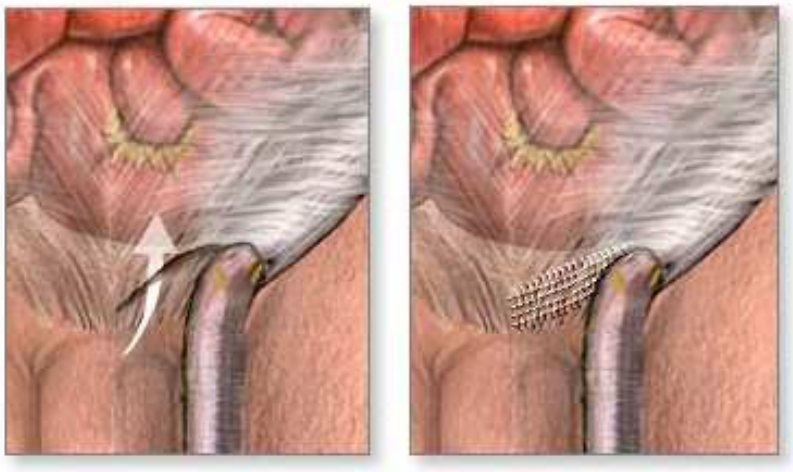

Figure 8.4. Left: bulging tissue is replaced inside the muscle wall; right: muscle tissue is repaired [4].

A further problem of this technique of hernia repair is that a significant number of cases (up to 10 percent or more) will recur by virtue of the internal scar tissue becoming pulled out at some time in the patient's life. The repair of this recurrent hernia is therefore a larger operation than the first and the result is proportionately more uncomfortable. In order to reduce the tension of the stitching, surgeons developed methods of stitching the tissue in layers. This technique reduced a little of the pressure, but resulted in more stitching through the patient's tissue. Later techniques include placing or stitching a "patch" over the hernia.

8.2.2 Laparoscopic Hernia Surgery

Another method is the laparoscopy technique in which the surgeon inserts small tubes into the abdominal cavity. Through one of these tubes (called trocars), he inserts

a video camera, and using other tubes to insert surgical instruments, and operates while monitoring at the image on a television monitor. In a laparoscopic hernia repair procedure, the surgeon first pulls the hernial sac back into the abdominal cavity, exposing the defect in the abdominal wall as shown in Fig. 8.5(a). Then this weakened portion is covered with a mesh patch, which is shown in Fig. 8.5(b). Laparoscopy allows the surgeon to place and staple the patch on the inside of the abdominal wall, taking advantage of the natural outward pressure of the abdomen to secure the repair and promote healing. This technique is performed under general/spinal anaesthesia. This approach is technically much more difficult for surgeons to perform successfully than other techniques.

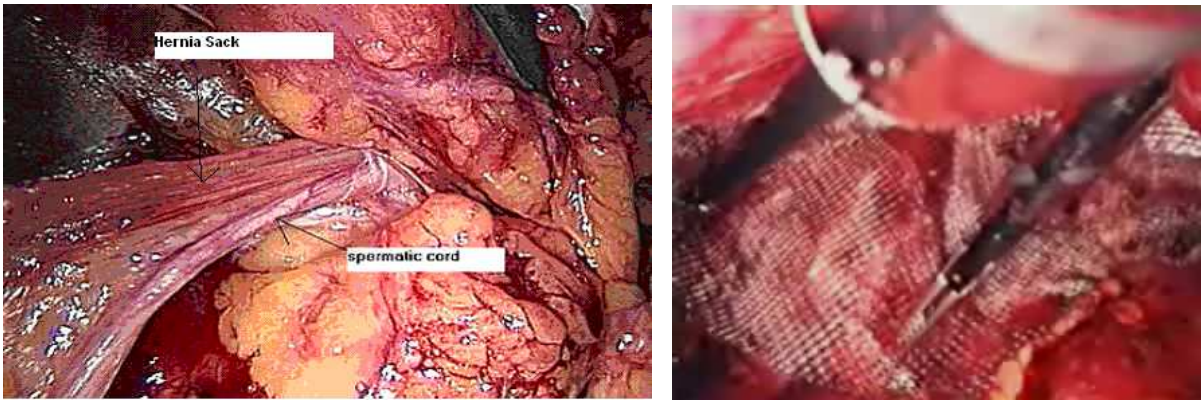

(a) (b)

Figure 8.5. (a) Real inguinal hernia view on the monitor [5]; (b) real mesh placement procedure [6].

The advantage of this technique from the patients's point of view is that only the smallest incisions are required (so-called keyhole surgery). In order that the surgeon may manoeuvre inside the patient and see what he is doing, the patient's abdomen has to be pumped up with compressed carbon dioxide gas. Because the surgeon works 'remotely' with these instruments and guided only by what he sees on a TV screen, he has less control than otherwise, particularly with difficult or complex cases. There are many

reports of serious accidents to neighboring organs [12, 85]. Thus, laparoscopy requires extensive and specialized training. As mentioned in chapter one, virtual reality based surgical simulation fulfills this need.

8.2.2.1 Details of Herniorrhaphy

The external appearance of a groin hernia corresponds to a sac of peritoneum, filled with omentum or intestine, which extends through a hole in the abdominal wall fascia. As mentioned before, there are three types of groin hernias–indirect, direct and femoral hernia. All three types of groin hernia are treated with the same laparoscopic technique of patching the inguinal floor from the inside. The procedure involves inserting a laparoscope through the umbilicus and distending the peritoneal cavity to a pressure of 15 mmHg. Groin defects are then seen with remarkable clarity. Two additional trocars are passed through the lateral abdominal wall to the right and left of the midline. Three ports are generally required, one for visualization, and two ports for instruments operated by the surgeon's right and left hands.

The important landmarks for hernia repair glisten through the peritoneum near the visible hernia defect. From within the peritoneum laparoscopic instruments are used, first the scissors to open the peritoneum near the hernia defect. Blunt dissection is performed to expose the strong fascial layers that will hold the staples and act as points of fixation for the mesh. Cautery may be necessary but the dissection is virtually bloodless in most cases. The preperitoneal space opening allows placement for the sheet of soft polypropylene mesh to overlay the defect without buckling or curling, which may predispose to early recurrence.

The mesh is a great deal larger than the groin defect and permits overlap onto strong fascial surfaces providing greater strength and allowing for tissue ingrowth. Ten to fifteen staples are placed to hold the mesh. The peritoneum is closed laparoscopically

over the mesh to prevent visceral adhesions to the repair. The trocars are removed and the abdominal wall incisions are closed.

The procedure takes as little as thirty minutes and bilateral hernias can be done with the same trocar-port exposure. The procedure is usually planned as an outpatient operation; postoperative stay is usually measured in hours as the patient recovers from general anesthesia.

The anatomy of the inguino-femoral region viewed via a telescope placed in intra-abdominal position differs radically from the anatomy observed via an open or anterior approach. The laparoscopic surgeon needs to become familiar with the anatomical structure of this region. As all anatomical landmarks are covered with peritoneum, they need to be meticulously exposed with blunt dissection or by incising the peritoneum and develop a lower flap. For the performance of a safe and secure laparoscopic inguinal hernia repair, the following structures should be clearly and unequivocally identified: cooper's ligament, epigastric vessels, the spermatic cord (or the round ligament), the femoral canal and the iliac vessels. The inguinal hernia anatomy is shown in Fig. 8.6.

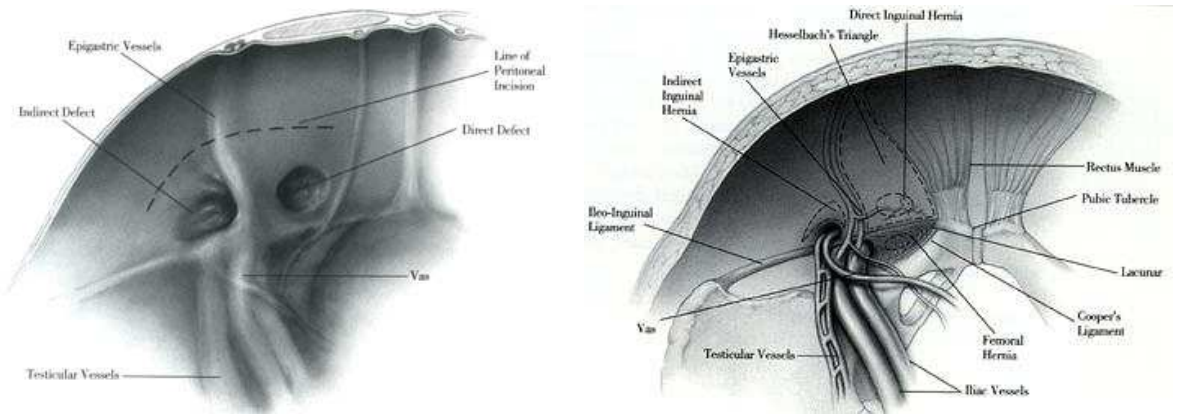

(a) (b)

Figure 8.6. (a) Inguinal hernia anatomy with peritoneal coverage; (b) inguinal hernia anatomy without peritoneal coverage [7].

Other tissues involved in an inguinal hernia repair are transversus abdominis, rectus abdominis, psoas muscle, lliacus muscle, lliopsoas muscle, pubic bone, pubic symphysis, vas deferens, spermatic vessels, inferior epigastric artery, lliac vessels and lliopubic tract.

8.3 Laparoscopic Hernia Surgery Simulator

Since the groin hernia is the most common and laparoscopy technique has been widely used for it, a simulator for it is being developed at the Virtual Environment Lab (VEL) at UT-Arlington in collaboration with UT-Southwestern Medical Center [13, 50, 86–91].A successful inguinal hernia surgery simulator should help surgeons get familiar with the anatomy and practice the skills of manipulating the instrument to expose the hernia site, puting back the hernia sack and placing the plastic mesh.

8.3.1 Hardware

The hardware required for a surgery simulator is a PC with an enhanced high-end graphics card, a Phantom interface device and a supporting framework as shown in Fig. 8.7.

Figure 8.7. Laparoscopic hernia surgery simulator [8].

8.3.2 Software Modules

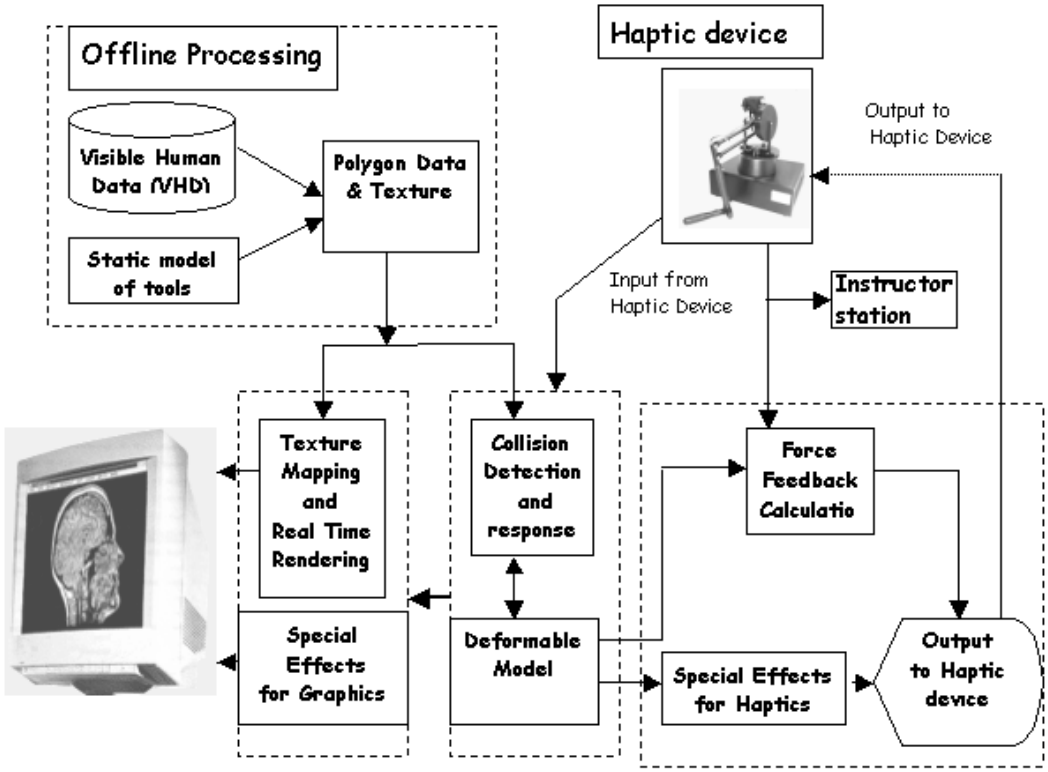

Figure 8.8. Control flow for laparoscopic hernia surgery simulator.

The system architecture for the laparoscopic hernia surgery simulator under construction by a team of VEL researchers is shown in Fig. 8.8. It contains all the modules that are necessary for the surgical simulation system for any surgery procedure. Each organ involved needs to be rendered both geometrically for graphics display and physically for force feedback (haptics). For graphics display, it is necessary to build geometry models for the organs. Although the organs are patient specific, i.e. the same organ for different people varies in size and shape, the result will be more convincing if we can reconstruct the organs according to a real person. Thanks to the Visible Human Project of

National Library of Medicine [9], we can extract surface triangles according to its visible human data (VHD). VHD is a set of digitally photographed axial sections of a man and a woman respectively. As an example, we show one slice of VHD in Fig. 8.9. For the photograph of each slice, experts at Gold Standard Media Inc. segmented it for different organs and formed segmented data, which is a set of gray pictures with the label number of the organ as its intensity. Based on the segmented data, we can reconstruct any organ in 3D in which we have interest by using the marching cubes algorithm [92], which is an algorithm to extract isosurfaces from volumetric data. Since the geometry models are only used once for initiation, it can be constructed by an off-line process.

Figure 8.9. One slice of the VHD for a male [9].

For haptics rendering, the organ needs to be physically driven, i.e. an physical model is needed to support the deformation of the organ and provide the force feedback. This module has to run in real-time to meet the requirement of the graphics update rate (30 Hz) and haptics update rate (1000 Hz).

During simulation, the instrument interacts with the virtual organs and the virtual organs also interact with each other. Real time algorithms are needed to handle these interactions, otherwise, the instrument will penetrate the virtual organs without resistance and also the virtual organs themselves. To prevent penetration, it is necessary to provide mechanisms to locate the intersection between them (so-called collision detection) and then apply appropriate force between them (so-called collision response) to prevent large penetrations.

For realistic graphics rendering, we intend to apply the texture mapping technique to enhance the visual effects. By using a graphics card, texture mapping can be used in a scene without much influence on the computation time. In our hernia surgery simulation project, it is desired that we use real texture of the organs. The texture information are extracted from VHD [8] or synthesized from videos of real surgeries.

In a hernia surgery, surgeons are mindful of the area between the spermatic vessels and the vas deferens in proximal to iliac vessels called the "triangle of doom". Complications like damage to the spermatic cord, nerves and blood vessels may occur within the triangle. Since laparoscopic herniorrhaphy requires a longer learning curve for the surgeon than for more conventional repairs, we provide realistic bleeding simulation during virtual laparoscopic herniorrhaphy to train residents to avoid entering the triangle, or properly handle this accident in case it happens. To achieve this goal, we simulate the bleeding [93], cauterization and irrigation procedure [94]. All these are called special effects.

8.3.3 Challenges

The most challenging module is the deformable model part, which is the core algorithm for the surgical simulation system and the subject of this dissertation. The models mentioned in chapter 2 have two common drawbacks. First, none of them preserve

volume, which is a very important property for soft tissues [52]. For all the models, their volume will be smaller if they are compressed in one direction and be larger if they are stretched. For models based on elasticity, the strain coupling effect is modeled by Poisson constant ν. Usually for isotropic materials, $\nu \approx 0.3$. For plastic materials such as rubber, $\nu \approx 0.5$, which can ensure volume preservation for small deformation but not for large deformation. While for the human organ, volume change probably means damage to the organ. The second drawback is that the stresses in mutually perpendicular directions are almost independent. For models based on elasticity, the stress coupling coefficient is ν, much smaller than 1, while the real organ should have deeply-coupled stress in different directions. As discussed in chapter 2, the models based on elasticity theory can achieve accurate results. But they are accurate under the assumption of small deformation which is usually not valid in a real surgery [95]. And current elasticity theory also assumes linear properties of the material, while soft tissue display highly nonlinear properties. These gaps between theory and practice also limit the accuracy of the simulation. Based on the current problems with deformable models, we have presented a new deformable model in chapter 3, which views the organ as a combination of a honeycomb fabric structure and incompressible fluid filled inside. This model can ensure volume preservation for large deformation and can model high stress coupling coefficient up to 1.

As the honeycomb model was developed and implemented, it turned out that this model is too slow to fit into real-time applications for the current CPU capacity. Therefore, in parallel, we also worked on improving the MSD model, which has the most potential for real-time applications. In laparoscopic hernia surgery, the core part is to lay a sheet of soft polypropylene mesh over the hernia defect without buckling or curling and place ten to fifteen staples to hold the mesh in place on the tissue. The mesh is simulated using a MSD model, which tends to be too soft and this defect cannot be fixed effectively by simply increasing the stiffness of the springs. Our work in chapter 4–6

analyzed the reason behind this phenomenon. As a result, the idea of using preload is proposed to accurately model the bending resistance. By applying the parameter optimization scheme we proposed, the realism of the mesh simulation is greatly improved. Then, we extended the parameter optimization techniques to a general 3D MSD model of an isotropic object.

CHAPTER 9

Conclusion and Future Work

This chapter concludes the dissertation. We will first provide a summary of the main results/constributions of this thesis and then describe possible future research as a result of this work.

9.1 Conclusion

There are two main contributions of this thesis. First, a honeycomb model based on the constitutive elements of the human organ and its volume preservation property is proposed, which has potential to be more accurate than other models, although it has too heavy computation to be suitable for real time applications at present. Second, the parameter optimization schemes for the physical accuracy of the 1D, 2D and 3D MSD models with both structured and unstructured meshes are proposed, developed and validated in detail with simulation. Previously, the application of the MSD model was limited to the structured MSD models. Our work makes it practical to apply the unstructured MSD models in case the real object does not have a regular shape. For 1D and 2D MSD models, our investigation finds the intrinsic defect with the traditional MSD models and extends the traditional models to more general models with preload. For the 3D structured MSD model, the proposed parameter optimization scheme can completely resolve the coupling effect between tensile resistance modeling and shear resistance modeling, which results in accurate modeling of both.

9.2 Future Work

For deformable modeling, based on the current computer resource, we would still recommend the use of MSD model for the human organs for the application of surgical simulation. To truly exploit the potential of the MSD model with respect to physical accuracy, the current parameter optimization scheme needs to be extended to anisotropic materials and then incorporated with in vivo tissue properties.

For unstructured MSD models, we have shown in chapter 6 and chapter 7 that high accuracy is not achievable for a general mesh structure. We would expect that some mesh structures would be able to achieve better physical accuracy than others. While the boundary nodes of the mesh structure have to fit into the irregular shape of the real object, it is possible to move the internal nodes to form an optimal mesh structure which is able to achieve the optimal accuracy. Therefore, further research can be done to optimize the mesh and parameters of the model together to enhance the physical accuracy of the model.

Deformable models have to support the adaptive refinement scheme to fully exploit the computer resources for real time applications. Previous work on adaptive refinement of the MSD model is limited to geometric refinement/simplification. Further research needs to be done based on our parameter optimization methods to find the optimal parameter re-assignation after geometric refinement/simplification so that the properties of the model do not have significant changes in the sense of visual effect and physical accuracy after the refinement/simplification.

APPENDIX A

The MSD Model of a Beam under a Lateral Central Load

In this appendix, we will investigate the MSD model of a beam under a lateral central load.

A.1 The MSD model of a beam under a lateral central load

Refer to Fig. 5.1, assume the lateral displacement of node V_k to be d_k ($-1 \leq k \leq n$). For node V_k that is not at the end or center ($0 < k < n-1$), the resultant internal force on the mass from the springs should be zero. By considering the equilibrium condition of the mass in the lateral direction, when the lateral displacements of the nodes are small compared to U, we have

$$P_1 \frac{d_{k+1} + d_{k-1} - 2d_k}{U} + P_2 \frac{d_{k+2} + d_{k-2} - 2d_k}{2U} = 0 \tag{A.1}$$

According to (5.19) and (5.20), we have $P_1/P_2 = -2$. Then from (A.1), we get

$$d_{k+2} = 4d_{k+1} - 6d_k + 4d_{k-1} - d_{k-2} \ (0 < k < n-1) \tag{A.2}$$

The characteristic equation is $r^4 - 4r^3 + 6r^2 - 4r + 1 = 0$. Its only solution is r=1. So

$$d_k = C_1 + C_2 k + C_3 k^2 + C_4 k^3 \tag{A.3}$$

From (A.2), we have $d_3 = 4d_2 - 6d_1$, $d_4 = 10d_2 - 20d_1$, $d_5 = 20d_2 - 45d_1$, $d_6 = 35d_2 - 84d_1$. According to (A.3), we have

$$\begin{bmatrix} 1 & 3 & 9 & 27 \\ 1 & 4 & 16 & 64 \\ 1 & 5 & 25 & 125 \\ 1 & 6 & 36 & 216 \end{bmatrix} \begin{bmatrix} C_1 \\ C_2 \\ C_3 \\ C_4 \end{bmatrix} = \begin{bmatrix} 4d_2 - 6d_1 \\ 10d_2 - 20d_1 \\ 20d_2 - 45d_1 \\ 35d_2 - 84d_1 \end{bmatrix} \tag{A.4}$$

We can obtain

$$\begin{bmatrix} C_1 \\ C_2 \\ C_3 \\ C_4 \end{bmatrix} = \begin{bmatrix} 0 \\ d_1 - \frac{d_2}{6} \\ \frac{d_1}{2} \\ \frac{d_2}{6} - \frac{d_1}{2} \end{bmatrix} \tag{A.5}$$

From (A.3), we obtain

$$d_k = \big(d_1 - \frac{d_2}{6}\big)k + \frac{d_1}{2}k^2 + \big(\frac{d_2}{6} - \frac{d_1}{2}\big)k^3 \quad (2 < k \leq n) \tag{A.6}$$

At node V_{n-1}, by considering the equilibrium condition of the mass in the lateral direction, we have

$$P_1 \frac{d_n + d_{n-2} - 2d_{n-1}}{U} + P_2 \frac{d_{n-3} - d_{n-1}}{2U} = 0 \tag{A.7}$$

Since $P_1/P_2 = -2$, we have

$$-4d_n + 7d_{n-1} - 4d_{n-2} + d_{n-3} = 0 \tag{A.8}$$

According to (A.6) and (A.8), we have

$$-2\big(d_1 - \frac{d_2}{6}\big) + \frac{d_1}{2}(-4n) + \big(\frac{d_2}{6} - \frac{d_1}{2}\big)(-2 - 6n^2) = 0 \tag{A.9}$$

We can get

$$d_2 = \frac{3n^2 - 2n - 1}{n^2} d_1 = (3 - \frac{2n+1}{n^2}) d_1 \tag{A.10}$$

By considering the equilibrium condition at node V_n in the lateral direction, we have

$$F = 2P_2 \frac{d_n - d_{n-2}}{2U} + 2P_1 \frac{d_n - d_{n-1}}{U} \tag{A.11}$$

Then

$$\frac{F}{d_n} = \frac{P_2}{U}\Big(1 - \frac{d_{n-2}}{d_n}\Big) + \frac{2P_1}{U}\Big(1 - \frac{d_{n-1}}{d_n}\Big) \tag{A.12}$$

According to (A.6) and (A.10), we have

$$d_k \;=\; \frac{3n^2 + 2n + 1 + 3n^2 k - (2n+1)k^2}{6n^2} d_1 k \tag{A.13}$$

Thus

$$d_n = \frac{n^3+2n^2+2n+1}{6n}d_1 \tag{A.14}$$

$$d_{n-1} = \frac{n^3+2n^2-n-2}{6n}d_1 \tag{A.15}$$

$$d_{n-2} = \frac{n^4+2n^3-10n^2+n+6}{6n^2}d_1 \tag{A.16}$$

According to (A.12), we have

$$\frac{F}{d_n} = \frac{P_2}{U}\Big(1-\frac{d_{n-2}}{d_n}\Big) - \frac{4P_2}{U}\Big(1-\frac{d_{n-1}}{d_n}\Big) \tag{A.17}$$

Then

$$\frac{F}{d_n} = \frac{P_2}{U}\frac{4d_{n-1}-3d_n-d_{n-2}}{d_n} \tag{A.18}$$

$$\frac{F}{d_n} = -\frac{P_2}{U}\frac{12n+6}{n^4+2n^3+2n^2+n} \tag{A.19}$$

Since

$$P_2 = -\frac{2EI}{U^2} \tag{A.19}$$

Thus

$$\frac{F}{d_n} = \frac{2EI}{U^3}\frac{12n+6}{n^4+2n^3+2n^2+n} \tag{A.19}$$

We have $U = L/2n$ (see section 5.2.3), so

$$\lim_{n\to\infty}\frac{F}{d_n} = \lim_{n\to\infty}\frac{2EI}{L^3}\frac{8n^3(12n+6)}{n^4+2n^3+2n^2+n} = \frac{192EI}{L^3} \tag{A.20}$$

APPENDIX B

Boundary Effect of the 1D MSD Model

In this appendix, we will analyze the boundary effect of the 1D MSD model.

B.1 Boundary effect of the 1D MSD model

Nonzero preload will cause the 1D MSD system to contract due to the imbalance of its two ends. Assume the amount of contraction between node V_{k-1} and V_k due to this boundary effect to be s_k $(k = 0, 1, 2, \cdots, n)$. Refer to Fig. 5.1, at node V_{-1}, we obtain

$$P_1 - k_1 s_0 + P_2 - k_2(s_0 + s_1) = 0 \tag{B.0}$$

At node V_0, we have

$$P_1 - k_1 s_0 = P_1 - k_1 s_1 + P_2 - k_2(s_1 + s_2) \tag{B.0}$$

At node V_k $(k \geq 1)$, we have

$$\begin{aligned} P_1 - k_1 s_k + P_2 - k_2(s_{k-1} + s_k) = P_1 - k_1 s_{k+1} \\ + P_2 - k_2(s_{k+1} + s_{k+2}) \end{aligned} \tag{B.0}$$

When $k_2 = 0$, from (B.1), (B.1) and (B.0) we have

$$P_1 - k_1 s_0 + P_2 = 0 \tag{B.1}$$

$$k_1 s_0 = k_1 s_1 - P_2 \tag{B.2}$$

$$s_k = s_{k+1} \quad (k \geq 1) \tag{B.3}$$

According to (B.1), (B.2), (B.3) and (5.18), we obtain

$$s_0 = \frac{P_1 + P_2}{k_1} \tag{B.4}$$

$$s_k = \frac{P_1 + 2P_2}{k_1} = 0 \quad (k \geq 1) \tag{B.5}$$

We can see that the boundary effect is restricted to only the structural springs and flexion springs connected to the two ends in this case. If the cross section of the beam modeled

is a rectangle of height (depth) h and width b, then $I = Ebh^3/12$. According to (5.19), (5.20) and (5.29), the preloads on the springs are proportional to the cube of the depth h of the beam and the spring constant k_1 is proportional to h. Then the contraction of the boundary spring is proportional to the square of h. Similarly, it is in inverse proportion to the space U between adjacent masses.

When $k_2 \neq 0$, let $k_1/k_2 = c$. Since k_1 and k_2 cannot be negative for the stability of the MSD system, we have $c \geq 0$. From (B.1), we have

$$s_1 = \frac{P_1 + P_2}{k_2} - (1 + c)s_0 \tag{B.5}$$

From (B.0) we have

$$s_{k+2}+(1+c)s_{k+1}-(1+c)s_k-s_{k-1}=0 \ (k \geq 1) \tag{B.6}$$

Then

$$s_3 = s_0 + (1 + c)s_1 - (1 + c)s_2 \tag{B.7}$$

$$s_4 = s_1 + (1 + c)s_2 - (1 + c)s_3 \tag{B.8}$$

$$s_5 = s_2 + (1 + c)s_3 - (1 + c)s_4 \tag{B.9}$$

The corresponding characteristic equation of (B.6) is

$$r^3 + (1 + c)r^2 - (1 + c)r - 1 = 0 \tag{B.9}$$

When $c > 0$, the roots of the equation above are

$$r_1 = 1 \tag{B.10}$$

$$r_2 = \frac{\sqrt{c^2 + 4c} - 2 - c}{2} > -1 \tag{B.11}$$

$$r_3 = \frac{-\sqrt{c^2 + 4c} - 2 - c}{2} < -1 \tag{B.12}$$

Then

$$s_k = C_1 + C_2 r_2^k + C_3 r_3^k \quad (k \geq 3) \tag{B.12}$$

In this situation, the contraction of springs will propagate from the boundary to the whole MSD system. We will show there cannot be three consecutive zero contractions. According to (B.1), we have

$$\begin{bmatrix} 1 & r_2^k & r_3^k \\ 1 & r_2^{k+1} & r_3^{k+1} \\ 1 & r_2^{k+2} & r_3^{k+2} \end{bmatrix} \begin{bmatrix} C_1 \\ C_2 \\ C_3 \end{bmatrix} = \begin{bmatrix} s_k \\ s_{k+1} \\ s_{k+2} \end{bmatrix} \quad (k \geq 3) \tag{B.13}$$

Assume $s_k = 0$, $s_{k+1} = 0$, $s_{k+2} = 0$ $(k \geq 3)$. Since

$$det \begin{bmatrix} 1 & r_2^k & r_3^k \\ 1 & r_2^{k+1} & r_3^{k+1} \\ 1 & r_2^{k+2} & r_3^{k+2} \end{bmatrix} = -(c+4)\sqrt{c^2+4c} \neq 0 \tag{B.14}$$

So $C_1 = C_2 = C_3 = 0$. Then $s_3 = s_4 = s_5 = 0$. From (B.9), we have $s_2 = 0$. Then from (B.8) and (B.7), we have $s_1 = 0$ and $s_0 = 0$, which contradicts (B.1).

When $c = 0$, we have $r_1 = 1, r_2 = r_3 = -1$. Thus

$$s_k = C_1 + (-1)^k C_2 + (-1)^k k C_3 \tag{B.14}$$

We can prove in a similar way that the contraction will propagate all over the 1D MSD system.

APPENDIX C

Axisymmetric Stretching of a Plate

In this appendix, we will analyze the axisymmetric stretching of a plate.

C.1 Axisymmetric stretching of a plate

Consider a circular plate with depth h under the action of circular stretch. We apply force evenly at any points on the circumference of the plate, and then a state of plane stress exists. For convenience, we use the polar coordinate system with origin at the center of the plate. Let the displacement in the radial direction be u_r, and the displacement in the tangential direction be u_θ. Obviously $u_\theta = 0$. We can obtain the radial strain, tangential strain and shear strain as follows [72].

$$\varepsilon_{rr} = \frac{\partial u_r}{\partial r} \tag{C.1}$$

$$\varepsilon_{\theta\theta} = \frac{u_r}{r} + \frac{1}{r}\frac{\partial u_\theta}{\partial \theta} = \frac{u_r}{r} \tag{C.2}$$

$$\gamma_{r\theta} = \frac{\partial u_\theta}{\partial r} + \frac{1}{r}\frac{\partial u_r}{\partial \theta} - \frac{u_\theta}{r} = 0 \tag{C.3}$$

Let $u_r(r) = f(r)$. Then

$$\sigma_{rr}(r) = \frac{E}{1-\nu^2}(\varepsilon_{rr}+\nu\varepsilon_{\theta\theta}) = \frac{E}{1-\nu^2}\left(f'(r)+\frac{\nu f(r)}{r}\right) \tag{C.4}$$

$$\sigma_{\theta\theta}(r) = \frac{E}{1-\nu^2}(\varepsilon_{\theta\theta}+\nu\varepsilon_{rr}) = \frac{E}{1-\nu^2}\left(\frac{f(r)}{r}+\nu f'(r)\right) \tag{C.5}$$

$$\sigma_{r\theta}(r) = G\gamma_{r\theta} = 0 \tag{C.6}$$

For a section of the circular plate of radius x with an infinite small angle $d\theta$, we have equilibrium equation along its symmetric axis

$$\sigma_{rr}(x)hxd\theta = \int_0^x 2\sigma_{\theta\theta}(r)\sin\frac{d\theta}{2}hdr \tag{C.6}$$

Then we have

$$x\sigma_{rr}(x) = \int_0^x \sigma_{\theta\theta}(r)dr \tag{C.7}$$

So

$$\sigma_{rr}(x) + x\sigma'_{rr}(x) = \sigma_{\theta\theta}(x) \tag{C.7}$$

Then

$$f'(x)+\frac{\nu f(x)}{x}+xf''(x)+\nu\frac{xf'(x)-f(x)}{x}=\frac{f(x)}{x}+\nu f'(x) \tag{C.8}$$

We can get

$$x^2f''(x)+xf'(x)-f(x)=0 \tag{C.8}$$

It is an Euler differential equation. Its solution is

$$f(x)=C_1x+\frac{C_2}{x} \quad (x>0,\ C_1,\ C_2 \text{ are contants}) \tag{C.8}$$

We know $f(0)=0$ and $f(x)$ should be continuous at $x=0$. So $C_2=0$. Thus

$$\varepsilon_{rr} = \frac{\partial u_r}{\partial r}=C_1 \tag{C.9}$$

$$\varepsilon_{\theta\theta} = \frac{u_r}{r}=C_1 \tag{C.10}$$

Let $\varepsilon_{rr}=\varepsilon$, then

$$\sigma_{rr}=\frac{E}{1-\nu^2}(\varepsilon_{rr}+\nu\varepsilon_{\theta\theta})=\frac{E}{1-\nu}\varepsilon \tag{C.10}$$

The we can obtain the strain energy of a plate with a radius of a as follows.

$$E_p^s(\varepsilon)=\frac{E}{1-v}\varepsilon^2\cdot\pi a^2h=\frac{\pi Eha^2\varepsilon^2}{1-\nu} \tag{C.10}$$

APPENDIX D

Boundary Effect of the 2D Rectangle Meshed MSD Model

In this appendix, we will analyze the boundary effect of the 2D rectangle meshed MSD model.

D.1 Boundary effect of the 2D rectangle meshed MSD model

Refer to Fig. 5.3, for the nodes on the line MN, denote them by V_k, where $k = -1, 0, \cdots$, starting from boundary nodes. Let the contraction of the structural spring between adjacent nodes V_{k-1} and V_k be $s_k\,(k = 0, 1, \cdots)$. Assume MN to be far from the boundary in the direction of the x'-axis and the contraction of the structural springs connected to MN in the direction of the x'-axis is negligible.

Consider the equilibrium condition of the node V_{-1}, we have

$$P_1 - k_1 s_0 + P_2 - k_2(s_0 + s_1) + \sqrt{2}P_3 - k_3 s_0 = 0 \tag{D.0}$$

At node V_0, we have

$$P_1 - k_1 s_0 + \sqrt{2}P_3 - k_3 s_0 = P_1 - k_1 s_1 + P_2 - k_2(s_1 + s_2) + \sqrt{2}P_3 - k_3 s_1 \tag{D.1}$$

At node $V_k\,(k \geq 1)$, we have

$$P_1 - k_1 s_k + P_2 - k_2(s_{k-1} + s_k) + \sqrt{2}P_3 - k_3 s_k = P_1 \tag{D.2}$$

$$-k_1 s_{k+1} + P_2 - k_2(s_{k+1} + s_{k+2}) + \sqrt{2}P_3 - k_3 s_{k+1} \tag{D.3}$$

According to (5.52), (D.1), (D.1) and (D.3), we have

$$k_1 s_0 + k_2(s_0 + s_1) + k_3 s_0 + P_2 = 0 \tag{D.4}$$

$$k_1 s_1 + k_3 s_1 + k_2(s_1 + s_2) - k_1 s_0 - k_3 s_0 - P_2 = 0 \tag{D.5}$$

$$k_1 s_{k+1} + k_2(s_{k+1} + s_{k+2}) + k_3 s_{k+1} - k_1 s_k - k_2(s_{k-1} + s_k) - k_3 s_k = 0 \quad (k \geq 1) \tag{D.6}$$

We want to restrict the contraction to the area close to the boundary. First we try to limit the contraction within one structural springs around the boundary, i.e.

$$s_k = 0 \quad (k \geq 1) \tag{D.7}$$

From (D.4), (D.5) and (D.7), we have

$$k_1 s_0 + k_2 s_0 + k_3 s_0 + P_2 = 0 \tag{D.8}$$

$$k_1 s_0 + k_3 s_0 + P_2 = 0 \tag{D.9}$$

Then

$$k_2 = 0 \tag{D.10}$$

And in this situation, (D.4), (D.5), (D.6) and (D.7) are compatible. So we can restrict the boundary effect to only the boundary springs. Note that the derivation above is only valid for those nodes far from the corner of the MSD system. Due to the influence of the corner nodes, we can not completely limit the boundary effect to the boundary springs. But under (D.10), the boundary effect is very small for the non-boundary springs.

APPENDIX E

Coefficients of the Fourier Series

E.1 Coefficients of the Fourier Series

The coefficients of the Fourier series of $\cos 2\phi_{mi}$ and $\cos 4\phi_{mi}$ mentioned in section 7.2.1 are listed below.

$$a_{0,0} = \frac{\cos 2\alpha_{mi} - 1}{4} \tag{E.1}$$

$$a_{0,2} = \frac{\cos 2\beta_{mi}}{4} - \frac{\cos 2\alpha_{mi} \cos 2\beta_{mi}}{4} \tag{E.2}$$

$$a_{2,0} = \frac{1 + 3\cos 2\alpha_{mi}}{4} \tag{E.3}$$

$$a_{2,1} = -\frac{\sin 2\alpha_{mi} \sin \beta_{mi}}{2} \tag{E.4}$$

$$a_{2,-1} = -a_{2,1} \tag{E.5}$$

$$a_{2,2} = \frac{\cos 2\alpha_{mi} \cos 2\beta_{mi}}{8} - \frac{\cos 2\beta_{mi}}{8} \tag{E.6}$$

$$a_{2,-2} = a_{2,2} \tag{E.7}$$

$$b_{0,2} = \frac{\sin 2\beta_{mi}}{4} - \frac{\cos 2\alpha_{mi} \sin 2\beta_{mi}}{4} \tag{E.8}$$

$$b_{2,1} = \frac{\sin 2\alpha_{mi} \cos \beta_{mi}}{2} \tag{E.9}$$

$$b_{2,-1} = b_{2,1} \tag{E.10}$$

$$b_{2,2} = \frac{\cos 2\alpha_{mi} \sin 2\beta_{mi}}{8} - \frac{\sin 2\beta_{mi}}{8} \tag{E.11}$$

$$b_{2,-2} = -b_{2,2} \tag{E.12}$$

$$c_{0,0} = \frac{9\cos 4\alpha_{mi} - 4\cos 2\alpha_{mi} - 5}{64} \tag{E.13}$$

$$c_{0,2} = \frac{\cos 2\alpha_{mi} \cos 2\beta_{mi}}{4} - \frac{\cos 2\beta_{mi}}{16} - \frac{3\cos 4\alpha_{mi} \cos 2\beta_{mi}}{16} \tag{E.14}$$

$$c_{0,4} = -\frac{3\cos 2\alpha_{mi} \cos 4\beta_{mi}}{16} + \frac{9\cos 4\beta_{mi}}{64} + \frac{3\cos 4\alpha_{mi} \cos 4\beta_{mi}}{64} \tag{E.15}$$

$$c_{2,0} = \frac{5\cos 4\alpha_{mi} - 4\cos 2\alpha_{mi} - 1}{16} \tag{E.16}$$

$$c_{2,1} = \frac{\sin 2\alpha_{mi} \sin \beta_{mi}}{4} - \frac{\sin 4\alpha_{mi} \sin \beta_{mi}}{8} \tag{E.17}$$

$$c_{2,-1} = -c_{2,1} \tag{E.18}$$

$$c_{2,2} = \frac{\cos 2\beta_{mi}}{8} - \frac{\cos 4\alpha_{mi} \cos 2\beta_{mi}}{8} \tag{E.19}$$

$$c_{2,-2} = c_{2,2} \tag{E.20}$$

$$c_{2,3} = -\frac{\sin 2\alpha_{mi} \sin 3\beta_{mi}}{4} + \frac{\sin 4\alpha_{mi} \sin 3\beta_{mi}}{8} \tag{E.21}$$

$$c_{2,-3} = -c_{2,3} \tag{E.22}$$

$$c_{2,4} = -\frac{3}{2} c_{0,4} \tag{E.23}$$

$$c_{2,-4} = c_{2,4} \tag{E.24}$$

$$c_{4,0} = \frac{35 \cos 4\alpha_{mi} + 20 \cos 2\alpha_{mi} + 9}{64} \tag{E.25}$$

$$c_{4,1} = -\frac{\sin 2\alpha_{mi} \sin \beta_{mi}}{8} - \frac{7 \sin 4\alpha_{mi} \sin \beta_{mi}}{16} \tag{E.26}$$

$$c_{4,-1} = -c_{4,1} \tag{E.27}$$

$$c_{4,2} = -\frac{\cos 2\alpha_{mi} \cos 2\beta_{mi}}{8} - \frac{3 \cos 2\beta_{mi}}{32} + \frac{7 \cos 4\alpha_{mi} \cos 2\beta_{mi}}{32} \tag{E.28}$$

$$c_{4,-2} = c_{4,2} \tag{E.29}$$

$$c_{4,3} = -\frac{1}{2} c_{2,3} \tag{E.30}$$

$$c_{4,-3} = -c_{4,3} \tag{E.31}$$

$$c_{4,4} = \frac{3}{8} c_{0,4} \tag{E.32}$$

$$c_{4,-4} = c_{4,4} \tag{E.33}$$

$$d_{0,2} = \frac{\cos 2\alpha_{mi} \sin 2\beta_{mi}}{4} - \frac{\sin 2\beta_{mi}}{16} - \frac{3 \cos 4\alpha_{mi} \sin 2\beta_{mi}}{16} \tag{E.34}$$

$$d_{0,4} = -\frac{3 \cos 2\alpha_{mi} \sin 4\beta_{mi}}{16} + \frac{9 \sin 4\beta_{mi}}{64} + \frac{3 \cos 4\alpha_{mi} \sin 4\beta_{mi}}{64} \tag{E.35}$$

$$d_{2,1} = -\frac{\sin 2\alpha_{mi} \cos \beta_{mi}}{4} + \frac{\sin 4\alpha_{mi} \cos \beta_{mi}}{8} \tag{E.36}$$

$$d_{2,-1} = d_{2,1} \tag{E.37}$$

$$d_{2,2} = \frac{\sin 2\beta_{mi}}{8} - \frac{\cos 4\alpha_{mi} \sin 2\beta_{mi}}{8} \tag{E.38}$$

$$d_{2,-2} = -d_{2,2} \tag{E.39}$$

$$d_{2,3} = \frac{\sin 2\alpha_{mi} \cos 3\beta_{mi}}{4} - \frac{\sin 4\alpha_{mi} \cos 3\beta_{mi}}{8} \tag{E.40}$$

$$d_{2,-3} = d_{2,3} \tag{E.41}$$

$$d_{2,4} = -\frac{3}{2} d_{0,4} \tag{E.42}$$

$$d_{2,-4} = -d_{2,4} \tag{E.43}$$

$$d_{4,1} = \frac{\sin 2\alpha_{mi} \cos \beta_{mi}}{8} + \frac{7 \sin 4\alpha_{mi} \cos \beta_{mi}}{16} \tag{E.44}$$

$$d_{4,-1} = d_{4,1} \tag{E.45}$$

$$d_{4,2} = -\frac{\cos 2\alpha_{mi} \sin 2\beta_{mi}}{8} - \frac{3 \sin 2\beta_{mi}}{32} + \frac{7 \cos 4\alpha_{mi} \sin 2\beta_{mi}}{32} \tag{E.46}$$

$$d_{4,-2} = -d_{4,2} \tag{E.47}$$

$$d_{4,3} = -\frac{1}{2} d_{2,3} \tag{E.48}$$

$$d_{4,-3} = d_{4,3} \tag{E.49}$$

$$d_{4,4} = \frac{3}{8} d_{0,4} \tag{E.50}$$

$$d_{4,-4} = -d_{4,4} \tag{E.51}$$

REFERENCES

[1] C. Kuhn, "The karlsruhe endoscopic surgery trainer," Forschungszentrum Karlsruhe, January 1997. [Online]. Available: http://iregt1.iai.fzk.de/TRAINER/

[2] B. Mirtich and S. F. F. Gibson, "A survey of deformable modeling in computer graphics," MERL, Tech. Rep., Feb. 13 1998. [Online]. Available: http://citeseer.ist.psu.edu/435596.html; http://www.merl.com/reports/TR97-19/TR97-19.ps.gz

[3] H. Delingette, S. Cotin, and N. Ayache, "A hybrid elastic model allowing real-time cutting, deformations and force-feedback for surgery training and simulation," in *CA '99: Proceedings of the Computer Animation*. IEEE Computer Society, 1999, pp. 70–81.

[4] National Library of Medicine, "MEDLINEplus." [Online]. Available: http://www.nlm.nih.gov/medlineplus/tutorials/inguinalhernia/

[5] S. Sugavanam, "Simulation of preperitoneal mesh in larparoscopic hernia surgery," Master's thesis, University of Texas at Arlington, Arlington Texas, August 2002.

[6] G. Gopalakrishnan, "Stapsim: Virtual reality based stapling simulation for laparoscopic herniorrhaphy," Master's thesis, University of Texas at Arlington, May 2003.

[7] P. J. Quilici, "Laparoscopic repair of inguinal & femoral hernias." [Online]. Available: http://www.laparoscopy.net/inguinal/ingher1.htm

[8] J. Benshetler, "Blunt dissection in surgical simulation," Master's thesis, University of Texas at Arlington, December 2003.

[9] National Library of Medicine, "The visible human project." [Online]. Available: http://www.nlm.nih.gov/research/visible/

[10] W. Wayand, "The history of minimally invasive surgery," in *Global Surgery 2004*, pp. 37–38. [Online]. Available: http://www.bbriefings.com/download.cfm?fileID=3978

[11] D. B. Jones, J. S. Wu, and N. J. Soper, *Laparoscopic Surgery Principles and Procedures.* Quality Medical Publishing, Inc., 1997.

[12] The MRC Laparoscopic Groin Hernia Trial Group, "Laparoscopic versus open repair of groin hernia: a randomised comparison," *The Lancet*, vol. 354, pp. 185–190, 1999.

[13] L. Raghupathi, V. Devarajan, R. Eberhart, and D. B. Jones, "Simulation of bleeding during laparoscopic herniorrhaphy," in *Proc. Medicine Meets Virtual Reality*, 2002, pp. 382–387.

[14] T. W. Sederberg and S. R. Parry, "Free-form deformation of solid geometric models," in *SIGGRAPH '86: Proceedings of the 13th annual conference on Computer graphics and interactive techniques.* New York, NY, USA: ACM Press, 1986, pp. 151–160.

[15] P. Faloutsos, M. van de Panne, and D. Terzopoulos, "Dynamic free-form deformations for animation synthesis," *IEEE Transactions on Visualization and Computer Graphics*, vol. 3, no. 3, pp. 201–214, 1997.

[16] H. Z. Tan, M. A. Srinivasan, B. Eberman, and B. Cheng, "Human factors for the design of force-reflecting haptic interface," in *Proc. Winter Annual Meeting of the American Society of Mechanical Engineers: Dynamic Systems and Control*, vol. 55-1, 1994, pp. 353–359.

[17] A. Gande, "Instructor station for virtual laparoscopic surgery," Master's thesis, University of Texas at Arlington, August 2003.

[18] A. Yoganathan and F. Sotiropoulos, "Using computational fluid dynamics to examine the haemodynamics of artificial heart valves," in *Business Briefing: US Cardiology 2004*, 2004, pp. 1–5. [Online]. Available: http://www.touchbriefings.com/pdf/1102/yoganathan.pdf

[19] J. Thilmany, "Surgical analysis," *Mechanical Engineering Magazine Online*, August 2004. [Online]. Available: http://www.memagazine.org/backissues/aug04/features/surgany/surgany.html

[20] B. A. Szabo, *Finite Element Analysis*. New York : Wiley, 1991.

[21] M. Bro-Nielsen, "Surgery simulation using fast finite elements," in *VBC '96: Proceedings of the 4th International Conference on Visualization in Biomedical Computing*. London, UK: Springer-Verlag, 1996, pp. 529–534.

[22] D. Terzopoulos, J. Platt, A. Barr, and K. Fleischer, "Elastically deformable models," *SIGGRAPH Comput. Graph.*, vol. 21, no. 4, pp. 205–214, 1987.

[23] S. M. Platt and N. I. Badler, "Animating facial expressions," in *Proc. SIGGRAPH'81*. ACM Press, 1981, pp. 245–252.

[24] K. Waters, "A muscle model for animating three-dimensional facial expression," *ACM Computer Graphics*, vol. 21, no. 4, pp. 17–24, July 1987.

[25] D. Terzopoulos and K. Waters, "Physically-based facial modeling, analysis and animation," *J. of Visual. and Comput. Animation*, no. 1, pp. 73–80, 1990.

[26] D. Baraff and A. Witkin, "Dynamic simulation of non-penetrating flexible bodies," in *Proc. SIGGRAPH'92*, 1992, pp. 303–308.

[27] M. Desbrun, P. Schröder, and A. Barr, "Interactive animation of structured deformable objects," in *Graphics Interface*, June 1999, pp. 1–8. [Online]. Available: http://www.graphicsinterface.org/proceedings/1999/141

[28] D. Baraff and A. Witkin, "Large steps in cloth simulation," in *Proc. SIGGRAPH'98*, 1998, pp. 43–54.

[29] J. Brown, K. Montgomery, J.-C. Latombe, and M. Stephanides, "A microsurgery simulation system," in *Medical Image Computing and Computer-Assisted Interventions*, 2001, pp. 137–144.

[30] J. Zhang, S. Payandeh, and J. Dill, "Haptic subdivision: an approach to defining level-of-detail in haptic rendering," in *Proc. 10th Symposium on Haptic Interfaces for Virtual Environment and Teleoperator Systems*, 2002, pp. 201–208.

[31] M. Bro-Nielson, "Fast finite elements for surgery simulation," in *Proc. 5th Medicine Meets Virtual Reality*, 1997.

[32] S. P. DiMaio and S. E. Salcudean, "Simulated interactive needle insertion," in *Proc. 10th Symposium on Haptic Interfaces for Virtual Environment and Teleoperator Systems*, 2002, pp. 344–351.

[33] S. De and K. J. Bathe, "The method of finite spheres," *Computational Mechanics*, vol. 25, pp. 329–345, 2000.

[34] ——, "The method of finite spheres: a summary of recent developments," in *Proc. 1st MIT Conference on Computational Fluid and Solid Mechanics*, 2001, pp. 1546–1549.

[35] J. Kim, S. De, and M. A. Srinivasan, "Computationally efficient techniques for real time surgical simulation with force feedback," in *Proc. IEEE Virtual Reality Conference*, 2002.

[36] Y. C. Fung, *A first Course in Continuum mechanics.* Prentice-Hall, 1969.

[37] G. Debunne, A. H. Barr, and M.-P. Cani, "Interactive multi-resolution animation of deformable models," in *Proceedings of Eurographics Workshop on Computer Animation and Simulation*, 1999.

[38] D.-C. Tseng and J.-Y. Lin, "A hybrid physical deformation modeling for laparoscopic surgery simulation," in *Proc. 2000 World Congress on Medical Physics and Biomedical Engineering*, 2000.

[39] R. Balaniuk and K. Salisbury, "Dynamic simulation of deformable objects using the long element method," in *Proc. 10th international symposium on Haptic Interfaces for Virtual Environment and Teleoperator systems*, 2002, pp. 58–65.

[40] W. T. Reeves, "Particle systems—a technique for modeling a class of fuzzy objects," *ACM Trans. Graph.*, vol. 2, no. 2, pp. 91–108, 1983.

[41] G. S. P. Miller, "The motion dynamics of snakes and worms," in *Proc. SIGGRAPH'88*. ACM Press, 1988, pp. 169–173.

[42] X. Tu and D. Terzopoulos, "Artificial fishes: Physics, locomotion, perception, behavior," in *Proc. SIGGRAPH'94*. ACM Press, 1994, pp. 43–50.

[43] D. E. Breen, D. H. House, and M. J. Wozny, "Predicting the drape of woven cloth using interacting particles," in *Proc. SIGGRAPH'94*. ACM Press, 1994, pp. 365–372.

[44] B. Eberhardt, A. Weber, and W. Strasser, "A fast, flexible, particle-system model for cloth draping," *IEEE Comput. Graph. Appl.*, vol. 16, no. 5, pp. 52–59, 1996.

[45] M. Carignan, Y. Yang, N. M. Thalmann, and D. Thalmann, "Dressing animated synthetic actors with complex deformable clothes," *SIGGRAPH Comput. Graph.*, vol. 26, no. 2, pp. 99–104, 1992.

[46] P. Volino, M. Courchesne, and N. M. Thalmann, "Versatile and efficient techniques for simulating cloth and other deformable objects," in *Proc. SIGGRAPH'95*. ACM Press, 1995, pp. 137–144.

[47] D. H. House and D. E. Breen, *Cloth Modeling and Animation*. A. K. Peters, Ltd., 2000.

[48] T. Vassilev, B. Spanlang, and Y. Chrysanthou, "Fast cloth animation on walking avatars," *Comput. Graph. Forum*, vol. 20, no. 3, pp. 260–267, 2001, ISSN 1067-7055.

[49] K.-J. Choi and H.-S. Ko, "Stable but responsive cloth," in *Proc. SIGGRAPH'02*. ACM Press, 2002, pp. 604–611.

[50] Y. Shen, V. Devarajan, and R. Eberhart, "Haptic herniorrhaphy simulation with robust and fast collision detection algorithm," in *Proc. of Medicine Meets Virtual Reality*, 2004.

[51] D. Hutchinson, M. Preston, and T. Hewitt, "Adaptive refinement for mass/spring simulations," in *Proceedings of the Eurographics workshop on Computer animation and simulation '96*. Springer-Verlag New York, Inc., 1996, pp. 31–45.

[52] D. Bourguignon and M.-P. Cani, "Controlling anisotropy in mass-spring systems," in *Proc. 11th Eurographics Workshop on Animation and Simulation*, 2000, pp. 113–123.

[53] M. Desbrun, P. Schröder, and A. Barr, "Interactive animation of structured deformable objects," in *Proceedings of the 1999 conference on Graphics interface '99*. San Francisco, CA, USA: Morgan Kaufmann Publishers Inc., 1999, pp. 1–8.

[54] M. Hauth, O. Etzmuss, and W. Strasser, "Analysis of numerical methods for the simulation of deformable models," *The Visual Computer*, vol. 19, no. 7–8, pp. 581–600, 2003.

[55] X. Provot, "Deformation constraints in a mass-spring model to describe rigid cloth behavior," in *Proc. Graph. Interface*, 1995, pp. 147–154.

[56] E. Boxerman and U. Ascher, "Decomposing cloth," in *SCA '04: Proceedings of the 2004 ACM SIGGRAPH/Eurographics symposium on Computer animation*. New York, NY, USA: ACM Press, 2004, pp. 153–161.

[57] J. Brown, "Real time soft tissue and suture simulation," Ph.D. dissertation, Stanford University, 2003.

[58] S. P. DiMaio, "Modelling, simulation and planning of needle motion in soft tissues," Ph.D. dissertation, The University of British Columbia, 2003.

[59] I. Beju, *Euclidean Tensor Calculus with Applications*. Bucures,ti, Romania : Editura Tehnica; Tunbridge Wells, Kent : Abacus Press, 1983.

[60] G. Debunne, M. Desbrun, M.-P. Cani, and A. H. Barr, "Dynamic real-time deformations using space & time adaptive sampling," in *SIGGRAPH '01: Proceedings of*

the 28th annual conference on Computer graphics and interactive techniques. ACM Press, 2001, pp. 31–36.

[61] S. Cotin, H. Delingette, and N. Ayache, "Real-time elastic deformations of soft tissues for surgery simulation stéphane cotin, hervé delingette, and nicholas ayache," in *IEEE Transactions on Visualization and Computer Graphics*, H. Hagen, Ed. IEEE Computer Society, 1999, vol. 5 (1), pp. 62–73. [Online]. Available: http://visinfo.zib.de/EVlib/Show?EVL-1999-389

[62] H. Delingette, "Towards realistic soft tissue modeling in medical simulation," Inria, Institut National de Recherche en Informatique et en Automatique, Technical Report RR-3506, 1998.

[63] X. Wang and V. Devarajan, "A honeycomb model for soft tissue deformation," in *Proc. ACM SIGGRAPH international conference on Virtual-Reality Continuum and its applications in Industry*, 2004, pp. 257–260.

[64] N. Jojic and T. S. Huang, "Estimating cloth draping parameters from range data," in *Proc. International Workshop on Synthetic-Natural Hybrid Coding and Three Dimensional Imaging*, 1997, pp. 73–76.

[65] A. V. Gelder, "Approximate simulation of elastic membranes by triangulated spring meshes," *J. Graph. Tools*, vol. 3, no. 2, pp. 21–42, 1998.

[66] K. S. Bhat, C. D. Twigg, J. K. Hodgins, P. K. Khosla, Z. Popovic, and S. M. Seitz, "Estimating cloth simulation parameters from video," in *Proc. ACM SIGGRAPH/Eurographics Symposium on Computer Animation*, D. Breen and M. C. Lin, Eds., 2003, pp. 37–51.

[67] A. Maciel, R. Boulic, and D. Thalmann, "Deformable tissue parameterized by properties of real biological tissue," in *Proc. International Symposium on Surgery Simulation and Soft Tissue Modeling*, 2003, pp. 74–87.

[68] R. Bridson, S. Marino, and R. Fedkiw, "Simulation of clothing with folds and wrinkles," in *Proc. 2003 ACM SIGGRAPH/Eurographics Symposium on Computer animation*. Eurographics Association, 2003, pp. 28–36.

[69] E. Grinspun, A. N. Hirani, M. Desbrun, and P. Schröder, "Discrete shells," in *SCA '03: Proc. 2003 ACM SIGGRAPH/Eurographics Symposium on Computer animation*. Eurographics Association, 2003, pp. 62–67.

[70] X. Wang and V. Devarajan, "2D structured mass-spring system parameter optimization based on axisymmetric bending for rigid cloth simulation," in *Proc. ACM SIGGRAPH international conference on Virtual-Reality Continuum and its applications in Industry*, 2004, pp. 317–324.

[71] V. Panc, *Theory of Elastic Plates*. Noordhoff International Publishing Leyden, 1975.

[72] R. Solecki and R. J. Conant, *Advanced Mechanics of Materials*. Oxford University Press, 2003.

[73] J. N. Reddy, *Theory and Analysis of Elastic Plates*. Philadelphia, PA : Taylor & Francis, 1998.

[74] J. Lander, "1999 game developer magazine article companion," 1999. [Online]. Available: http://www.darwin3d.com/gdm1999.htm

[75] X. Wang and V. Devarajan, "1D and 2D structured mass-spring model with preload," *The Visual Computer*, vol. 21, no. 7, 429–448.

[76] R. T. Fenner, *Mechanics of Solids*. CRC Press, 1993.

[77] E. W. Weisstein, "Circle lattice points," From MathWorld. [Online]. Available: http://mathworld.wolfram.com/CircleLatticePoints.html

[78] X. Wang and V. Devarajan, "Physically improved 2D mass-spring-damper model using unstructured triangular meshes," *MIT Presence: Teleoperators and Virtual Environments*, submitted for publication.

[79] C. Geuzaine and J.-F. Remacle, *Gmsh Reference Manual*, 2004.

[80] X. Wang and V. Devarajan, "Parameter optimization for 3D haptic mass-spring-damper models," *IEEE Transactions on Visualization and Computer Graphics*, submitted for publication.

[81] D. Terzopoulos, J. Platt, and K. Fleischer, "Heating and melting deformable models (from goop to glop)," in *Proc. Graph. Interface*, 1989, pp. 219–226.

[82] M. Kass, "An introduction to physically based modeling, chapter:introduction to continuum dynamics for computer graphics," 1995. [Online]. Available: http://www-2.cs.cmu.edu/afs/cs/user/baraff/www/pbm/continuators.pdf

[83] O. Etzmuss, J. Gross, and W. Strasser, "Deriving a particle system from continuum mechanics for the animation of deformable objects," *IEEE Trans. Visual. Comput. Graphics*, vol. 9, no. 4, pp. 538–550, 2003.

[84] The British Hernia Center, "Hernia infomation home page." [Online]. Available: http://www.hernia.org/

[85] J. Hureau, P. Vayre, V. Chapuis, M. A. Germain, J. L. Jost, J. Murat, and G. Spay, "Risk of laparoscopic surgery. 100 records of complications. a qualitative study," *Chirurgie*, vol. 121, no. 1, pp. 1–8, 1996.

[86] R. Agarwal, Y. Bhasin, L. Raghupathi, and V. Devarajan, "Special visual effects for surgical simulation: Cauterization, irrigation and suction," in *Proc. Medicine Meets Virtual Reality*, 2003, pp. 1–3.

[87] S. Sugavanam and V. Devarajan, "Special visual effects for surgical simulation: Cauterization, irrigation and suction," in *Proc. Medicine Meets Virtual Reality*, 2003, pp. 1–3.

[88] A. Gande and V. Devarajan, "Instructor station for virtual laparoscopic surgery: Requirements and design," in *Proc. Computer Graphics and Imaging Conference*, 2003, pp. 1–7.

[89] V. Gupta and V. Devarajan, "Extraction of realistic anatomical texture from visible human data for laparoscopic surgery simulation," in *Proc. Medicine Meets Virtual Reality*, 2004.

[90] G. Gopalakrishnan and V. Devarajan, "Stapsim: A virtual reality-based stapling simulator for laparoscopic herniorrhaphy," in *Proc. Medicine Meets Virtual Reality*, 2004, pp. 111–113.

[91] S. Kapdoskar and V. Devarajan, "Use of the visible human dataset and 3d studio max to model laparoscopic inguinal herniorrhaphy," in *Proc. Medicine Meets Virtual Reality*, 2004.

[92] S. Gottschalk, M. Lin, and D. Manocha, "OBBTree: A hierarchical structure for rapid interference detection," in *Proceedings of the ACM Conference on Computer Graphics*. New York: ACM, Aug. 4–9 1996, pp. 171–180.

[93] L. Raghupathi, V. Devarajan, R. C. Eberhart, and D. B. Jones, "Simulation of bleeding during laparoscopic herniorrhaphy," in *Proc. Medicine Meets Virtual Reality*. IO Press, 2002.

[94] R. Agarwal, "Simulation of irrigation and suction for a virtual reality based laparascopic surgery simulator," Master's thesis, University of Texas at Arlington, May 2003.

[95] Y. Zhuang and J. Canny, "Real-time global deformations," in *Workshop on Algorithmic Foundations of Robotics*, 2000, pp. 97–107.

BIOGRAPHICAL STATEMENT

Xiuzhong Wang was born in Anhui Province, P. R. China. He received his B.E. degree from Northwestern Polytechnical University at Xi'an, China in 1994. After working in industry for three years, he continued to study. He obtained his M.E. degree in control theory and applications from The Institute of Automation, Chinese Academy of Sciences in 2000, and his Ph.D. degree in electrical engineering from The University of Texas at Arlington in 2005.